THE RUNUP AND REFLECTION OF SOLITARY WAVES ON STEEP SLOPES

by

S. Grilli and I. A. Svendsen

RESEARCH REPORT NO. CACR-91-04
April 1991

CENTER FOR APPLIED COASTAL RESEARCH
University of Delaware
Department of Civil Engineering
Newark, DE 19716

The Runup and Reflection of Solitary Waves on Steep Slopes

S. Grilli and I. A. Svendsen

Abstract

The runup and reflection of a solitary wave are examined using a higher order Boundary Element Method for the velocity potential, using the full nonlinear free surface boundary conditions. The time integration is explicit and of second order in Δt. The solitary waves are either numerically *exact* solutions of the nonlinear potential problem, directly introduced in the model, or approximate *first-order* waves generated by a numerical piston wavemaker like in laboratory experiments. The transformation of the approximate waves are studied as they propagate down a numerical wave tank. Reflection on a vertical wall of the waves generated both ways is studied and differences in runup and pressure force analyzed. Values of runup, rundown, reflected wave, celerity, phase shift, energy partition and pressure force of the *exact* solitary waves are compared with other numerical or analytical solutions. Results show, effects of order higher than 3rd in wave height are becoming important for the highest waves. Comparisons are made for runup and reflection from steep slopes (45°, 70°) with detailed measurements of solitary waves generated by a piston wavemaker. Free surface elevations are found to agree quite well with the measurements and even small scale disturbances in the experiments from the nonlinear processes are reproduced surprisingly accurately. Finally, a detailed analysis is given of the velocity and pressure variation during the runup and reflection process on a 45° slope, and the applicability of the nonlinear shallow water equations is discussed on the basis of the computational results.

1 Introduction

Over the last decade numerical solution of the exact nonlinear equations for the inviscid water waves using a Boundary Integral Equation (BIE) description has become an extremely successful method for analyzing free surface motion and, in particular, the overturning of breaking waves. Practically all previous contributions, however, utilize space periodicity of the waves and most of them also are based on a conformal mapping of physical space onto

a plane in which the equivalent of the free surface is the only part left of the boundary. The Boundary Integral Equation is then solved in the transformed plane. A few contributions use other complex variable-dependent techniques.

There are many advantages of this method which has been explored extensively by many authors. Particularly noteworthy for significant steps to the development are contributions by Longuet-Higgins & Cokelet (1976), Vinje & Brevig (1981) and Dold & Peregrine (1986). The procedure, however, also has some important limitations which are associated with the use of complex variables and with the assumption of waves that are periodic in space. A more complete review of the literature on the subject can be found in Grilli, *et al.* (1989).

In the present paper, we develop an equally efficient and accurate method without those two limiting assumptions and we apply it to a problem for which the above-mentioned version is not well suited, namely the generation of a solitary wave, its subsequent propagation and development as it runs up and is reflected from a vertical wall or from a steep smooth slope. Hence, we consider the wave motion in the physical space and computations are made for the velocity potential, using the fully nonlinear free surface boundary conditions. An important difference from the existing space periodic solutions lies in specifying the boundary conditions in the physical space where there is a moving surface piercing boundary. For completeness, other contributions to the development of various forms of such computations in physical space have been given by Isaacson (1982), Kim, Liu & Liggett (1983), Nakayama (1983), Greenhow & Lin (1985), Dommermuth & Yue (1987), Sugimoto, *et al.* (1987) and Romate (1989).

The motion is described using a Green's function, to transform the Laplace equation into an integral equation (BIE) that involves only values of the velocity potential and its normal derivative along the physical boundary. The numerical procedure used for solving the BIE is a higher-order Boundary Element Method (BEM). The time integration corresponds to the explicit scheme developed by Dold & Peregrine (1986). Grilli, *et al.* (1988) modified this method to using the shape functions of the BEM and applied it to the physical space. A version correct to second order in Δt has been developed for the computations presented here.

Since the computations are made in physical space, but only covering a limited region of a long wave tank, the waves to be studied have to be generated at one end of or inside the fluid domain. Solitary waves will differ, depending on the way they are generated in the numerical model. Numerically exact solitary wave solutions of the fully nonlinear potential flow equations will be generated by Tanaka's (1986) method and introduced in the model directly on the free surface; in the following, these waves will be termed, for short : *exact* solitary waves. Waves will

also be generated as in laboratory experiments, by numerically simulating a piston wavemaker, moving according to Goring's (1978) first-order solution; in the following, these waves will be termed, for short : *first-order* solitary waves.

Runup and reflection from slopes of non-breaking solitary waves have been studied quite extensively in the literature. This was the topic of the boundary integral computations by Kim, *et al.* (1983) who, however, only used a few computation points and gave very few details about the results. In fact, the solitary wave runup problem using Euler equations was studied numerically already by Camfield & Street (1969) by means of a marker and cell method.

More commonly, however, the runup of solitary waves has been analyzed using long wave or Boussinesq theory. The special case of reflection from a vertical wall is equivalent to the problem of collision between two opposing solitary waves of the same height and several studies have been published utilizing that analogy. A first-order solution can be obtained by the Inverse Scattering Technique developed by Gardner, *et al.* (1967), a 3rd-order analysis was developed by Su & Gardner (1969) and Su & Mirie (1980) and solved numerically by Mirie & Su (1982), and a 5th-order analysis was developed by Byatt-Smith (1988). Fenton & Rienecker (1982) used a Fourier Method to obtain very high order results for the same problem (somewhat limited, however, in the representation of high frequency oscillations by the periodicity condition they had to impose in their method).

The runup on a slope was analyzed numerically on the basis of the Boussinesq equations by Pedersen & Gjevik (1983), and analytically by Synolakis (1987) who generalized the approach of Carrier (1966), based on the Nonlinear Shallow Water equation (NSW), to apply to the situation also considered in this paper with a constant depth region in front of the slope.

We will show that our method is quite capable of accurately describing fully nonlinear free surface flows in great detail and over periods of time at least long enough to allow us to study wave runup problems without having to introduce any smoothing or modification of the solution. The method will be used for analyzing the higher-order effects in terms of the ratio wave height over depth, which occur during reflection of high solitary waves from a vertical wall and from steep slopes. In particular, values of runup and rundown, reflected wave, celerity, phase shift, energy partition and pressure force on the slope will be compared with other numerical or analytical solutions (vertical wall), and with recent experimental results (steep slopes).

The theoretical background is briefly outlined in Section 2 and 3. The generation and horizontal propagation of both *exact* and *first-order* solitary waves is described in Section 4. Results obtained with both generation methods are compared in Section 5 with those of Su & Mirie (1980), Fenton & Rienecker (1982) and Byatt-Smith (1988), for the case of a vertical wall. Finally, the generation

by a piston wavemaker motion is used in Section 6, for making a comparison with the experimental results by Losada, *et al.* (1986) for the runup and reflection from steep slopes (Section 6.2). Computational results are also given for detailed evolution of the internal velocity field (Section 6.3) and for the pressure along the slope (Section 6.4). Both are shown to deviate substantially from the basic assumption underlying the NSW solution of, e.g., Synolakis (1987) (Section 6.5). Some of these results, using an earlier, less accurate version of the method, were reported by Grilli & Svendsen (1989) and Svendsen & Grilli (1990).

2 Mathematical formulation

2.1 *Governing equations and boundary conditions*

We consider an inviscid irrotational 2-D flow described by a velocity potential $\phi(\mathbf{x},t)$, and the velocity field is given by $\mathbf{u} = \nabla\phi = (u,w)$. Thus, the continuity equation in the fluid domain $\Omega(t)$ with the boundary $\Gamma(t)$ becomes a Laplace equation for ϕ (Figure 1),

$$\nabla^2\phi = 0 \qquad \text{in } \Omega(t) \tag{1}$$

Using the free space Green's function, $G(\mathbf{x},\mathbf{x}_l) = -\frac{1}{2\pi}\log|\,\mathbf{x}-\mathbf{x}_l\,|$, (1) becomes the boundary integral equation,

$$\alpha(\mathbf{x}_l)\phi(\mathbf{x}_l) = \int_\Gamma [\frac{\partial\phi}{\partial n}(\mathbf{x})G(\mathbf{x},\mathbf{x}_l) - \phi(\mathbf{x})\frac{\partial G(\mathbf{x},\mathbf{x}_l)}{\partial n}]\,d\Gamma \tag{2}$$

where $\mathbf{x} = (x,z)$ and $\mathbf{x}_l = (x_l,z_l)$ are position vectors for points on the boundary, and $\alpha(\mathbf{x}_l)$ is a geometric coefficient.

On the free surface $\Gamma_f(t)$, ϕ satisfies the kinematic boundary condition,

$$\frac{D\mathbf{r}}{Dt} = (\frac{\partial}{\partial t} + \mathbf{u}\cdot\nabla)\mathbf{r} = \mathbf{u} \qquad \text{on } \Gamma_f(t) \tag{3}$$

with $\mathbf{r}$, the position vector of a free surface fluid particle. Thus

$$\frac{D\mathbf{r}}{Dt} = \nabla\phi \qquad \text{on } \Gamma_f(t) \tag{4}$$

and the dynamic free surface boundary condition,

$$\frac{D\phi}{Dt} = -gz + \frac{1}{2}|\,\nabla\phi\,|^2 - \frac{p_a - p_o}{\rho} \qquad \text{on } \Gamma_f(t) \tag{5}$$

where g is the acceleration due to gravity, z is the vertical coordinate (positive upwards and $z = 0$ at the undisturbed free surface), p_a the pressure at the surface, p_o a reference pressure (e.g. at infinity) and ρ the fluid density.

The solitary waves are generated in two ways. In the first, the potential $\phi(x,t_o)$ and the elevation $\eta(x,t_o)$ of an *exact* solitary wave are prescribed on the free surface $\Gamma_f(t_o)$ at an initial time t_o. In this case, the normal velocity is zero over the leftward boundary Γ_{r1}, so that we have (see Figure 1),

$$\begin{aligned} &\phi = \phi(x,t_o)\ ,\ z = \eta(x,t_o) && \text{on } \Gamma_f(t_o) \\ &\nabla\phi\cdot\mathbf{n} \equiv \frac{\partial\phi}{\partial n} = 0 && \text{on } \Gamma_{r1} \end{aligned} \tag{6}$$

where $\mathbf{n}$ is the unit outward normal vector. In the second method, *first-order* solitary waves are generated by simulating a piston-type wavemaker motion on the boundary $\Gamma_{r1}(t)$. In this second case, the normal velocity is specified over the surface of the paddle by,

$$\nabla\phi\cdot\mathbf{n} \equiv \frac{\partial\phi}{\partial n} = u_p(x_p(t),t)\ n_x \qquad \text{on } \Gamma_{r1}(t) \tag{7}$$

where (x_p, u_p) are prescribed wavemaker position and velocity respectively.

Along the stationary bottom Γ_b and the slope Γ_{r2} we have in both cases,

$$\nabla\phi\cdot\mathbf{n} \equiv \frac{\partial\phi}{\partial n} = 0 \qquad \text{on } \Gamma_b \text{ and } \Gamma_{r2} \tag{8}$$

2.2 *The time stepping method*

The time stepping consists of integrating the two nonlinear free surface conditions (4) and (5) to establish the new position of the free surface and the relevant boundary conditions of Laplace's problem at the next time step. Following the approach used by Dold & Peregrine (1986), the updating of $\Gamma_f(t)$ is based on a truncated Taylor expansion in a Lagrangian formulation which corresponds to following a fluid particle,

$$\mathbf{r}(t+\Delta t) = \mathbf{r}(t) + \sum_{k=1}^{m} \frac{(\Delta t)^k}{k!}\frac{D^k\mathbf{r}(t)}{Dt^k} + O[(\Delta t)^{m+1}] \tag{9}$$

and the analogous for ϕ.

All the partial derivatives of ϕ with respect to time satisfy equation (1) so the coefficients of Δt in equation (9) can be found from a sequence $\{\phi,\ \frac{\partial\phi}{\partial t}\ ,\ \frac{\partial^2\phi}{\partial t^2}\ ,...\}$ of solutions of a succession of Laplace's equations. The expansion coefficients are then expressed as function of $\{\phi,\ \frac{\partial\phi}{\partial n}\ ,\ \frac{\partial\phi}{\partial t}\ ,\ \frac{\partial^2\phi}{\partial t\partial n}\ ,...\}$ and of their derivatives along the free surface (s-derivatives). The order of the latter derivatives increases as the order m of the Taylor series (9). Since the s-derivatives have to be computed by numerical differentiation – an operation which loses accuracy in the corners of a physical domain – we have so far limited the series and thus the s-derivatives to second order

($m = 2$). The procedure described can, however, in principle be extended to higher order and, in particular, for space periodic problems where the periodicity conditions can be used to avoid extrapolating the s-derivatives in the corners, higher order time series have been used by others (see Dold & Peregrine (1986) (m=3), Nam Seo (1988) (m=4)).

While the boundary conditions for all Laplace problems are readily obtained along the solid boundaries, the boundary values for $\frac{\partial \phi}{\partial t}$ at the free surface, are obtained from the Bernoulli equation. For $m > 2$, the $\{\frac{\partial^2 \phi}{\partial t^2}, ...\}$ would be obtained from the successive time derivatives of Bernoulli's equation.

In the computations, the terms in (9) are expressed in a local curvilinear coordinate system defined by (**s**,**n**), the tangential and normal unit vectors at a point of the free surface. For $m = 2$, the first two Lagrangian time derivatives are needed for evaluating the series. Defining,

$$\cos\beta = \frac{\partial x}{\partial s}\ ,\ \sin\beta = \frac{\partial z}{\partial s}\ ;\ \mathbf{s} = [\cos\beta\ ,\ \sin\beta]\ ,\ \mathbf{n} = [-\sin\beta\ ,\ \cos\beta]$$

we obtain by (4),

$$\frac{D\mathbf{r}}{Dt} = \frac{\partial \phi}{\partial s}\mathbf{s} + \frac{\partial \phi}{\partial n}\mathbf{n} \tag{10}$$

The continuity and irrotationality conditions yield,

$$\begin{aligned} \frac{\partial w}{\partial z} = -\frac{\partial u}{\partial x} \quad &\text{or} \quad \frac{\partial^2 \phi}{\partial n^2} = -\frac{\partial^2 \phi}{\partial s^2} + \frac{\partial \phi}{\partial n}\frac{\partial \beta}{\partial s} \\ \frac{\partial w}{\partial x} = \frac{\partial u}{\partial z} \quad &\text{or} \quad \frac{\partial^2 \phi}{\partial n \partial s} = \frac{\partial^2 \phi}{\partial s \partial n} \end{aligned} \tag{11}$$

where $\frac{\partial \beta}{\partial s}$ is the boundary curvature. After some calculations we get,

$$\begin{aligned} \frac{D^2\mathbf{r}}{Dt^2} = &(\frac{\partial^2 \phi}{\partial t \partial s} + \frac{\partial \phi}{\partial s}\frac{\partial^2 \phi}{\partial s^2} + \frac{\partial \phi}{\partial n}\frac{\partial^2 \phi}{\partial n \partial s})\mathbf{s} + \\ &(\frac{\partial^2 \phi}{\partial t \partial n} - \frac{\partial \phi}{\partial n}\frac{\partial^2 \phi}{\partial s^2} + \frac{\partial \phi}{\partial s}\frac{\partial^2 \phi}{\partial n \partial s} + \frac{\partial \beta}{\partial s}\mid \nabla\phi \mid^2)\mathbf{n} \end{aligned} \tag{12}$$

In the same way, $\frac{D\phi}{Dt}$ is obtained from (5) and we then get,

$$\begin{aligned} \frac{D^2\phi}{Dt^2} = &\frac{\partial \phi}{\partial s}(\frac{\partial^2 \phi}{\partial t \partial s} + \frac{\partial \phi}{\partial s}\frac{\partial^2 \phi}{\partial s^2} + \frac{\partial \phi}{\partial n}\frac{\partial^2 \phi}{\partial n \partial s}) + \\ &\frac{\partial \phi}{\partial n}(\frac{\partial^2 \phi}{\partial t \partial n} - \frac{\partial \phi}{\partial n}\frac{\partial^2 \phi}{\partial s^2} + \frac{\partial \phi}{\partial s}\frac{\partial^2 \phi}{\partial n \partial s} + \frac{\partial \beta}{\partial s}\mid \nabla\phi \mid^2) - \\ &g(\frac{\partial \phi}{\partial n}\cos\beta + \frac{\partial \phi}{\partial s}\sin\beta) - \frac{1}{\rho}\frac{Dp_a}{Dt} \end{aligned} \tag{13}$$

where $\frac{Dp_a}{Dt}$ is the total rate of change of the surface pressure in time.

After solving the Laplace problem for (ϕ, $\frac{\partial \phi}{\partial n}$) at time t, we can determine the boundary conditions for the ($\frac{\partial \phi}{\partial t}$, $\frac{\partial^2 \phi}{\partial t \partial n}$) problem. Along the free surface, the Bernoulli equation yields,

$$\frac{\partial \phi}{\partial t} = -gz - \frac{1}{2}|\nabla\phi|^2 - \frac{p_a - p_o}{\rho} \qquad \text{on } \Gamma_f(t) \tag{14}$$

and along the fixed boundaries, we get,

$$\frac{\partial^2 \phi}{\partial t \partial n} = 0 \qquad \text{on } \Gamma_b \text{ and } \Gamma_{r2}, (\Gamma_{r1}) \tag{15}$$

Finally, when $\Gamma_{r1}(t)$ represents a plane piston-wavemaker ($\frac{\partial \beta}{\partial s} = \frac{\partial^2 \phi}{\partial n \partial s} = 0$) with velocity u_p, we have,

$$\frac{\partial^2 \phi}{\partial t \partial n} = \left(\frac{d\, u_p(x_p(t),t)}{d\, t} + u_p(x_p(t),t)\frac{\partial^2 \phi}{\partial s^2}\right) n_x \qquad \text{on } \Gamma_{r1}(t) \tag{16}$$

3 Numerical implementation

3.1 *General scheme*

Provided we know the initial conditions at a given time, i.e., the position of the boundary $\Gamma_f(t)$ and ϕ and $\frac{\partial \phi}{\partial n}$ along $\Gamma_f(t)$, we can update the free surface position and the free surface potential to the next time step. When required, the value of $\frac{\partial \phi}{\partial n}$ along the wave generator and its position can also be specified at the next time step (Section 4.2), and the value of $\frac{\partial \phi}{\partial n}$ along the solid boundaries is invariably zero. Hence, boundary values for ϕ or $\frac{\partial \phi}{\partial n}$ can be determined at $t + \Delta t$ and a "*first*" Laplace problem solved which determines ϕ or $\frac{\partial \phi}{\partial n}$ (whichever is unknown) along the entire boundary.

Then, with ϕ and $\frac{\partial \phi}{\partial n}$ known along the free surface, $\frac{\partial \phi}{\partial t}$ can be determined from the Bernoulli equation. Similarly, along the rest of the boundary we can specify $\frac{\partial^2 \phi}{\partial t \partial n}$ and hence determine the necessary boundary values for solving Laplace's equation with respect to $\frac{\partial \phi}{\partial t}$ (and so forth for $\frac{\partial^2 \phi}{\partial t^2}$,..., when $m > 2$). Since the succession of Laplace problems is expressed for the same geometry of the boundary $\Gamma(t)$, the extra computational effort required to solve them is very small.

3.2 *Solution of Laplace equation*

For the solution of the Laplace equation in the form (2), we use the Boundary Element method (BEM) (Brebbia, 1978). Collocation nodes are distributed along the entire boundary to describe the variation of boundary geometry as well as boundary conditions and the unknown functions of the problem. Between the collocation nodes, the variation of all quantities is described by means of shape functions, and for this purpose, the boundary is divided into elements each of which contains two or more nodes.

Spatial discretization : In all computations, quasi-spline elements (2-node) are used on the free surface, linear isoparametric elements (2-nodes) on the lateral boundaries and quadratic isoparametric

elements (3-node) on the bottom. For quasi-spline elements, the geometry is described by regular cubic splines and the field functions ϕ, $\frac{\partial \phi}{\partial n}$, etc..., by linear shape functions. As in finite element methods, mapping of the boundary elements onto reference elements is used and the Jacobian of the mapping function is determined analytically.

To obtain sufficient resolution to describe also the higher frequency oscillations created both by the wave generation and after the wave reflection, the interval Δx between nodes on the free surface is selected considerably smaller than was actually found sufficient by Grilli & Svendsen (1990), for the accurate propagation of a solitary wave over constant depth (in the applications, $\Delta x' = \frac{\Delta x}{d} = 0.25$ to 0.45). Even so, at special instances of rapid development, we came close to the limit of accurate reproduction.

To improve the resolution close to the surface corner, the discretization on boundary Γ_{r2} (slope or vertical wall) is modified at each time step, as suggested by Klopman (1988), according to an exponential law which forces the upper element length (closest to the free surface) to be the same as the one of the last element on the free surface. The other elements on the slope are, accordingly, becoming wider towards the bottom.

Corners : A double node technique (Svendsen 1971, Brebbia 1978) is used in combination with continuity and compatibility relationships, to utilize all information given in the corners by the boundary conditions. The continuity conditions impose uniqueness of the potential at the double-nodes and the compatibility conditions express uniqueness of the velocity vector at the corner, based on the values of $\frac{\partial \phi}{\partial s}$ and $\frac{\partial \phi}{\partial n}$ on both intersecting boundaries (see Grilli & Svendsen (1990) for details about the corner treatments and also for a discussion about surface piercing bodies such as wavemakers).

Numerical integrations : The regular integrals in (2) are computed by Gaussian quadrature, using up to ten integration points per element, and a kernel transformation is applied to the singular integrals which are then computed by a Gauss-like quadrature dealing with the logarithmic singularity. More details about these aspects of the method are given in Grilli, Skourup & Svendsen (1989).

An adaptive numerical integratiòn method is used for improving the accuracy of the regular integrations for the elements close to the corners of the fluid domain. It is based on a binary subdivision of the element to integrate, while keeping the number of integration points constant within each subdivision. Subdivision is performed until the intercept angle of each subdivision with respect to the source point falls under a pre-set value. The same technique is also used when the

distance between two boundaries of the fluid domain tends to vanish (e.g. during wave rundown on a slope). Almost arbitrary accuracy can thus be achieved in the numerical integrations (see Grilli & Svendsen (1990) for details).

Solution of the algebraic system : After being assembled according to the type of boundary conditions (Dirichlet or Neuman), the algebraic system matrix equivalent to (2), is solved for the first Laplace problem by direct elimination (Khaletsky method, see Demidovitch & Marion (1979)). The geometry is identical for both the Laplace problems we need to solve when $m = 2$, so only the right hand side vector needs to be recomputed to solve the second system.

3.3 *Time stepping*

Tangential derivatives : The s-derivatives along the free surface, used in the Taylor expansions, are calculated in a sliding 4th-order isoparametric element independant of the BEM discretization. This provides local continuity on the boundary Γ_f of at least the 2nd s-derivatives (see Grilli, *et al.* 1989).

Temporal discretization : Computations were made in a series of space-time discretizations, for the propagation of *exact* solitary waves over constant depth d (Grilli & Svendsen, 1990). For a spatial discretization with given $\Delta x'$, numerical errors were found to be proportional to $\Delta t'^3$ ($\Delta t' = \Delta t\sqrt{\frac{g}{d}}$), when the mesh Courant number $\frac{\Delta t'}{\Delta x'} \geq 0.5$. This is consistent with the second order accuracy of the time integration. When $\frac{\Delta t'}{\Delta x'} < 0.5$, however, errors were not further reduced by decreasing $\Delta t'$, but varied with $\Delta x'$ only, suggesting that, in this case, errors due to the spatial discretization become dominant over time stepping errors.

Thus, time steps should not exceed $\Delta t' \sim 0.5\Delta x'$. Due to the Lagrangian updating of the free surface nodes, however, the distance between nodes on the free surface can vary considerably, for example during runup-rundown on the slope. Hence, time steps have initially been selected so that $\frac{\Delta t'}{\Delta x'} \simeq 0.2$, and these have been further reduced during wave reflection on the slope (see Appendix A for further details).

4 Wave generation and propagation over constant depth

Dimensionless variables x', z', t' and c' will be used in the following. They are defined by,

$$x' = \frac{x}{d} \ , \ z' = \frac{z}{d} \ , \ t' = t\sqrt{\frac{g}{d}} \ , \ c' = \frac{c}{\sqrt{gd}} \tag{17}$$

where c denotes the wave celerity and d the water depth.

$\frac{H}{d}$	c'	m	e_k	e_p	e_t
0.20	1.09434	1.09765	0.077477	0.072295	0.149772
0.30	1.13752	1.37074	0.148068	0.134314	0.282382
0.40	1.17808	1.60052	0.233938	0.206929	0.440867
0.50	1.21578	1.79148	0.330198	0.285514	0.615712
0.55	1.23339	1.87126	0.380025	0.325134	0.705158
0.60	1.24999	1.93883	0.429220	0.363516	0.792735

Table 1: *Exact* solitary wave data computed with Tanaka's (1986) method : $\frac{H}{d}$ is the wave height, c' the wave celerity, m the wave mass (area in 2D), e_k the wave kinetic energy, e_p the wave potential energy, $e_t = e_k + e_p$ the wave total energy. The unit for the energy results is $\rho g d^3$ and for the mass results ρd^2, both per unit of width.

4.1 *Exact solitary wave*

One main purpose of the computations has been to analyze the runup and reflection of a solitary wave on a vertical wall, and to compare the method with other numerical and analytical methods (Section 5). For this purpose the free surface elevation $\eta(x, t_o)$ and potential $\phi(x, t_o)$ (as in (6)) of solitary waves, which are constant shape solutions of the fully nonlinear constant depth potential flow equations, have been generated using the method of Tanaka (1986). These solitary waves have been termed *exact* solitary waves for short (but are in fact only numerically exact, within the (high) accuracy of Tanaka's method).

Tanaka's method is based on using Cauchy's integral theorem in a frame of reference moving at the celerity c' of the wave, and the crest velocity q_c in that frame defines the wave. Cooker (1989) has modified the method so that the wave height $\frac{H}{d}$ can be prescribed instead of q_c, within the limits $\frac{H}{d}$=0.833197 (or q_c=0) for the highest wave and $\frac{H}{d}$=0 (or q_c=1) for a flat free surface. The modified Tanaka's method determines iteratively the free surface elevation and velocity distribution for a prescribed wave height. *Exact* wave data obtained with Tanaka's method are listed in Table 1.

Before their introduction in the BEM model, the waves are truncated left and right at points where the free surface elevation $\eta = \varepsilon_z H$, with $\varepsilon_z \ll 1$ chosen in advance. The wave truncation and the change from the discretization of Tanaka's method to the BEM discretization induce small adjustments (a few hundredths of a percent) of wave shape $\eta(x', t'_o)$, potential $\phi(x', t'_o)$ and normal velocity $\frac{\partial \phi}{\partial n}(x', t'_o)$, at the first time step of the BEM computations. Results for later times show, the numerical model can propagate *exact* solitary waves over long distances of constant depth while

conserving their shape, mass and total energy constant within a very small margin ($< 0.01\%$). In the brief interval of the rapid surface movements during reflection from a wall or slope, however, errors in mass and total energy temporarily increase (up to 0.1% for the highest wave $\frac{H}{d}$=0.6).

Details of numerical data and checks of accuracy for the *exact* waves are given in Appendix A.

4.2 *First order solitary wave*

A second main purpose of the computations reported in this paper has been to compare the numerical results to the measurements of Losada, *et al.* (1986) (LVN) (Section 6). They generated waves, in their laboratory wave tank, by moving a piston wavemaker according to Goring (1978) first-order solitary wave solution. We have reproduced that process as closely as possible in the numerical experiments made for comparing with their measurements, and the solitary waves generated that way have been termed *first-order* waves, for short.

In a wave of permanent form, we have at any instant (Svendsen & Justesen, 1984),

$$\int_{-d}^{\eta} u \ \mathrm{d}z = c_a \eta + Q_s + Ud \tag{18}$$

where c_a is the propagation speed of the wave in a fixed frame of reference, $\eta(x,t)$ is the wave elevation above the still water level, Q_s is the mass flux averaged over a wave period, and U, the speed of the current defined as the averaged particle velocity below wave trough level (Phillips, 1977).

In a solitary wave, the period is infinite, so Q_s becomes zero. Hence, with no current, $c_a = c$ and the right hand side of (18) simply reduces to $c\eta$ where c is the relative or "intrinsic" celerity of the wave. Thus, (18) equals the simpler expression used by Goring (1978) for determining the motion required by a piston wavemaker to generate a specified water surface elevation immediately in front of the wavemaker. Since the piston motion creates a depth uniform horizontal velocity $u_p(x_p(t),t)$ (18) reduces to,

$$u_p\,(d+\eta) = c\eta \tag{19}$$

which means that a required η can be generated by a piston velocity,

$$u_p = \frac{c\,\eta(x_p,t)}{d+\eta(x_p,t)} \tag{20}$$

This corresponds to a piston motion $x_p(t)$ given by,

$$x_p(t) = \int_0^t \frac{c\,\eta(x_p,\tau)}{d+\eta(x_p,\tau)} \ \mathrm{d}\tau \tag{21}$$

To generate a first-order solitary wave profile with,

$$\eta(x,t) = H\,\mathrm{sech}^2[\frac{\kappa}{d}(x-ct)] \tag{22}$$

$$c = \sqrt{g(d+H)} \tag{23}$$

$$\kappa = \sqrt{\frac{3H}{4d}} \tag{24}$$

(22)-(24) have to be substituted into (21) with $x = x_p(t)$ required throughout the integration in order to account for the finite amplitude of the piston [1] (see Grilli & Svendsen (1990) for detail).

4.3 *Propagation of the first-order waves*

Both energy and mass are well conserved also during propagation of the *first-order* waves (errors of the order of those of the *exact* waves are typically obtained in computations with identical discretizations). However, theoretical *first-order* profiles as given by (22), are never obtained in the fully nonlinear computations. For waves of appreciable height, the free surface elevation produced by the wavemaker is not quite an exact solution of the nonlinear problem solved in the model (i.e., an *exact* solitary wave). Computations show, the water elevation starts adjusting its shape long before the piston motion is completed and the wave disintegrates into a leading wave and an oscillatory tail. This is also observed in LVN's laboratory experiments. In fact, within the frame of Boussinesq's approximation, the inverse scattering theory would have predicted similar results for a wave that does not corresponds to a solitary wave for the Boussinesq equations. A distributed elevation of the free surface will disintegrate into one or more solitons and a tail of disturbances (Hammack & Segur, 1974).

In the nonlinear model, the deviations between the wave motion generated and an *exact* solitary wave are essentially associated with two aspects : the piston generates the flow of a KdV solitary wave, i.e., a horizontal velocity constant over depth, which is not quite the case in a steep *exact* solitary wave, and the amplitudes of the wave considered are too large for the KdV type approximation of the flow (like (22)) to give an accurate prediction of the surface profile. In fact Goring (1978) found, in his experiments, that the limit for an accurate solitary wave reproduction by his method was $\frac{H}{d} \simeq 0.2$. For larger amplitudes, the profile (22) deviates more and more from an *exact* solitary wave of the same height.

[1] Most wavemaker theories describe the solution to the problem : What is the wave motion generated by a specified paddle motion. It may be interesting to notice that the procedure described above is the only one (known to the authors) for solving the "inverse" wave generation problem : How do we move the wave maker to generate a wave of a specified (arbitrary) form. Recently Synolakis (1990) has generalized Goring's wavemaker method to the generation of arbitrary finite-amplitude long waves, by solving an inverse evolution problem of the KdV equation.

Figure 2 shows computed profiles of waves with four different amplitudes H_i (Figure 1) at the (different) time when the crest of each of them passes a point I, $20d$ in front of the wave generator. In accordance with the comments above, it is found that the higher the waves, the more pronounced is the amplitude A (Figure 1) of the tail of disturbances they are shedding. A closer inspection also shows that, although the highest parts of the crests are closely symmetric, there are non-negligeable differences between front and rear for the lowest 25-35 % of each leading wave profile. All these features have been qualitatively observed in LVN's experiments, although detailed comparison has not been made.

As the waves propagate further away from the wave generator, the asymmetry of the leading wave decreases and the part of the tail closest to the wave turns into a long, shallow trough. Figure 3a shows this in a comparison between two waves of the same height ($\frac{H_i}{d}$=0.25), one having propagated only $20d$ since generated, the other after $86.7d$. Figure 3b shows a comparison between the leading wave after propagation over $86.7d$ (as in Figure 3a) and an *exact* solitary wave of the same height. One sees the differences between both profiles are significantly reduced. The slow transformation of the wave profile as it propagates and adjusts itself to a stable form also results in a moderate decrease in wave height. Figure 4 shows the amplitude variation for the 2 waves of Figure 3a, which were generated at $x' = 0$ and 66.7 in such a way that their their amplitude is the same at $x' = 86.7$. Although the computations clearly have not been carried far enough, it seems likely that the wave generated at $x' = 0$ will eventually stabilize at a height only marginally smaller than that found at $x' = 86.7$ where we stopped this computation. Figure 4 also shows that the wave in Figure 3a, generated at $x' = 66.7$ by the piston wavemaker was initially generated slightly smaller. Finally it is mentioned that, as one would expect, we also find that the transformation occurs much faster for the highest waves than for the smaller waves.

The wave motion in a wave flume should be expected to behave precisely the same way as in the numerical solution of the fully nonlinear equations (except for the bottom and sidewall friction, which will be negligible for the situations considered, see Section 4.5). As will be shown in the comparison with LVN's experiments (Section 6), this is in fact the case when we closely duplicate the way the laboratory waves are generated.

4.4 *Celerity of the first-order waves*

A relative difference in celerity c' is found between the *first-order* waves (Table 3) and the *exact* waves (Table 1). It is positive and quite small ($< +0.06\%$), up to amplitudes of $\frac{H}{d}$=0.2 where the differences in profile are small (Section 4.3). The difference remains small up to $\frac{H}{d}$=0.456

($< +0.40\%$) and grows near $+1.00\%$ for the highest waves considered. Hence in all cases it is found that the *first-order* waves travel faster than *exact* waves of the same height, likely so because they are bulkier and show less frequency dispersion.

4.5 *Remark on the friction*

It may also be worthwhile briefly to comment on the fact that the method does not include frictional effects in its present form. Friction will occur along the solid boundary at the bottom and the slope where a boundary layer will develop. This will clearly dissipate some of the wave energy, and if longer distances of propagation are considered, the cumulative effect may be quite important for which wave height actually reaches the slope [2]. As usual, however, locally friction has only a negligible effect on the wave motion. In particular, on a smooth slope as considered here, the influence of friction on the highly inertia dominated runup and reflection process must be expected to be of virtually no consequence. Only at the uppermost tip of the runup, would some frictional effect be expected. The problem was studied by Packwood & Peregrine (1981).

5 Reflection from a vertical wall

Before considering the reflection from a slope, we analyze the more simple reflection from a vertical wall and compare it with the results, Fenton & Rienecker (1982) (F&R) obtained for that situation using a Fourier Method, with the 3rd-order analytic solution of Su & Mirie (1980) (S&M) and with the 5th-order analytic solution of Byatt-Smith (1988) (B-S). Reflection of both *exact* and *first-order* solitary waves of amplitude ranging from $\frac{H}{d}$=0.2 to 0.6 is computed. The *exact* waves will allow for a direct comparison with S&M, F&R and B-S results, whereas the *first-order* waves, which represent the waves generated in the laboratory experiments, will be used to show how close to the *exact* wave runup these waves can be expected to be.

Notice, since the amplitude of a *first-order* wave slightly decreases during propagation (Figure 4, Section 4.2), the initial amplitude imposed at the wavemaker is adjusted so that the desired value of the incident wave amplitude $\frac{H_i}{d}$ is obtained at a given position x' (the slightly higher initial wave to be imposed to the wavemaker is determined by trial and error). A location $13.3d$ in front of the vertical wall is selected for the incident wave as in LVN's experiments (x'=20, Figure 1). At that location, the effect of the wall is not yet too sensitive on the incident wave.

[2] The way the comparisons with the experiments will be set up here (Sections 5, 6), the effect is virtually nil, since the initial wave height $\frac{H_i}{d}$ used as reference for the computations with the *first-order* waves is measured at quite a short distance from the slope ($13.3d$), which eliminates the effect friction has during most of the propagation in the much longer physical wave tank used by LVN ($L \simeq 160d$).

$\frac{H}{d}$	$\frac{R_u}{d}$	$\frac{R_d}{d}$	F_x^{max}	M_b^{max}
0.20	0.42920	0.00058	1.8775	2.6486
0.30	0.66873	0.00179	2.3058	3.7220
0.40	0.93673	0.01758	2.6809	4.8077
0.50	1.25308	0.05250	3.0693	5.9454
0.55	1.47937	–	3.2808	6.6075
0.60	1.67100	–	3.5034	7.3471

Table 2: *Exact* solitary waves BEM results (dimensionless variables) : $\frac{R_u}{d}$ is the maximum runup value, $\frac{R_d}{d}$ the rundown, F_x^{max} the maximum horizontal pressure force and M_b^{max} the maximum moment with respect to the toe of the wall on the bottom. The units for the forces and moments are $\frac{1}{2}\rho g d^2$ and $\frac{1}{6}\rho g d^3$ per unit width, respectively.

$\frac{H_i}{d}$	$\frac{R_u}{d}$	$\frac{R_d}{d}$	F_x^{max}	M_b^{max}	c'
0.200	0.425	0.003	1.864	2.623	1.095
0.255	0.547	0.007	2.093	3.172	1.121
0.300	0.654	0.015	2.257	3.625	1.136
0.400	0.910	0.038	2.638	4.685	1.183
0.456	1.074	0.055	2.844	5.280	1.204
0.500	1.215	0.068	3.031	5.806	1.228
0.600	1.583	–	3.402	6.999	1.260

Table 3: *First order* solitary waves BEM results (dimensionless variables) : $\frac{H_i}{d}$ is the incident wave at $x' = 20$ ($13.3d$ in front of the wall), and the other results are defined as in Table 2.

Numerical data and checks of accuracy of the computations with the *exact* waves are given in Appendix A.

5.1 *Runup*

One might expect that, for a *first-order* wave, the oscillatory tail would not influence too much the runup but would have a more significant effect later on in the reflection process when the tail meets with the reflected wave. Figure 5 shows the envelope of the maximum surface elevation of a *first-order* wave as it approaches the wall and after it has been reflected. The wall is placed at $x' = 100$ and results are shown for the same two waves as in Figure 3a and 4 ($\frac{H_i}{d}$=0.25), to indicate the effect which the small differences between those two waves have on the maximum elevations and after reflection. The two waves have almost equal runup values and both come out of the reflection process with a somewhat smaller amplitude. Notice that only the variation of maximum

elevation is shown, not the envelope of the free surface positions. The maximum elevation is at the wall throughout the time it takes the surface to move from A to B (maximum runup) and back to A'. That results in the spike from the highest position A near the wall to the runup position B at the wall. Immediately after reflection, the amplitude decrease is almost 10%, but at some distance from the wall it settles at 3-5 %. This is comparable to the approximately 3 % decrease found by F&R, though the results for the reflected wave show some variation (as expected) due to the interaction with the incoming tail. This transient decrease of the wave amplitude after reflection will be studied in detail, for an *exact* wave of $\frac{H}{d}$=0.5, in Section 5.2.

In Figure 6, the maximum elevation ("runup", R_u) at the wall, computed for different amplitudes of the *exact* and *first-order* waves is compared to the 3rd-order results by S&M and to the F&R's computations (the BEM results are also in Table 2 and 3).

Up till amplitudes about $\frac{H}{d}$=0.4, the BEM results for the *exact* waves are almost identical with those of S&M and F&R. Above that value, the 3rd-order theory predicts slightly smaller runup implying that for high waves ($\frac{H}{d} > 0.4$) the runup, contributions of order higher than third in $\frac{H}{d}$ are important. This ties well in with B-S's results that show that other effects occuring during wave reflection are at least of 5th-order in $\frac{H}{d}$(Section 5.2). The Fourier method by F&R coincides very closely with the present results even for the highest wave of amplitude 0.5161 computed by that method (in spite of F&R's own comment about the reduced accuracy of their method for ampitudes above 0.4554).

The runup of the *first-order* waves is slightly smaller than for the *exact* waves, for amplitudes $\frac{H}{d} \geq 0.3$. This is likely due to the effect of the oscillatory tail the *first-order* waves shed behind them which, for sufficiently high waves, removes enough energy from the leading wave to reduce its runup significantly.

BEM results for the reflection of *first-order* waves from a steep slope will be compared in Section 6 with detailed experiments made by LVN. Some of these experiments correspond to a vertical wall and their results are listed in Table 4 (LVN). The corresponding computations are listed in the same Table (BEM). It appears that computed and measured runup values $\frac{R_u}{d}$ agree quite well (within 4.8% and 3.0% for waves of $\frac{H}{d}$=0.255 and 0.456 respectively).

5.2 *Rundown and reflected wave*

Rundown : Figure 7 shows the maximum depression of the water surface as a function of the wave amplitude ("rundown" or "rush-down", R_d) for both *exact* and *first-order* waves (these results are also in Tables 2 and 3). It appears, the rundown value is significantly higher for the *first-order*

Type	$\frac{H_i}{d}$	$\frac{H_r}{d}$	K_r	$\frac{\mathcal{R}_u}{d}$	$\frac{\mathcal{R}_d}{d}$
LVN	0.255	0.224	0.882	0.521	0.003
LVN	0.456	0.419	0.918	1.107	0.059
BEM	0.255	0.247	0.964	0.547	0.007
BEM	0.456	0.417	0.915	1.074	0.055

Table 4: *First-order* solitary wave reflection from a vertical wall : Experimental results from Losada *et al.* (1986) (LVN) and computations (BEM), with $\frac{H_i}{d}$ the height of the incident wave at $x = 20d$ and $\frac{H_r}{d}$ the height of the reflected wave measured at the same x location, $\frac{\mathcal{R}_u}{d}$ and $\frac{\mathcal{R}_d}{d}$ the runup and rundown of the wave, and $K_r = \frac{H_r}{H_i}$ the reflection coefficient.

waves (in particular for $\frac{H}{d}$<0.3) probably due to superposition with the shallow trough following those waves in their (incoming) oscillatory tail (Figures 3a and 5). The highest *exact* waves also develop negative surface elevation after reflection, as a start of the (actual) oscillatory tail which is created for those waves by the reflection process.

Rundowns have been measured on a vertical wall for *first-order* waves, in the experiments by LVN. They are listed in Table 4 (LVN), along with the numerical results for the same waves (BEM). Although the very small rundown of the smaller wave is not quite well predicted, the rundown measured for a wave of $\frac{H}{d}$=0.456 agrees to within 5% with the computed value.

Reflected wave : Figure 8 shows computed profiles of *exact* waves of height 0.2 to 0.5, reflected from the wall at $x' = \frac{L}{d}$ (Table 7). The various x' locations of the maximum crests have been selected, to get a good picture of the development of the reflected waves. One clearly sees oscillatory tails develop behind the reflected waves, and increasingly so for increasing $\frac{H}{d}$ (for $\frac{H}{d}$=0.5, the maximum depression in the tail is close to 10% of the wave height, a value similar to the corresponding R_d in Table 2). Both S&M and B-S theoretically predicted that, to the 3rd-order in $\frac{H}{d}$, an oscillatory tail should appear after reflection. F&R, however, could not produce oscillatory tails in their computational results, presumably due to their Fourier method which essentially assumes that their waves are periodic (see comments by B-S).

Figure 9a shows a comparison between an *exact* wave of $\frac{H}{d}$=0.5, at its initial location x'=14 (or $14d$ from the vertical wall positioned at $x' = \frac{L}{d} = 28$), and the corresponding reflected wave which propagates back through the same location. A decrease in wave height after reflection is observed ($\Delta\frac{H}{d}$=0.0313 or 6.2% of $\frac{H}{d}$), and a well developed oscillatory tail follows the leading wave. Before analyzing this further, notice that the reflected wave height $\frac{H_r}{d}$ measured in LVN's experiments at $13.3d$ from the vertical wall, for a *first-order* wave of $\frac{H_i}{d}$=0.456, gives a decrease in height of 8.1%

with respect to the incident wave (Table 4 (LVN)). Our computation for the same wave (BEM) agrees to within 0.5% with this result. Although that wave is not quite an *exact* solitary wave and is slightly smaller in height, this experimental result at least qualitatively, also confirms the present computational observations.

Maximum amplitude reduction : A more detailed picture of the variation in wave height following the wave after reflection is shown in Figure 9b (solid line), for the same wave of initial amplitude $\frac{H}{d}$=0.5. We see, there is an initial reduction of the maximum amplitude, of about $\Delta\frac{H}{d}^{max} = 0.0556$, around the time of the maximum rundown ($t'(R_d)$, Table 5), after which the maximum amplitude of the reflected wave is continuously increasing. F&R, although they did not get an oscillatory tail, obtained a 3rd-order reduction in the wave amplitude after reflection, by curve fitting to their numerical results : $\Delta\frac{H}{d}^{max} \simeq 0.4(\frac{H}{d})^3$ which, for $\frac{H}{d}$=0.5, yields $\Delta\frac{H}{d}^{max} = 0.05$, in good agreement with our result. Seabra-Santos (1985) confirmed F&R's approximate relationship in his experiments, as well as the slow increase in amplitude, when the reflected wave propagates backwards in the wave tank. B-S derived an analytic expression for the transient change in amplitude of the wave after reflection and showed that the oscillatory tail is responsible for this reduction (a simple energy balance demonstrated that the leading reflected wave gives energy to the oscillatory tail at the time of the reflection and that, accordingly, its amplitude decreases of $\Delta\frac{H}{d}^{max}$). B-S's results confirmed that the change in amplitude is proportional to $(\frac{H}{d})^3$. In particular, the maximum amplitude reduction measured from his Figure 1 and scaled for our case by 0.125 ($\frac{H}{d}$=0.5), yields $\Delta\frac{H}{d}^{max} \simeq 0.0612$, which is also in good agreement with our result. Notice, finally, S&M did not find any reduction in wave amplitude to the 3rd-order in $\frac{H}{d}$, and Mirie & Su (1982) found a reduction in amplitude of less than 3rd-order in $\frac{H}{d}$.

Transient loss in amplitude : The reflection considered by B-S is obtained by analyzing the situation when two opposing waves of the same height meet. He developed analytic expressions to 5th-order for the tail of oscillations, but had to introduce the additional approximation that the phase ξ_2 of the "reflected" wave is infinitely large, even at limited time τ_2 after the meeting of the crests. A complete comparison with the expression derived by B-S for the transient loss in amplitude has been made by relating his time scale τ_2 to our dimensionless time scale t'. Measuring on the curve from B-S's Figure 1 after scaling both axis, we obtain the dashed curve in Figure 9b, where t'_2 is the time when, in our computations, the reflected wave leaves the wall (defined when $\frac{H}{d}$ =0.5 or $\Delta\frac{H}{d}$ =0). The agreement between the curves in this Figure is quite good for large $(t' - t'_2)$ but the discrepancies are larger when $(t' - t'_2)$ (or τ_2) is small. We believe this is partly due to the effect of

the limited order of B-S's analysis (5th-order in $\epsilon=\frac{H}{d}$) whereas we solve the equations exactly, and partly due to the asymptotic hypothesis B-S makes for deriving his analytical expressions ($\xi_2 \rightarrow \infty$ at a fixed time τ_2), which corresponds to the "reflected" wave being far from the "wall".

Although the amplitude of the reflected wave recovers somewhat as the wave moves away from the wall, it will not return to its initial value, however, because a certain amount of energy is permanently lost to the tail.

Oscillatory tail : This is further illustrated in Figure 9c (solid line) which shows the difference between the incoming wave and the reflected wave of Figure 9a (at x'_o=14 for t'=23.525). It is seen that the difference wave consists of a depression under the crest of the main wave, accounting for the transient reduction in amplitude $\Delta\frac{H}{d}$, and the tail of the reflected wave. In Figure 9c is also shown B-S's 5th-order expressions for the oscillatory tail (dashed line). B-S's τ_2 has been calculated and the situation has been chosen at a time step of our computations with $\tau_2 = 3.04$, which corresponds closely to the τ_2 values of 3 of B-S Figures 2d [3]. This also corresponds to a situation where the reflected wave is $14d$ (i.e. $28 - x'_o$) from the wall, which means that B-S assumption of large phase is reasonably well satisfied. The similarity between the results of the two methods is apparent although there also are some significant differences. In particular the agreement between both the curves in the Figure is quite good around the maximum of the main wave (wave of depression at $x'_o - x' = 0$). B-S theory predicts, however, a much less pronounced decay rate for the tail than does the numerical computations, perhaps because that part of the tail is closer to the reflection point and hence is likely to invalidate the large phase assumption (when x' increases the tail gets closer to the wall).

5.3 *Celerity and phase shift*

A phase diagram equivalent to F&R's Figure 10 has been developed for the *exact* wave of $\frac{H}{d}$=0.5 considered in Figure 9. The solid line in Figure 10a represents the relationship between t' and x' for the point of maximum wave amplitude $\frac{H}{d}$ determined as in Figure 9b, and the wave celerity is given by the reciprocal of its slope (its lower part corresponds to the wave before reflection, and its upper part to the wave after reflection).

The lower and upper dashed lines in the Figure are the best fits to the results for $x' < 20$, and give a measure of the average incident and reflected wave celerity respectively : $\overline{c'_i} = 1.2168$ and

[3] By comparing B-S Figures 1 and 2 and considering his equation (6.11), there seems to be a factor two error in B-S's Figure 2. We believe, Figure 2 is actually a plot of $2\tilde{u}_1(\xi_1, \tau_2)$ and should thus be scaled by a factor $\epsilon^3 = (\frac{H}{d})^3$ (like in B-S's Figure 1) rather than by $2\epsilon^3$ as indicated by B-S.

$\overline{c_r'} = 1.2226$. The celerity $\overline{c_i'}$ is slightly larger (0.085%) than the theoretical value in Table 1, and corresponds to an average incident wave height (over x'=14 to 20) $\frac{H_i}{d} = 0.5008$. This slight increase in height is likely to be due to the small adjustments of the *exact* wave to the BEM discretization, already mentioned in Section 4.1.

Alhough it is of smaller amplitude (Section 5.2), the average reflected wave is found to be $\frac{\Delta c'}{\overline{c_r'}}$=0.47% faster than the incident wave. A higher celerity after reflection has been observed in Seabra-Santos' (1985) experiments, as well as in F&R's numerical result, who interpreted it as being an effect of the unsteadiness of the wave after reflection (F&R, however, computed a much larger increase in celerity than ours : they found $\Delta c' \simeq 0.64(\frac{H}{d})^3$, or $\frac{\Delta c'}{\overline{c_r'}}$=6.56% for the case discussed here). Figures 9b and 10a indeed show, wave height and celerity substantially change after reflection and over an horizontal distance of several depths. Figure 10b is a closer view of the right part of Figure 10a ($x' \geq 24$). Notice, the large increase in celerity near the wall, before and after reflection, is mainly a geometric effect which could be reproduced quite well, just by linearly superposing two first-order profiles (22). B-S further points out that, since wave celerity is a monotonic increasing function of $\frac{H}{d}$(when the waves are not close to the maximum), a solitary wave having reached its permanent form cannot be smaller and faster. According to his asymptotic results, the reflected wave should recover its initial height when time tends to infinity, hence its speed.

Our results show that, right after reflection, highly transient phenomena take place which can cause the wave to be temporarily smaller and faster. As time passes, the leading reflected wave partially recovers its height and approaches permanent form. Part of its energy, however, has been *irreversibly* transmitted to the oscillatory tail, and since energy is also a monotonic increasing function of $\frac{H}{d}$ the leading wave cannot recover its initial height. Hence, after a very long time, a permanent reduction in amplitude should be observed along with a wave celerity smaller than $\overline{c_i'}$ (unlike BS's theory predictions). Computations, however, have not been pursued long enough for this last stage to be observed.

Figure 10b also shows the phase shift of the wave, during reflection, which leads to a time phase lag $\Delta t'$=0.627, measured between B and C on the wall (identified by the intersection with the lines representing $\overline{c_i'}$ and $\overline{c_r'}$) and to an instantaneous spatial phase lag $\Delta x'$=0.763, measured between C on the wall and E on the line B-F representing a perfect reflection of the incident wave. With slightly different celerities before and after reflection, B-F and C-G will, in theory, eventually intersect as time increases, thus $\Delta t'$ and $\Delta x'$ will gradually vanish. However, since the celerity of the reflected wave should eventually decrease as the wave stabilizes its shape, permanent but

$\frac{H}{d}$	e_{ko}	$10^4\Delta^T e_k$	$\frac{e_k^{min}}{e_{ko}}(\%)$	$\Delta^{R_u}t'$	$\frac{\Delta e_k}{e_{ko}}(\%)$	$t'(R_u)$	$t'(R_d)$
0.20	0.077480	0.36	0.0259	0.045	0.068	17.82	29.34
0.30	0.147953	7.74	0.1167	0.070	0.159	15.02	25.90
0.40	0.233696	10.4	0.3520	0.120	0.301	12.54	17.10
0.50	0.329923	8.33	0.7859	0.200	0.543	12.05	16.18

Table 5: *Exact* solitary wave variation in kinetic energy in the computations (dimensionless variables) : e_{ko} is the wave kinetic energy at the first time step and $\Delta^T e_k$ its difference from exact (Tanaka's) result, $\frac{e_k^{min}}{e_{ko}}$ is the relative minimum of the kinetic energy during runup and $\Delta^{R_u}t'$ the (negative) time difference from the time of maximum runup $t'(R_u)$ at which this minimum occurs, $\frac{\Delta e_k}{e_{ko}}$ is the drop in kinetic energy corresponding to the first relative minimum after the time of rundown $t'(R_d)$ (point A in Figure 11b).

reduced time and space phase lags should be observed in the long term.

The phase shift observations tie qualitatively well in with the results by Maxworthy (1976), Oikawa & Yajima (1973), S&M, and F&R. S&M estimated immediate and long term time and space phase lags, to the 3rd-order in $\frac{H}{d}$. From their analysis we get for $\frac{H}{d}$=0.5, values of $\Delta t'$={1.505 ,0.485} and $\Delta x'$={1.607,0.587} for the immediate and long term phase lags, respectively. Thus, their immediate values are more than twice our results. F&R did not compute lags for a wave of $\frac{H}{d}$=0.5 (they did not trust their results for $\frac{H}{d}\geq$0.45) but they got results increasing with $\frac{H}{d}$ and obtained $\Delta t'$=1.12 for $\frac{H}{d}$=0.4554. Hence, they also got much larger results than ours.

5.4 *Energy partition*

Figure 11a shows the variation in time of both the kinetic energy e_k and the potential energy e_p, computed for an *exact* wave of $\frac{H}{d}$=0.5; e_{ko} represents the kinetic energy of the wave at the first time step after the start of the BEM computations and $\Delta^T e_k$ is the slight shift this represents from the initial Tanaka's value at time t'_o=0 (Table 1) caused by the shift to the BEM numerical scheme (e_{ko} and $\Delta^T e_k$ are given in Table 5 as function of $\frac{H}{d}$). We see on the Figure that the kinetic energy reaches its minimum e_k^{min} a fraction of a time unit ($\Delta^{Ru}t'$) before the time of maximum runup ($t'(R_u)$) and that it never becomes quite zero. Also it is seen (Table 5) that both these variables increase with $\frac{H}{d}$. In fact, computational results show that the flow is at no time at rest at all points of the wave.

If we look closer at the energy partition we see in Figure 11b that, before the time of rundown, there is a small portion of the curve where $e_k > e_{ko}$, and this corresponds, in Figure 9b, to a region

where the reflected wave amplitude is close to minimum. This transient increase in kinetic energy also happens at the same time as the wave shows a higher celerity (Section 5.3).

After rundown at $t'(R_d)$, we see on Figure 11b, there is a decrease in kinetic energy, Δe_k, on a more or less permanent basis (there actually is a slight increase on a longer term basis). Table 5 shows this decrease in kinetic energy is an increasing function of $\frac{H}{d}$. We believe, the decrease, likely, is an effect of the energy transmission to the oscillatory tail, during reflection. F&R also observed a slight decrease in the kinetic energy. For a wave height of 0.2134 they found $\frac{\Delta e_k}{e_{ko}}$=0.135% against $\sim$ 0.092% in our computations (by interpolation).

5.5 *Horizontal forces and moments*

F&R computed total maximum horizontal forces and moments (with respect to the bottom) of waves acting on the wall, and S&M calculated them to the 3rd-order in $\frac{H}{d}$. Figure 12a and b show a comparison of our BEM solution for both *exact* and *first-order* waves with these results (our results are also listed in Table 2 and 3). F_x represents the horizontal pressure force on the wall, calculated by the Bernoulli equation (14) integrated over the wall, made dimensionless by dividing it by the hydrostatic pressure force at still water level : $\frac{1}{2}\rho g d^2$ and, similarly, M_b represents the moment with respect to the bottom of the wall divided by $\frac{1}{6}\rho g d^3$. In view of the close agreement observed for the runup values (Section 5.1), it is not surprising that our BEM computations for the *exact* waves give results that coincide very well with the earlier results by S&M and F&R up to a wave of $\frac{H}{d}$=0.5. For higher waves, slightly higher values are (again) obtained with the *exact* waves.

A somewhat surprising result is a double maximum found in the time variation of the total force (and moment) for high waves as shown in Figure 13a for the *exact* waves (similar results were also obtained for the *first-order* waves). A wave of $\frac{H}{d}$= 0.4 already shows signs of an extended maximum, and for $\frac{H}{d}$= 0.5 there are distinctively two extremes on the force curve. For higher waves ($\frac{H}{d}$=0.55 and 0.6), the computations broke down at the time of the second maximum in a situation with essentially zero pressure and a free falling water volume near the crest. No attempt was made to investigate this further.

Figure 13b shows details for the wave of $\frac{H}{d}$=0.5 and gives a picture of the force F_x, moment M_b and the surface elevation at the wall η' as a function of time t'. One sees F_x first reaches its absolute maximum F_x^{max}, then M_b reaches its absolute maximum M_b^{max}. Both F_x and M_b reach local minima, slightly after the maximum runup R_u=1.253 at $t'(R_u)$=12.05, and, finally, second maxima slightly smaller than the first.

It is interesting that Nagai (1969) experimentally observed similar double maxima in the hori-

Type	θ	$\frac{H_i}{d}$	$\frac{H_r}{d}$	K_r	$\frac{\mathcal{R}_u}{d}$	$\frac{\mathcal{R}_d}{d}$
LVN	70°	0.259	0.232	0.893	0.568	0.004
LVN	70°	0.437	0.402	0.920	1.071	0.103
LVN	45°	0.269	0.214	0.796	0.672	0.129
LVN	45°	0.457	0.347	0.759	1.294	0.267
BEM	70°	0.259	0.243	0.937	0.580	0.013
BEM	70°	0.437	0.376	0.861	1.066	0.099
BEM	45°	0.269	0.224	0.833	0.673	0.134
BEM	45°	0.457	—	—	1.262	0.186

Table 6: *First-order* solitary wave reflection from a slope θ. Definitions are as in Table 4.

zontal force exerted on vertical walls by steep standing periodic waves in shallow water.

6 Reflection from a steep slope

6.1 *Description of Experiments by Losada, et al.*

Losada et al. (1986) (LVN) have reported detailed measurements of the runup and reflection of solitary waves from steep plane slopes, in a tank 48.0m to 49.6m long, with a water depth over the horizontal part of d=0.3m. Their experimental facility was equivalent to the arrangement shown in Figure 1 except that the length of the flume was $L = 160$ to $165d$. The wave generation was ensured by a piston wavemaker controlled by a computer, providing displacements according to Goring's (1978) solution (21)-(24), with truncation $\varepsilon_z = 0.002$. Error sources in the experiments were some losses of water observed during the piston motion, through gaps between the sides of the piston wavemaker and the tank walls. These were negligible, however, for waves with $\frac{H}{d} > 0.15$. The results of LVN consist of time series of surface elevation recorded by capacity wave gauges with a sampling frequency of 33 to 75 Hz, at 16 to 21 positions, primarily in the neighborhood of the slope. Also, the runup itself was recorded. Three wave gauges were used at a time, at different positions, in identical repetitions of each experiment. A high degree of repeatability of the experiments was observed in the results. Points from different experiments could not be dissociated, within the accuracy of the recording device.

The experiments included (*first-order*) solitary waves with $\frac{H}{d} \simeq 0.065$, 0.267 and 0.457, on four different smooth slopes $\theta = 17.9°$, 45°, 70° and 90°. In our comparisons we will concentrate on the results for the two steepest waves. We shall also omit the 90° case (which was discussed in Section 5), and the results for 17.9° where all but the smallest waves break. Our computer

program is capable of handling breaking (see Grilli, *et al.* (1989), Grilli & Svendsen (1989, 1990)), but computations have to be interrupted at least when the jet plunges into the surface below. No such experimental measurements, however, were available in LVN's experiments.

6.2 *Comparison with experimental results by Losada, et al.*

The computational region for our comparison with Losada's experiments has the dimensions shown in Figure 1. To reduce the amount of computations, our results are obtained for a flume with a length $L = 33.33d$, i.e. the distance from our wavemaker to the still water level intersection with the slope is 33.33 times the depth (or 10m with LVN's dimensions). This is only about one fifth the length of Losada's wave basin. The minor inaccuracies this leads to are almost entirely concentrated in the tail following the wave as was discussed in Section 4. Hence, the major effect of the reduced computational region is a limitation in the time over which we can meaningfully compare our results with those of Losada's : In our computations the tail meets the reflected wave somewhat before it does in the experiments. As will be seen in the following, however, this does not constitute a major problem since most of the evolution takes place before that time. It is also found that a new trailing system of high frequency oscillations, quite stronger than in the reflection from a vertical wall, is generated by the runup and reflection process from a slope. In spite of the above mentioned effects of the shortening of the computational wave flume we find that computations compare very favorably with the measurements even for those high frequency parts of the wave motion.

The comparison has been made for the cases of slope angle 45° and 70° for which even relatively steep waves do not break. As detailed in Section 4.2, in our computations we generate the *first-order* waves at $x' = 0$ (i.e., 33.3 water depths from the slope) by simulating a piston-type wavemaker motion, according to Goring's procedure. The amplitude of the wavemaker is adjusted so that when the wave passes $x' = 20$ (i.e., $13.3d$ from the slope) it has a height $\frac{H_i}{d}$=$\{0.269,0.259\}$ or $\{0.457,0.437\}$, for θ=$\{45°, 70°\}$, as found in the experiments at that point.

In all cases, the computed and measured results have been synchronized at the time of maximum runup which, in the experiments reported, is the only well-defined time available. The form of the wave, however, at that time entirely results from the generation and propagation which preceed the runup (as described in Section 4.3). Though comparisons can be made before the time of maximum runup, experimental results are only available from the time of runup onward, except for θ=70° (Figure 15), where an extra experimental profile was available at a time somewhat before maximum runup and was used in the comparison.

Table 6 shows experimental (LVN) and computed (BEM) results for both the wave heights and the slopes considered here. One sees the maximum runup values $\frac{R_u}{d}$ are in good agreement (within 2.5% for $\theta = 45°$ and 2.0% for $\theta = 70°$). The agreement for the rundown figures $\frac{R_d}{d}$ is somewhat less good but it should be noted that LVN found this quantity quite difficult to measure.

Runup and rundown figures are, in fact, only values of the wave elevation at one point of the free surface. It is far stronger a test to compare complete computed free surface elevations with those measured in the experiments. This is first done in Figures 14a and 14b which show how the two considered waves reflect from a 45° slope. The computations are compared with the surface profiles measured by LVN at three different times, of which the first available is the instant of maximum runup (curves a) used for synchronization. In general, the agreement is considered good.

In Figure 14a, however, results do not quite coincide at the time of rundown (curve c). The agreement is somewhat better with a profile computed at a time slightly before the instant of rundown (curve b) (i.e., 0.48 time units or 0.084s in the experiments). As pointed out by LVN, both rundown and instant of rundown are quite difficult to measure since the surface motion along the slope is important over a very short time (the whole rundown process only lasts a small fraction of a second in the experiments). In Figure 14b, an irregularity occured on the computed surface after the time of rundown (curve b). According to visual observation during the experiments, a backward breaking actually occured at this instant as the main crest moved away from the slope (i.e., breaking onto the slope, in the direction opposite to reflected wave propagation). In the computations, the small irregularity propagates away from the wall and, shortly after (b), this wave rapidly breaks backward while still propagating away from the slope, thus terminating the computations. This is the reason why we do not show any computational results corresponding to (c) in Figure 14b. It is in fact fairly evident that at this point we are close to the resolution possible with the number of nodes and the time step used. The rapid development of such small patterns stresses the computations to their limit.

Figure 15a and 15b show the results for a 70° slope. Here an extra profile (curves a) is available in the experiments before the wave reaches the slope. As in the first case, the agreement between physical and numerical experiments is surprisingly good. Notice that even the oscillatory tail left after the main crest has cleared the slope is quite well represented. In the case of the smaller wave (Figure 15a), we have shown curves corresponding to both the measured and the computed times of rundown (curves c and d). In the case of the higher wave, though the various times coincide quite well, the reflected wave is somewhat higher in the experiments (curves c and d). This could be due to the differences in the incident wave, which looks somewhat bulkier in the experiments

(curves a) than the computed wave.

6.3 *The internal velocity field*

The examples in Section 6.2 show that it has been possible to reproduce the surface variations recorded in the experiments down to very small details and over quite extended periods of time relative to the time scale of the important events. This can only be possible if the computational solution actually represents the whole flow pattern to a high degree of accuracy. Thus it will be possible to use the computational solution to analyze other properties of the flow (like the internal velocity field) than those actually measured in the experiments and to have a reasonable confidence in the correctness of such predictions.

We have computed the internal velocity field at 80-90 points (the exact number depending on the water level elevation) in the neighborhood of a 45° slope during runup of a *first-order* wave of $\frac{H}{d}$=0.457. To measure velocities in that detail in the physical experiments would be a tremendous task, whereas it only requires a limited extra effort computationally. Hence this example illustrates the usefulness of combining experiments and numerical computations.

Computation of internal field : The numerical procedure that computes the development of the wave motion in space and time (Sections 2 and 3), leaves us with both ϕ and $\frac{\partial \phi}{\partial n}$known at all time steps. At an internal point $\mathbf{x}_o = (x_o, z_o)$, differenciation of (2) with respect to x_o and z_o yields the velocity components in integral form (see Grilli & Svendsen (1989) for detail). Therefore, the computation of the internal velocity is a theoretically straight-forward evaluation of an integral, as long as the observation point $\mathbf{x}_o$, stays inside the domain. If $\mathbf{x}_o$ is too close to the boundary, however, the integrand varies so rapidly over the one or two elements closest to $\mathbf{x}_o$ that the accuracy is insufficient, even when using ten Gauss-points per element. Therefore the computation points for the internal velocity field have been kept at a distance of about half an element length from the boundary (distance found sufficient for ensuring a good accuracy). This constraint can, of course, be removed by using an adaptive integration for the internal points [4].

Runup : Figure 16a-f shows the velocity field at six different stages of the runup and reflection. Throughout the Figure, the same scale has been used for the velocities, as indicated by the arrow of length $\sqrt{gd}$ shown on part a. When the first part of the wave reaches the slope, the motion

[4] In the computations described here, the number of nodes has been increased up to 232 (of which 137 are on the surface and 19 are on the slope), in order to obtain a better resolution of the internal velocity field close to the slope (see Appendix A for detail). This measure also gives a slight improvement of the integration over the elements closest to the wedge at the tip of the runup.

gradually builds up (Fig. 16a). The combination of the rising water level in the solitary wave and the upward twist of the flow along the slope makes the flow field look almost like the flow in a corner bounding a semi-infinite space. Over the 1.68 time units between part a and b in Figure 16, the picture changes as the wave crest approaches the slope. The upward movement becomes more and more concentrated to the region closest to the shoreline and almost looks like a jet rushing up along the slope. This is even more pronounced in part c where the crest has almost reached the shoreline. Yet, immediately under the crest, which is still a clearly visible maximum of elevation, the velocities are horizontal and large as in a progressive wave. Similarly, behind the crest, the velocities are facing downward and decreasing in size. Part d of Figure 16 shows the instant where the crest of the wave has reached the instantaneous intersection between surface and slope. There is still a jet-like up-rush of the tip of the wave here 0.83 time units later, though more isolated and with smaller velocities than in part c. A stagnation point has developed near the toe of the slope as an indication of the reflection taking effect. In the next 0.90 time units from d to e, this stagnation point moves up along the slope so that more and more of the flow turns direction to downwards along the slope. However, even part e of Figure 16 does not yet represents the instant of maximum runup. That does not occur until at $t'(R_u) = 35.38$ (part f). Clearly, at this and any stage, the flow kinetic energy does not quite reach zero (like observed on a vertical wall in Section 5.4). From this time on, however, the flow is outward going at all points until the lowest point in the down rush is reached. Hence, the tip of the wave is the very last point at which the velocity changes direction.

Rundown : Figure 17a-d similarly shows the velocity field at 4 stages of the flow between the instant of maximum runup and that of the lowest computed position of the surface. A remarkably interesting feature is the combination of high velocities and large accelerations at the time of the lowest position (Fig. 17-d). The steep shoreward slope of the free surface in this non-distorted figure suggests horizontal accelerations close to one g. The rapid retraction of the free surface has another implication, however. Had the slope been porous like a rubble mound structure, it is unlikely the water table inside the structure would have been able to follow the fast drop of the outside water surface. Consequently, onwards from the time of part c in Figure 17, there would be a strong outward directed pressure gradient on the armor units in the structure, caused by the difference in water level inside and outside the slope. This would result in a high risk of units being pulled out of the slope. The damage to rubble mound structures observed during experiments actually often occurs at this stage of the process.

Horizontal velocities : It is rather evident from the outset that, on a steep slope, large horizontal velocities are closely associated with vertical velocities of the same order of magnitude. Therefore, vertical accelerations cannot be neglected, which implies nonhydrostatic pressure which will feed back and create horizontal velocities that are not uniform over depth. The horizontal velocity profiles along verticals can be inferred from Figures 16 and 17. At places and times with high velocities, the relative difference between surface and bottom velocity may be seen to be about 25-30%.

6.4 *Pressure on the slope*

The pressure variation along the slope is shown in Figure 18a and 18b, for the stages of the runup and rundown of Figures 16 and 17. The abscissa is the vertical dimensionless coordinate along the slope. The ordinate $\frac{p_T}{p_H}$ is given by,

$$\frac{p_T}{p_H} = \frac{-\rho(\frac{\partial \phi}{\partial t} + \frac{1}{2}\mid \nabla\phi \mid^2 + gz)}{\rho g \zeta} \tag{25}$$

where p_T is the total pressure computed from the Bernoulli equation and ζ is the vertical distance between the free surface and the point on the slope. Hence, the ordinate $+1$ corresponds to the actual pressure being equal to the weight of the water column above the point ("hydrostatic pressure" p_H).

While the pressure in the runup phase (Fig. 18a) differs somewhat from the hydrostatic, it generally stays within 1.1 and 0.7 times that value, the lowest values occuring near the surface at the time of runup (part f). Figure 18b shows the pressure during rundown. Initially, the pattern at the time of runup essentially propagates down the slope. This might be expected because at that point, the tip of the runup is rather isolated from the rest of the water body and just moving under the action of gravity so that the pressure reflects the gravity component $\frac{g}{\sqrt{2}} \simeq 0.7g$ normal to the surface (curve a and next in Figure 18b). When the surface slope changes sign (Figure 17b-c), the flow in the down-rush starts decelerating, which creates pressures above hydrostatic, as seen from curves b and c. This is even more pronounced in curve d where the pressure is above hydrostatic all along the slope.

6.5 *Comparison with the shallow water wave equations*

One of the questions that can be asked when looking at these results for highly nonlinear wave runup is: How well will the nonlinear shallow water (NSW) equations be able to describe this flow.

Synolakis (1987) (SY) extended the Carrier & Greenspan (1958) solution for the Nonlinear

Shallow Water (NSW) equations on an infinite slope, to the case of a slope facing a region of finite constant depth d, and a (*first-order*) solitary incident wave. He gave two different expressions for the runup height $\frac{R_u}{d}$ on the slope : one an explicit approximate formula only valid for gentle slopes, the other an integral equation. A comparison of his runup values with the BEM results has been reported by Svendsen & Grilli (1990) (S&G) who found acceptable agreement with the BEM computations, particularly for the integral equation, even for slopes as steep as 70°.

However, the relevance of using the NSW equations on so steep slopes is questionable. S&G find that the basic assumptions behind the NSW equations, of negligible vertical accelerations and, consequently, uniform horizontal velocities and hydrostatic pressures, are severely invalidated already on a slope of 30°. This is further confirmed by the results obtained above for a 45° slope (Sections 6.3 and 6.4).

7 Conclusions

The computations described here have been made in the physical space with a Boundary Integral Equation Method which allows for waves that are non periodic in space. It turns out that sawtooth instability does not occur, and that both energy and volume inside the computational region are controled sufficiently well to not making it necessary to carry out artificial adjustments during the computations.

Solitary waves have been generated by two independent methods. *Exact* solitary waves by Tanaka's (1986) method and *first-order* waves by a piston wavemaker using Goring's (1978) approach. Both wave types are used for examining the runup and reflection from a vertical wall and the *first-order* waves reproduce as closely as possible the conditions in the experiments by Losada, *et al.* (1986) (LVN).

The BEM computations have been compared with a 3rd-order analytic solution by Su & Mirie (1980) (S&M) and a Fourier solution by Fenton & Rienecker (1982) (F&R) for the reflection from a vertical wall. The results show that up to $\frac{H}{d}$=0.4, all three methods give similar predictions for the runup and for the pressure force on the wall (with slightly lower results for the *first-order* waves, because of the energy transmitted to their oscillatory tail). For higher waves, higher order contributions are becoming important and our results predict somewhat larger runup and force than did the previous investigations. For large values of $\frac{H}{d}$it is also found that the variation of the pressure force on the wall with respect to time exhibits double maxima. *First-order* wave runup and rundown values agree well with LVN's experiments (within 5%).

Results for the rundown, reflected wave, celerity, phase shift and energy partition of an *exact*

solitary wave of incident height $\frac{H}{d}$=0.5 have been compared with a 5th-order analytic solution by Byatt-Smith (1988) (B-S). Most of the findings of the latter study are quite well reproduced quantitatively. An oscillatory tail is created by the reflection process and, due to the energy transmitted to the tail, the wave amplitude decreases slightly after reflection (9.3%). Rundown values (negative elevations) of the same order are observed at the wall. The celerity of the (transient) reflected wave is found to be slightly more (0.5%) than for the incident wave, as also computed by F&R (who , however, got a much larger increase of 6.6%, and also did not obtain an oscillatory tail after reflection) and observed experimentally by Seabra-Santos (1985). Instantaneous time and space phase lags during the reflection process are also found somewhat smaller than predicted by S&M and F&R. Although the amplitude of the reflected wave recovers partly, it will not return to its initial value because of the energy transfered to the tail (against B-S statement) and, accordingly, the celerity of the reflected wave will eventually become slightly smaller, as it approaches permanent form. The kinetic energy is found to be minimum (but not quite zero) slightly before the time of the runup. Kinetic energy also drops after reflection (0.54%), with respect to its initial value, and only part of this decrease is recovered on a longer term basis.

Reflection from steep slopes (45° and 70°) has also been examined for solitary waves generated by a piston wavemaker, as in LVN's experiments. Comparison with the measurements shows that generation, propagation and runup on a steep slope of large amplitude waves are accurately predicted by this method. Even small scale oscillations in the experiments (like the oscillatory tail after reflection) are well reproduced. Motivated by the accuracy of the computations the method has been used to analyze flow properties such as velocity and pressure fields that have not been measured during the experiments. Computation of the water particle velocities above a 45° slope during runup-rundown shows that horizontal velocities are significantly non-uniform over the depth (variation of 25-30%) and that, accordingly, important non-hydrostatic pressures (variations of -38% to 75%) are generated. This invalidates the assumptions underlying the Nonlinear Shallow Water equations and makes their use questionable in these situations. Similar conclusions were already reached by Svendsen & Grilli (1990), for a 30° slope. The maximum runup, however, is found to compare reasonably well with the results obtained by Synolakis (1987) using those approximate equations.

$\frac{H}{d}$	$\Delta x'$	L'	$\Delta t'$	$10^4\Delta^T m$	$10^4\Delta^T e_t$	$10^4\Delta^o m$	$10^4\Delta^o e_t$
0.20	0.45	37.80	0.09-0.450	1.29	0.49	7.9	6.3
0.30	0.40	33.60	0.07-0.035	2.03	0.54	9.0	4.2
0.40	0.33	28.67	0.06-0.030	3.03	1.75	13.8	10.1
0.50	0.25	28.00	0.05-0.025	3.62	2.21	4.8	10.9
0.55	0.25	28.00	0.04-0.010	2.97	4.75	8.0	8.6
0.60	0.25	28.00	0.04-0.010	3.58	6.88	6.9	10.2

Table 7: Reflection on a vertical wall of *exact* solitary waves : wave height $\frac{H}{d}$, discretization step $\Delta x'$, tank length $L' = \frac{L}{d}$, and time step $\Delta t'$ (over constant depth – during reflection at the wall), differences between computed and exact (Tanaka (1986)) values of mass and total energy at the first time step $\Delta^T m$ and $\Delta^T e_t$ and absolute maximum mass and energy errors over the BEM computations (relative to first time step values) $\Delta^o m$ and $\Delta^o e_t$.

A Appendix. Numerical data and checks of accuracy for the exact waves

Reflection of *exact* solitary waves from a vertical wall has been computed. Waves are generated with $\varepsilon_z = 5.10^{-6}$ to 10^{-5}, at the mid-point of a tank of length L=28d to 37.8d, whose free surface is discretized by 85 to 113 equally spaced nodes (step $\Delta x'$ as in Table 7). The discretization step is twice larger on the bottom than on the free surface. Hence, the total number of nodes of the BEM discretizations varies between 184 and 242, and the total number of elements, between 140 and 184. Time steps $\Delta t'$ vary between 0.04 and 0.09 for the propagation over constant depth ($\frac{\Delta t'}{\Delta x'}$=0.16 to 0.20), and between 0.01 and 0.045 ($\frac{\Delta t'}{\Delta x'}$=0.04 to 0.10) during reflection on the wall (Table 7). Computation times vary between 1.44s to 2.34s CPU per time step (IBM-3090/300), of which 2 to 9% are used for data postprocessing.

Discretization effects create small initial adjustments of mass and energy (Δ^T's in Table 7) with respect to Tanaka's (1986) results (Table 1). The overall accuracy of the computations is checked by calculating maximum absolute errors in energy $\Delta^o e_t$ and mass $\Delta^o m$, relative to values at the first time step. Results in Table 7 show that maximum errors are always less than 0.1%.

A more detailed analysis of the results, however, shows that the errors are generally much less during propagation of the wave ($\sim$ 0.01%), and that the higher variations are observed during the reflection at the slope. After reflection, both total energy and mass get back to their initial values, within a few hundredths of a percent. Comparing the instantaneous errors for e_t and m, it is apparent that the change in total energy during the runup-rundown of the wave is quite well

matched by a similar change in volume. This suggests that, although a reduction of the time step is made in the computations (Table 7), the fixed $\Delta t'$ may be too large to account for the rapid changes in surface position during the short interval of the process where the surface is moving really fast up and down along the slope.

Aknowledgments

The authors greatfully acknowledge the assitance from M.A. Losada in extracting the experimental results from the original data. The authors would also like to thank D.H. Peregrine and M. Cooker for having provided them with software which generates exact solitary wave profiles according to Tanaka (1986), and C.E. Synolakis for helpful comments and numerical results.

REFERENCES

BREBBIA, C.A. 1978 *The Boundary Element Method for Engineers.* John Wiley & Sons, U.K..

BYATT-SMITH, J.G.B. 1988 The Reflection of a Solitary Wave by a Vertical Wall. *J. Fluid Mech.* **197,** 503-521.

CAMFIELD, F.E. & STREET, R.L. 1969 Shoaling of Solitary Waves on Small Slopes. *J. Waterways and Harbor Div.* **95** (WW1), 1-22.

CARRIER, G.F. 1966 Gravity Waves on Water of Variable Depth. *J. Fluid Mech.* **24** (4), 641-659.

CARRIER, G.F. & GREENSPAN, H.P. 1958 Water Waves of Finite Amplitude on a Sloping Beach. *J. Fluid Mech.* **4** (1), 97-110.

COOKER, M. 1989 Personal communication.

DEMIDOVITCH, B. & MARION, I. 1979 *Eléments de calcul numérique.* Edition Mir. Moscou.

DOLD, J.W. & PEREGRINE, D.H. 1986 An Efficient Boundary Integral Method for Steep Unsteady water Waves. *Numerical methods for Fluid Dynamics II* (ed. K.W. Morton & M.J. Baines), pp. 671-679. Clarendon Press, Oxford.

DOMMERMUTH, D.G. & YUE, D.K.P. 1987 Numerical Simulation of Nonlinear Axisymmetric Flows with a Free Surface. *J. Fluid Mech.* **178,** 195-219.

FENTON, J.D. & RIENECKER, M.M. 1982 A Fourier Method for Solving Nonlinear Water-Wave Problems : Application to Solitary-Wave Interactions. *J. Fluid Mech.* **118,** 411-443.

GARDNER, C.S., GREENE, J.M., KRUSKAL, M.D. & MIURA, R.M. 1967 Method for Solving the Korteweg-de Vries Equation. *Physical Revue Letters* **19,** (19), 1095-1097.

GORING D.G. 1978 Tsunamis - The Propagation of Long Waves onto a Shelf. *W.M. Keck Laboratory of Hydraulics and Water Ressources, California Institute of Technology, Report No.* **KH-R-38.**

GREENHOW, M. & LIN, W.M. 1985 Numerical Simulation of Nonlinear Free Surface Flows Generated by Wedge Entry and Wave-maker Motions. In *Proc. 4th Intl. Conf. on Num. Ship Hydro., Washington D.C., September 1985.*

GRILLI, S., SKOURUP, J. & SVENDSEN, I.A. 1988 The Modelling of Highly Nonlinear Waves : A Step Toward the Numerical Wave Tank. Invited paper in *Proc. 10th Intl. Conf. on Boundary Elements, Southampton, England, September 1988,* Vol. 1 (ed. C.A. Brebbia), pp. 549-564. Computational Mechan-

ics Publication. Springer-Verlag, Berlin.

GRILLI, S., SKOURUP, J. & SVENDSEN, I.A. 1989 An Efficient Boundary Element Method for Nonlinear Water Waves. *Engineering Analysis with Boundary Elements,* **6** (2), 97-107.

GRILLI, S. & SVENDSEN, I.A. 1989 Computation of Nonlinear Wave Kinematics during Propagation and Runup on a Slope. In *Water Wave Kinematics* (Proc. NATO ARW, Molde, Norway, May 89) (ed. A. Torum & O.T. Gudmestad), NATO ASI Series E: Applied Sciences Vol. **178,** 387-412. Klüwer Academic Publishers.

GRILLI, S. & SVENDSEN, I.A. 1990 Corner Problems and Global Accuracy in the Boundary Element Solution of Nonlinear Wave Flows. *Engineering Analysis with Boundary Elements* **7** (4) (in press).

HAMMACK, J.L. & SEGUR, H. 1974 The Korteweg-de Vries Equation and Water Waves. Part 2. Comparison with Experiments. *J. Fluid Mech.* **65** (2), 289-314.

ISAACSON, M. de St. Q. 1982 Nonlinear Effects on Fixed and Floating Bodies. *J. Fluid Mech.* **120,** 267-281.

KIM, S.K., LIU, P.L.-F. & LIGGETT, J.A. 1983 Boundary integral Equation Solutions for Solitary Wave Generation Propagation and Run-up. *Coastal Engineering* **7,** 299-317.

KLOPMAN, G. 1988 Numerical Simulation of Gravity Wave Motion on Steep slopes. *Delft Hydraulics Report No.* **H195.**

LONGUET-HIGGINS, M.S. & COKELET, E.D. 1976 The Deformation of Steep Surface Waves on Water - I. A Numerical Method of Computation. *Proc. R. Soc. Lond.* **A350,** 1-26.

LOSADA, M.A., VIDAL, C. & NUNEZ, J. 1986 Sobre El Comportamiento de Ondas Propagádose por Perfiles de Playa en Barra y Diques Sumergidos. *Dirección General de Puertos y Costas Programa de Clima Maritimo. Universidad de Cantábria. Publicación No.* **16.**

MAXWORTHY, T. 1976 Experiments on Collisions Between Solitary Waves. *J. Fluid Mech.* **76** (1), 177-185.

MIRIE R.M. & SU C.H. 1982 Collisions Between Two Solitary Waves. Part 2. A Numerical Study. *J. Fluid Mech.* **115,** 475-492.

NAGAI, S. 1969 Pressures of Standing Waves on Vertical Wall. *J. Waterways and Harbor Div.* **95** (WW1), 53-76.

NAKAYAMA, T. 1983 Boundary Element Analysis of Nonlinear Water Wave Problems. *Intl. J. Numer. Meth. Engng.* **19,** 953-970.

NAM SEO, S. 1988 Time-Dependent Highly Nonlinear Waves (Ph.D. Dissertation). *Civil Engineering Department, University of Delaware, U.S.A.* .

OIKAWA, M. & YAJIMA, N. 1973 Interaction of Solitary Waves - A Perturbation Approach to Nonlinear Systems. *J. Phys. Soc. Japan* **34,** 1093-1099.

PACKWOOD, A.R. & PEREGRINE, D.H. 1981 Surf and Runup on Beaches : Models of Viscous Effects. *School of Mathematics, University of Bristol, Report No.* **AM-81-07.**

PEDERSEN, G. & GJEVIK, B. 1983 Run-up of Solitary Waves *J. Fluid Mech.* **135,** 283-299.

PHILLIPS, O.M. 1977 *The Dynamics of the Upper Ocean.* Cambridge University Press, U.K..

ROMATE, J.E. 1989 The Numerical Simulation of Nonlinear Gravity Waves in Three Dimensions using a Higher Order Panel Method. *Ph.D. Dissertation. Department of Applied Mathematics, University of Twente, The Netherland.*

SEABRA-SANTOS, F.J. 1985 Contribution à l'étude des ondes de gravité bidimensionnelles en eau peu profonde (Thèse de Doctorat d'Etat). *Université scientifique et Médicale et Institut Polytechnique de Grenoble.*

SU, C.H. & MIRIE, R.M. 1980 On Head-on Collisions between two Solitary Waves. *J. Fluid Mech.* **98** 509-525.

SU, C.H. & GARDNER, C.S. 1969 Korteweg-de Vries Equation and Generalizations. III. Derivation of the Korteweg-de Vries Equation and Burgers Equation. *J. Math. Phys.* **10** 536-539.

SUGIMOTO, N., KUSAKA, Y. & KAKUTANI, T. 1987 Reflection of a Shallow-water Soliton. Part 2. Numerical Evaluation. *J. Fluid Mech.* **178,** 99-117.

SVENDSEN, I.A. 1971 Mixed Boundary Value Problem for Laplace's Equation in Domain of Arbitrary Shape. *Technical University of Denmark report No.* **23,** 33-38.

SVENDSEN, I.A. & GRILLI, S. 1990 Nonlinear Waves on Steep Slopes. *J. Coastal Research* **SI 7,** 185-202.

SVENDSEN, I.A. & JUSTESEN, P. 1984 Forces on Slender Cylinders from Very High and Spilling Breakers. In *Proc. Symp. on Description and Modelling of Directional Seas,* paper No. D-7, 16 pps. Technical University of Denmark.

SYNOLAKIS, C.E. 1987 The Runup of Solitary Waves. *J. Fluid Mech.* **185,** 523-545.

SYNOLAKIS, C.E. 1990 Generation of Long Waves in Laboratory. *J. Waterways, Harbors and Coastal Engng.* **116** (2), 252-267.

TANAKA, M. 1986 The Stability of Solitary Waves. *Phys. Fluids* **29** (3), 650-655.

VINJE, T. & BREVIG, P. 1981 Numerical Simulation of Breaking Waves. *Adv. Water Resources* **4,** 77-82.

List of Figure captions

Fig. 1: Sketch of the region used in the numerical computations in Section 5 and 6. Definition of geometrical parameters.

Fig. 2: Surface profile $\eta(x)$ for *first-order* solitary waves of height $\frac{H_i}{d} = 0.2$ through 0.5. Each wave is shown at the moment the crest passes $x' = 20$ (20 water depth d from the wave generator). The propagation times t' are : $\frac{H_i}{d} = 0.2 : 27.27, 0.3 : 24.64, 0.4 : 22.92, 0.5 : 21.65$.

Fig. 3a: Comparison between two *first-order* solitary wave surface profiles generated at $x' = 66.7$ (- - -) and $x' = 0$ (——) respectively (i.e. after propagating $20d$ and $86.7d$). To be of the same height $\frac{H_i}{d} = 0.25$ at $x' = 86.7$, the two waves were generated with slightly different amplitude.

Fig. 3b: Comparison between the second wave of Fig. 3a (——) and an *exact* solitary wave of same height (- - -), at the same position $x' = 86.7$.

Fig. 4: Development of crest elevation for the two *first-order* waves compared in Fig. 3a.

Fig. 5: Variation of maximum amplitude $\frac{H}{d}$during reflection from a vertical wall of the two *first-order* waves shown in Fig. 3a and 4 (solid and dotted lines defined as in Fig. 3a). The wall is at $x' = 100$ and the vertical line A-B shows the height of the runup. The lowest of the two sets of curves represents the crest elevations after runup (starting at A' on the wall).

Fig. 6: Maximum runup $\frac{R_u}{d}$ for reflection from a vertical wall versus the value of the incident wave height $\frac{H}{d}$(the incident *first-order* wave amplitude is defined at $x' = 20$ $(13.3d)$ in front of the wall as in Fig. 2). (——) Su & Mirie (1980) 3rd-order analytical results, (□) Fenton & Rienecker (1982) Fourier Method results, (o) present BEM results for the *first-order* waves, (◇) present BEM results for the *exact* waves, (- - -) cubic spline fitting to these last results and (– - –) linear relationship $\frac{R_u}{d} = 2\frac{H}{d}$.

Fig. 7: Lowest point of water surface $\frac{R_d}{d}$ (rundown) for reflection from a vertical wall versus the

incident wave height $\frac{H}{d}$defined as in Fig. 6. (o) Present BEM results for the *first-order* waves and (——) cubic spline fitting to the results; ($\diamond$) present BEM results for the *exact* waves and (- - -) cubic spline fitting to the results. Notice that all elevations are negative, and the scale is very different from that in Fig. 6.

Fig. 8: Reflected wave profiles of *exact* solitary waves from a vertical wall. Incident wave height $\frac{H}{d}$= (a) : 0.2, (b) : 0.3, (c) : 0.4, (d) : 0.5. Notice the increasingly more developed oscillatory tail from (a) to (d). Corresponding times are t' = (a) : 32.31, (b) : 27.58, (c) : 26.40, (d) : 29.98.

Fig. 9a: (——) Reflected wave (at t' = 23.53 or $\tau_2 \simeq 3$) for an incident *exact* solitary wave of $\frac{H}{d}$=0.5, compared with the incident wave (- - -) at the same location x'_o=14.

Fig. 9b: (——) Maximum amplitude $\frac{H}{d}$of the reflected wave of Fig. 9a, as a function of time t' (shown from time t'_2=13.58 where it leaves the wall), compared with the 5th-order analytic solution by Byatt-Smith (1988) (- - -). The time of rundown $t'(R_d)$=16.18 is also marked on the Figure. Locations x' of the maximum amplitude corresponding to times t', are plotted in Fig. 10.

Fig. 9c: (——) Deviation of the reflected wave η' of Fig. 9a from the incident wave $\eta'_o = \eta'(x', t'_o)$ (oscillatory tail), compared with the 5th-order analytic solution of Byatt-Smith (1988) (- - -).

Fig. 10a: (——) Phase diagram for the same wave as in Fig. 9, i.e., (x', t') plot for the point of maximum amplitude on the free surface. Notice the reflection occurs at x' = 28 (vertical wall location) and the maximum runup is at $t'(R_u)$ = 12.05. (- - -) are straight lines fitted (LSM) to the data for $x' < 20$ whose slope $\frac{dx'}{dt'}$ gives the average incident and reflected wave celerities : $\overline{c'_i}$ = 1.2168 and $\overline{c'_r}$ = 1.2226.

Fig. 10b: Closer view on Fig. 10a, with temporal phase lag $\Delta t'$ = 0.627 (B-C) and spatial phase lag $\Delta x'$ = 0.763 (E-C). Notice B-F is a line symmetric to $\overline{c'_i}$.

Fig. 11a: Change in kinetic energy e_k and in potential energy e_p during reflection from a vertical wall, for the same wave as in Fig. 8-10. Notice the kinetic energy never quite reaches zero (e_k^{min}=0.00259, or 0.786% e_{ko}), and the minimum occurs slightly before the instant of maximum runup ($\Delta^{Ru}t'$=0.200). The initial kinetic energy is e_{ko}=0.329923 and the initial potential energy is e_{po}=0.285567.

Fig. 11b: Closer view on Fig. 11a. The decrease in kinetic energy after rundown Δe_k at $t'(R_d)$ is calculated at A, equal to 0.00179 (0.543% e_{ko}). This eventually reduces down to 0.384% e_{ko} at t'=29.98.

Fig. 12: (a) Maximum dimensionless pressure force F_x^{max} and (b) moment with respect to the bottom M_b^{max}, for the same results as in Fig. 5.

Fig. 13a: Development in time of total dimensionless pressure force F_x on a vertical wall during reflection of an *exact* solitary wave. $\frac{H}{d}$ = (a) : 0.2, (b) : 0.3, (c) : 0.4, (d) : 0.5, (e) : 0.55, (f) : 0.6. Notice the double maximum for $\frac{H}{d}$greater than 0.4.

Fig. 13b: Surface elevation at the wall η', pressure force F_x and moment M_b as a function of time for the same wave as in Fig. 9-11.

Fig. 14a: Comparison between computations (——) and measurements (- - -) by Losada, *et al.* (1986) for reflection from a 45° slope, $\frac{H_i}{d}$= 0.269. The symbols mark data points that have been developed from the original experimental records, and the dotted curve is a spline fit to these points.

(a) Instant of maximum runup (t' = 38.44 in computations)

(b) t' = 41.76

(c) Instant of lowest position of water surface ($t' = 42.20$, computations and experiments)
(d) $t' = 51.92$ (computations and experiments)
Fig. 14b: Same definitions as Fig. 14a : 45° slope, $\frac{H_i}{d}$= 0.457.
(a) Instant of maximum runup ($t' = 35.38$ in computations)
(b) Instant of last computed position of the water surface ($t' = 37.93$)(backward breaking occured after that time)
(c) Instant of lowest position of water surface in experiments ($t' = 38.90$) (backward breaking was observed around that time)
(d) $t' = 52.50$
Fig. 15a: Same definitions as Fig. 14a : 70° slope, $\frac{H_i}{d}$= 0.259.
(a) Wave profile somewhat before maximum runup ($t' = 31.60$, computations and experiments)
(b) Instant of maximum runup ($t' = 38.20$ in computations)
(c) Instant of lowest position of water surface in computations ($t' = 42.56$)
(d) Instant of lowest position of water surface in the experiments ($t' = 42.83$)
(e) Reflected wave $\frac{H_r}{d} = 0.244$ at $x' = 20$ ($t' = 50.00$ in the computations, $t' = 49.85$ in the experiments).
Fig. 15b: Same definitions as Fig. 14a : 70° slope, $\frac{H_i}{d}$= 0.437.
(a) Wave profile somewhat before maximum runup ($t' = 27.90$, computations and experiments)
(b) Instant of maximum runup ($t' = 34.58$ in computations)
(c) Instant of lowest position of water surface ($t' = 38.10$, computations and experiments)
(d) Reflected wave $\frac{H_r}{d} = 0.376$ at $x' = 20$ ($t' = 45.50$ in the computations, $t' = 45.24$ in the experiments).
Fig. 16a-f: The internal velocity field during runup of a *first-order* solitary wave with $\frac{H_i}{d}$= 0.457 on a 45° slope, at time t' = (a) : 30.38, (b) : 32.05, (c) : 33.15, (d) : 33.98, (e) : 34.88, (f) : 35.38. The bar in Fig 16a indicates length of arrow representing a velocity of $\sqrt{gd}$. Details of the figures are discussed in the text.
Fig. 17a-f: Same as Fig. 16 but for the rundown phase, at time t' = (a) : 36.13, (b) : 37.25, (c) : 37.79, (d) : 37.93.
Fig. 18a: Pressure distribution along the slope during runup of the same wave and for the same times (curves (a) to (f)) as in Fig. 16. The total pressure p_T is made dimensionless by division by the hydrostatic pressure p_H of the instantaneous water surface vertically above the considered point.
Fig. 18b: Same as Fig. 18a but for the rundown phase (as in Fig. 17 plus one extra curve between (a) and (b) at $t' = 36.73$).

Figure 1

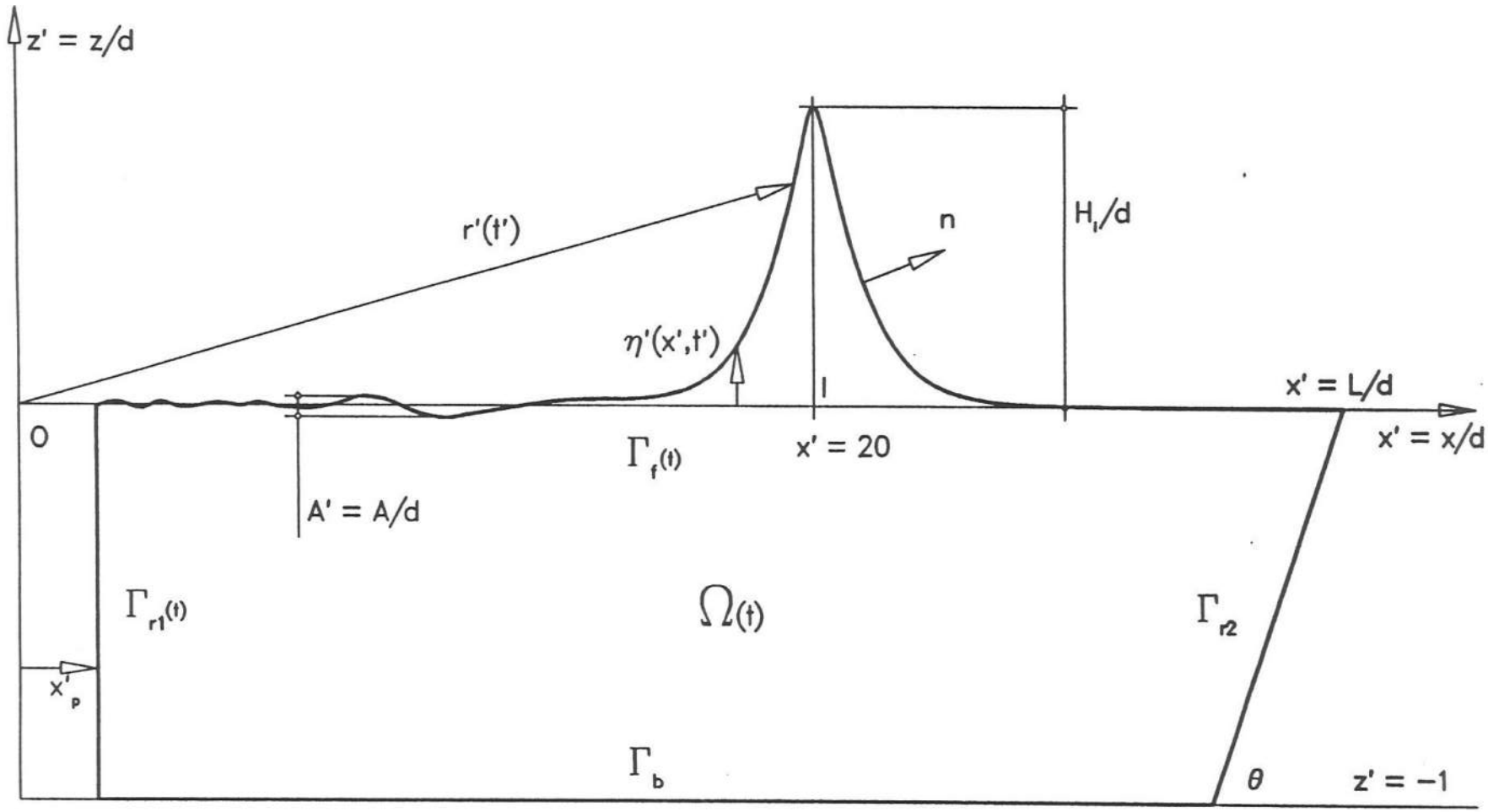

Fig. 2 1st Order Solitary Wave Generation

Incident Wave, Hi/d = 0.2 to 0.5

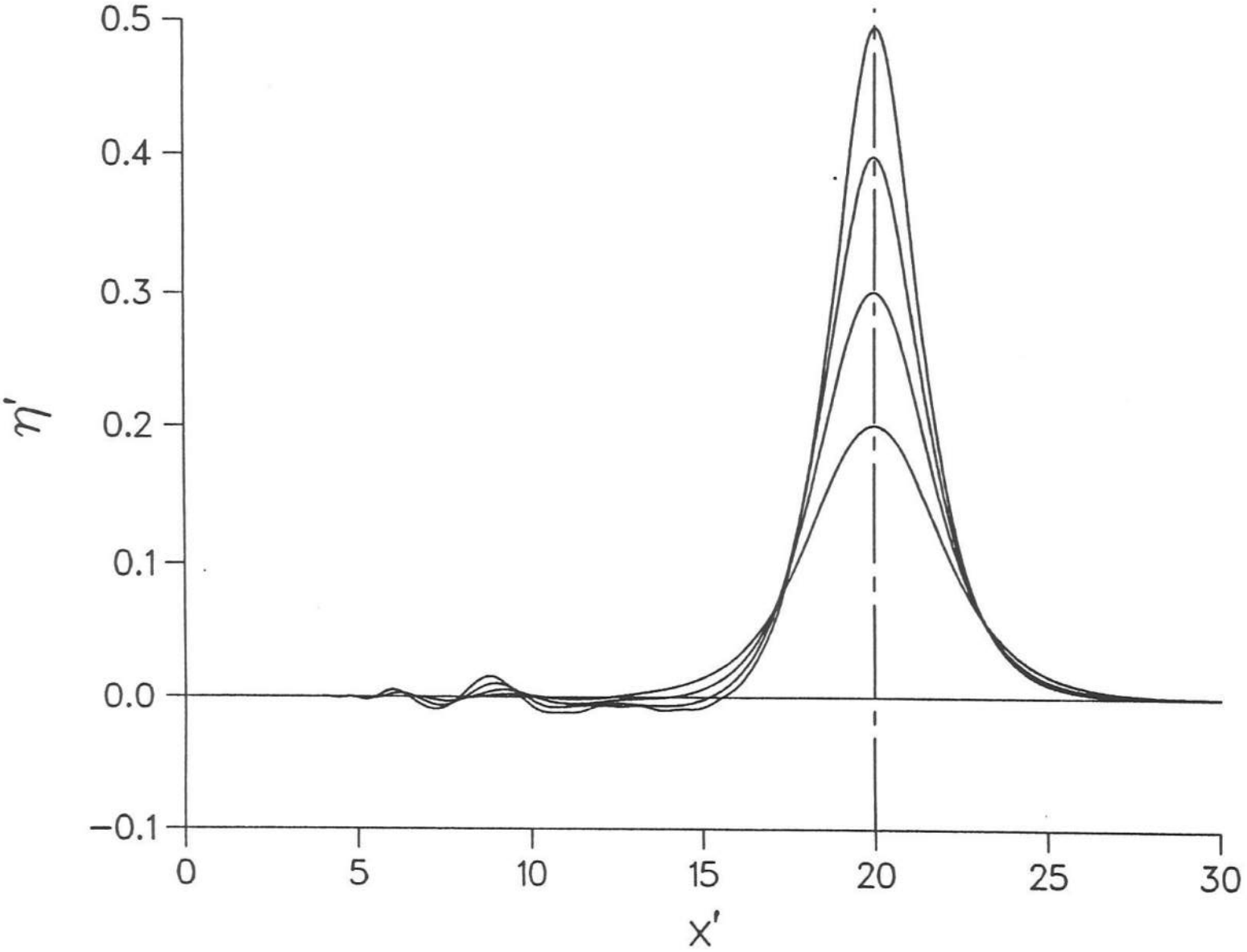

Fig. 3a: 1st Order Solitary Wave Generation

Comparison Of Wave Elevation For H/d=0.25 at x'=86.7

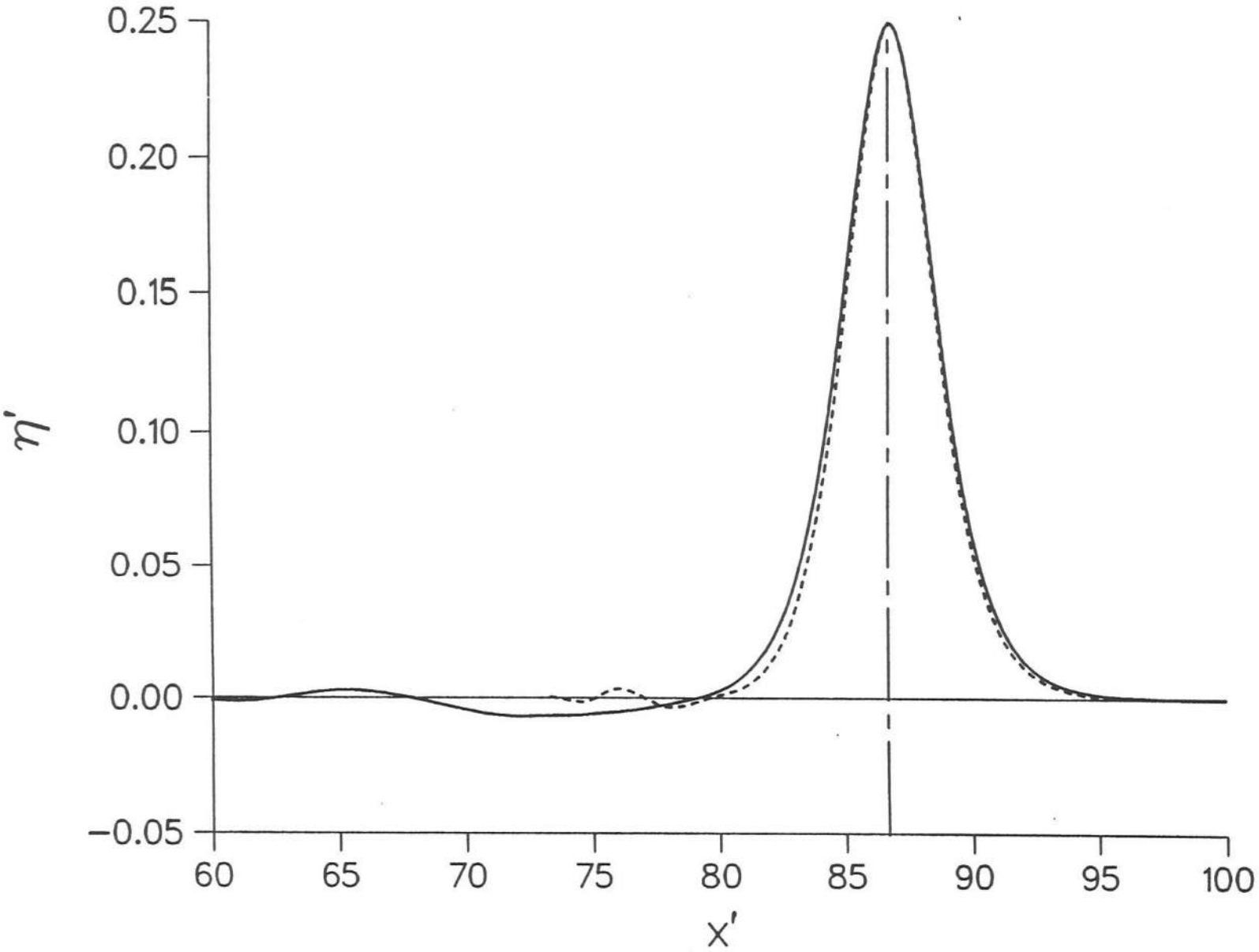

Fig. 3b: 1st Order Solitary Wave Generation

Comparison With an exact wave : H/d=0.25 at x'=86.7

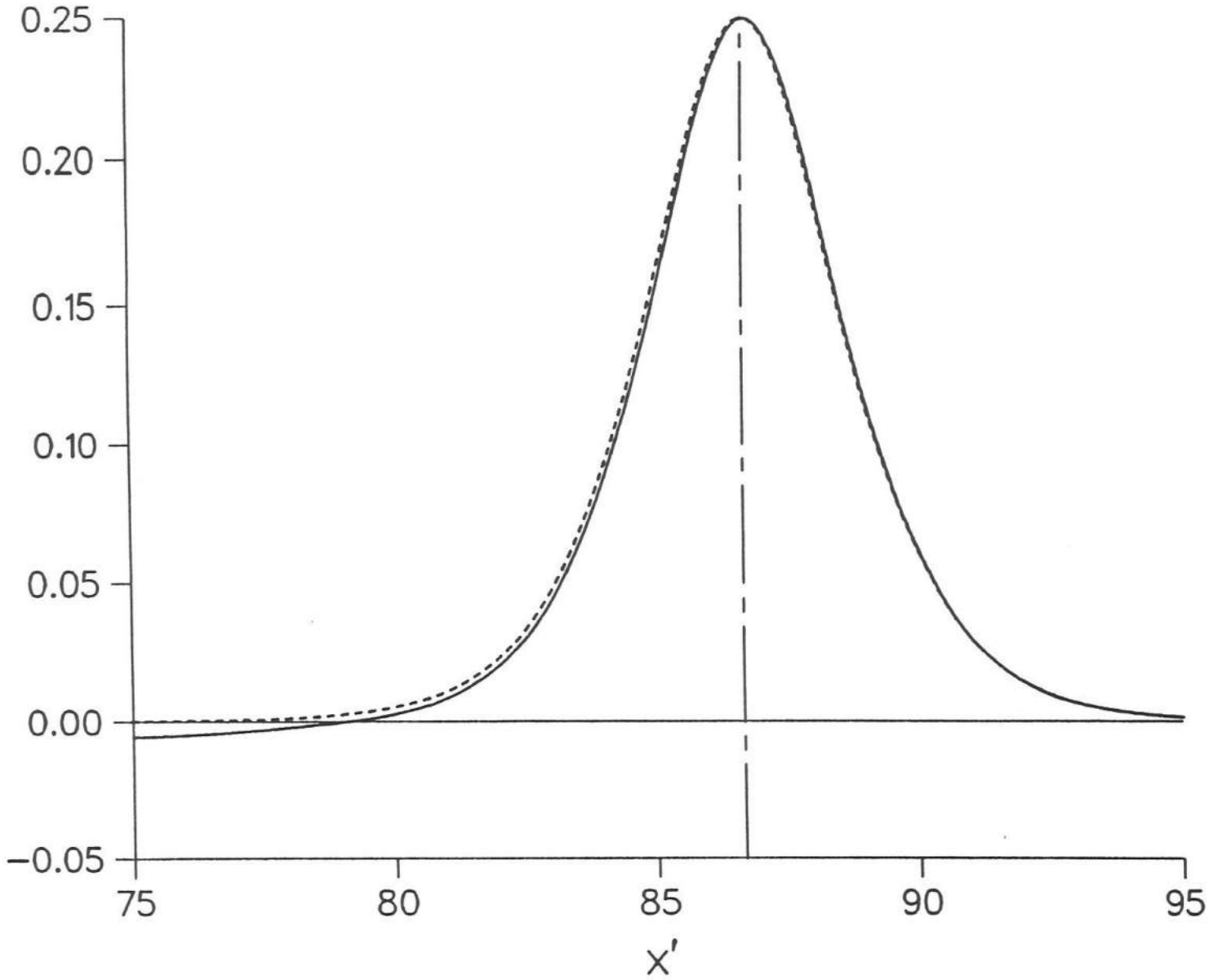

Fig 4: 1st Order Solitary Wave Generation

Amplitude Decrease : Hi/d = 0.25

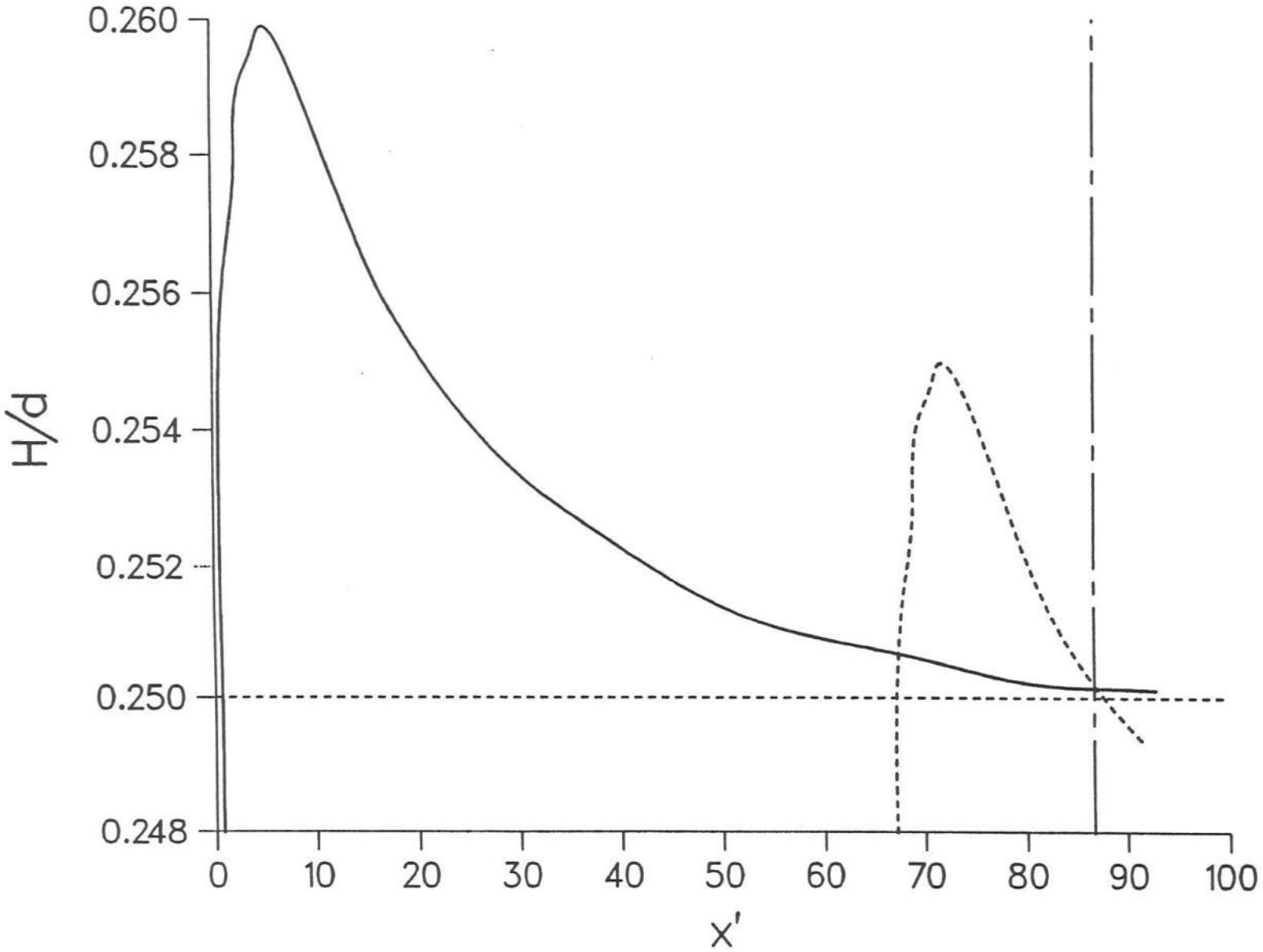

Fig. 5 : 1st Order Solitary Waves Generation

Reflection On A Vertical Wall For Hi/d=0.25

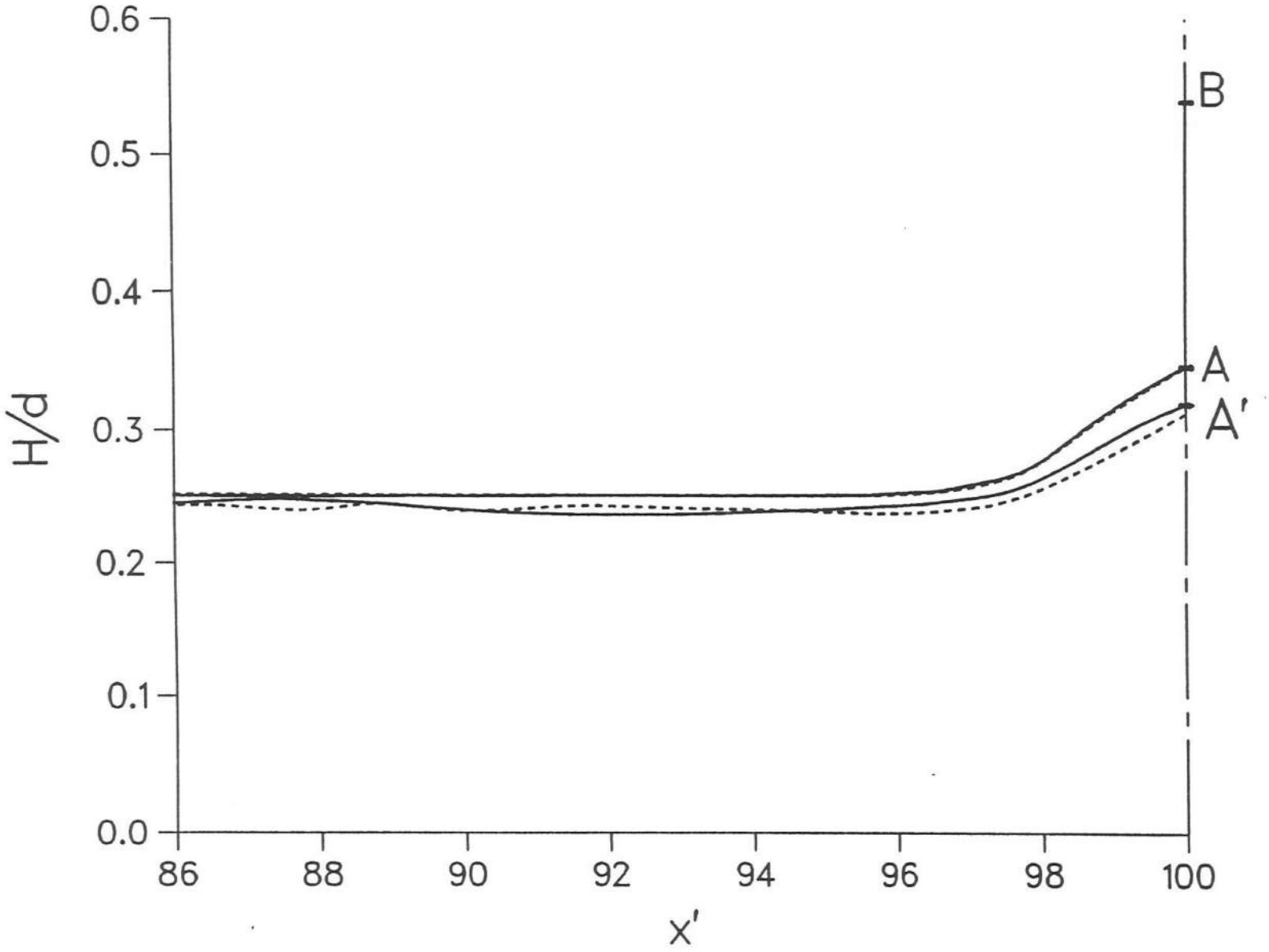

Fig. 6: Reflection On a Vertical Wall

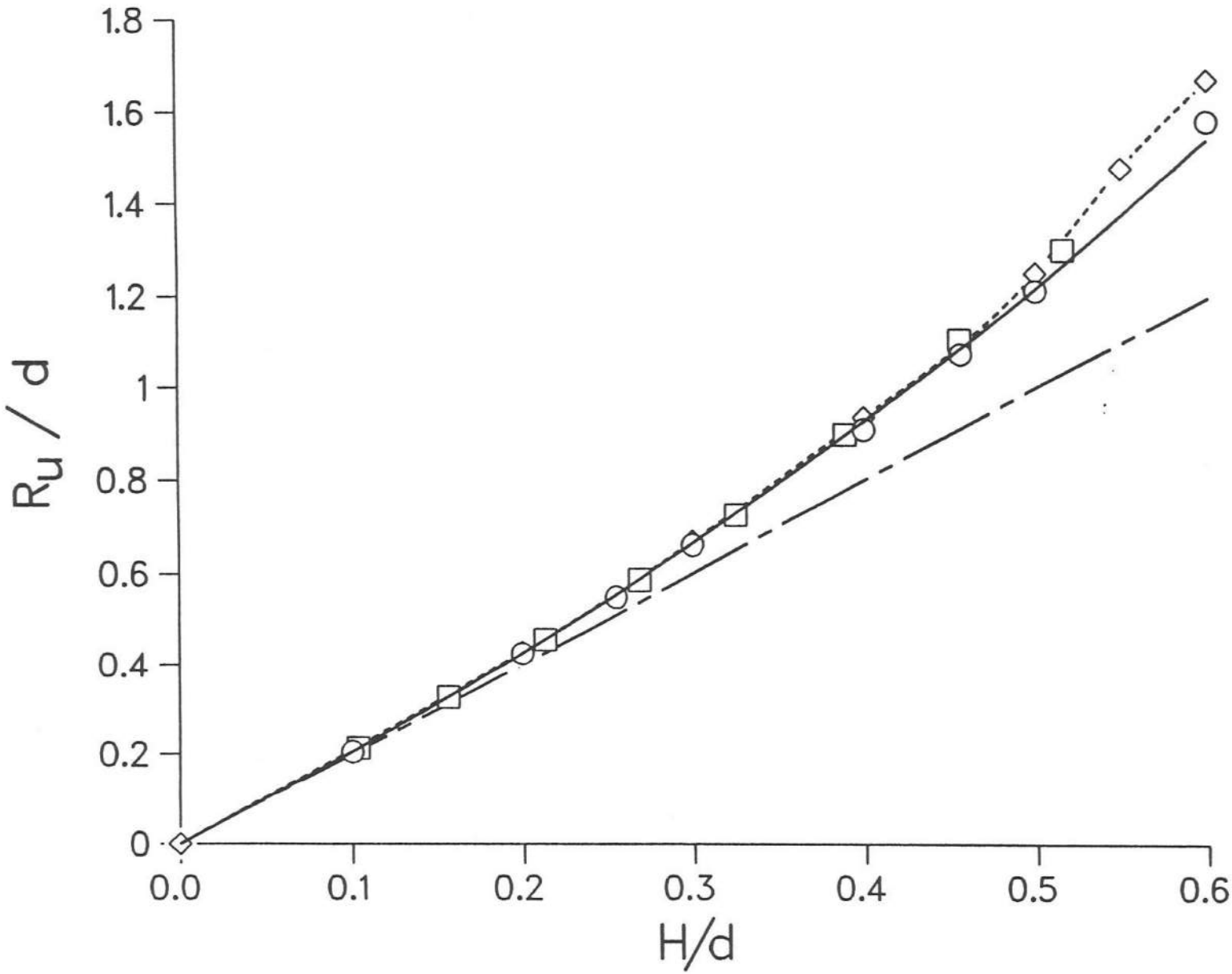

Fig. 7 Reflection On a Vertical Wall

Maximum Rundown

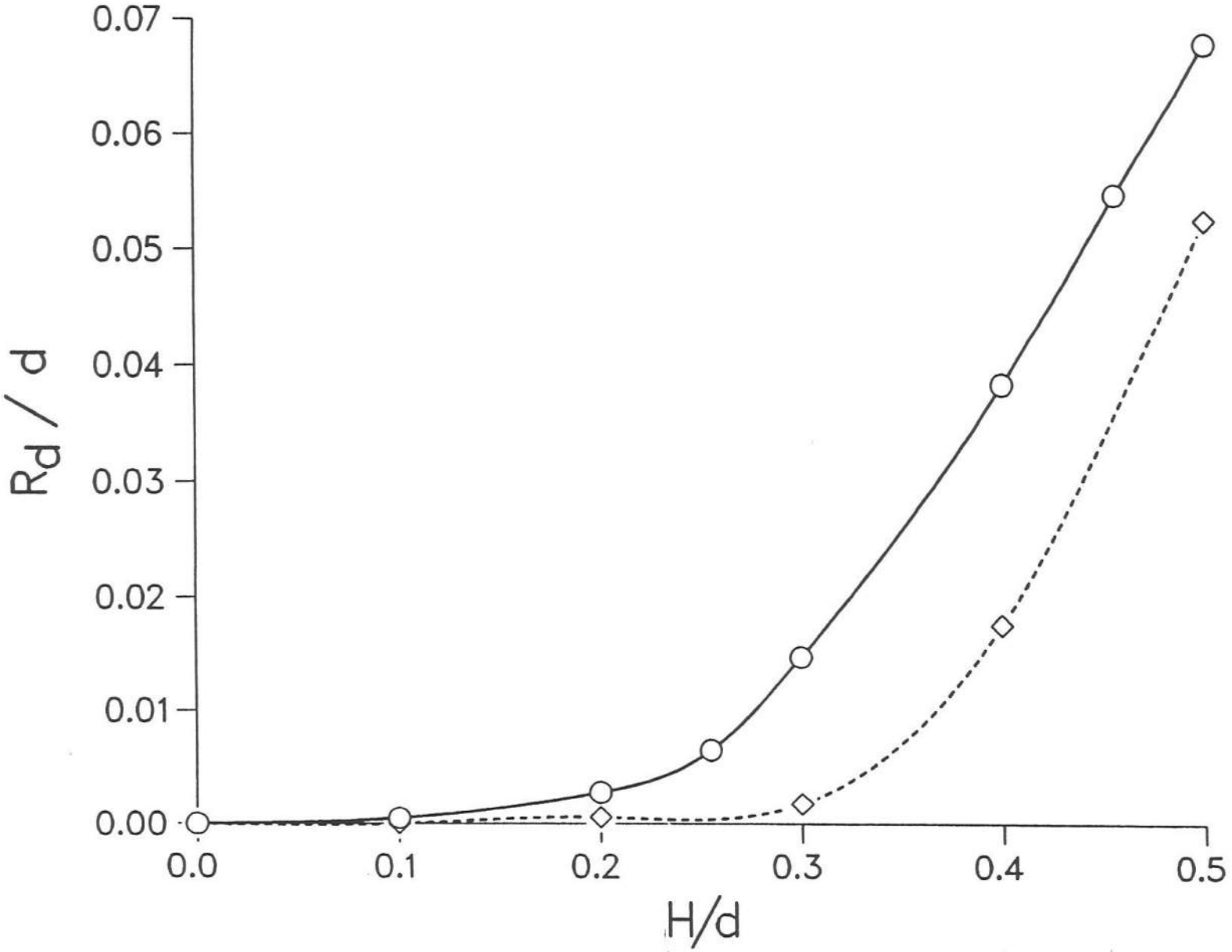

Fig. 8 : Reflection On A Vertical Wall

Reflected Exact Waves

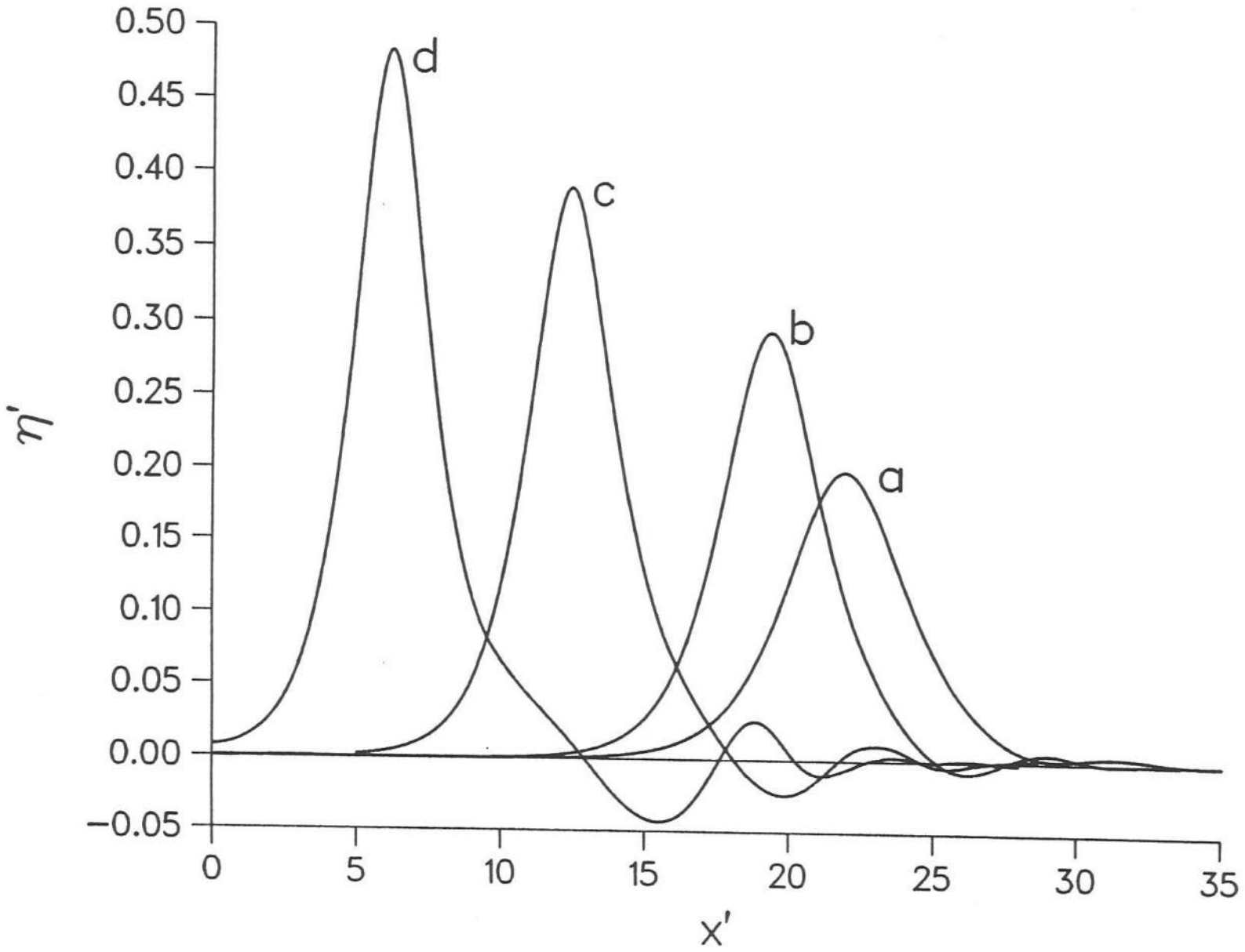

Fig. 9a: Reflection On A Vertical Wall

H/d=0.5 : I/R Waves for t'=23.525, tau2=3

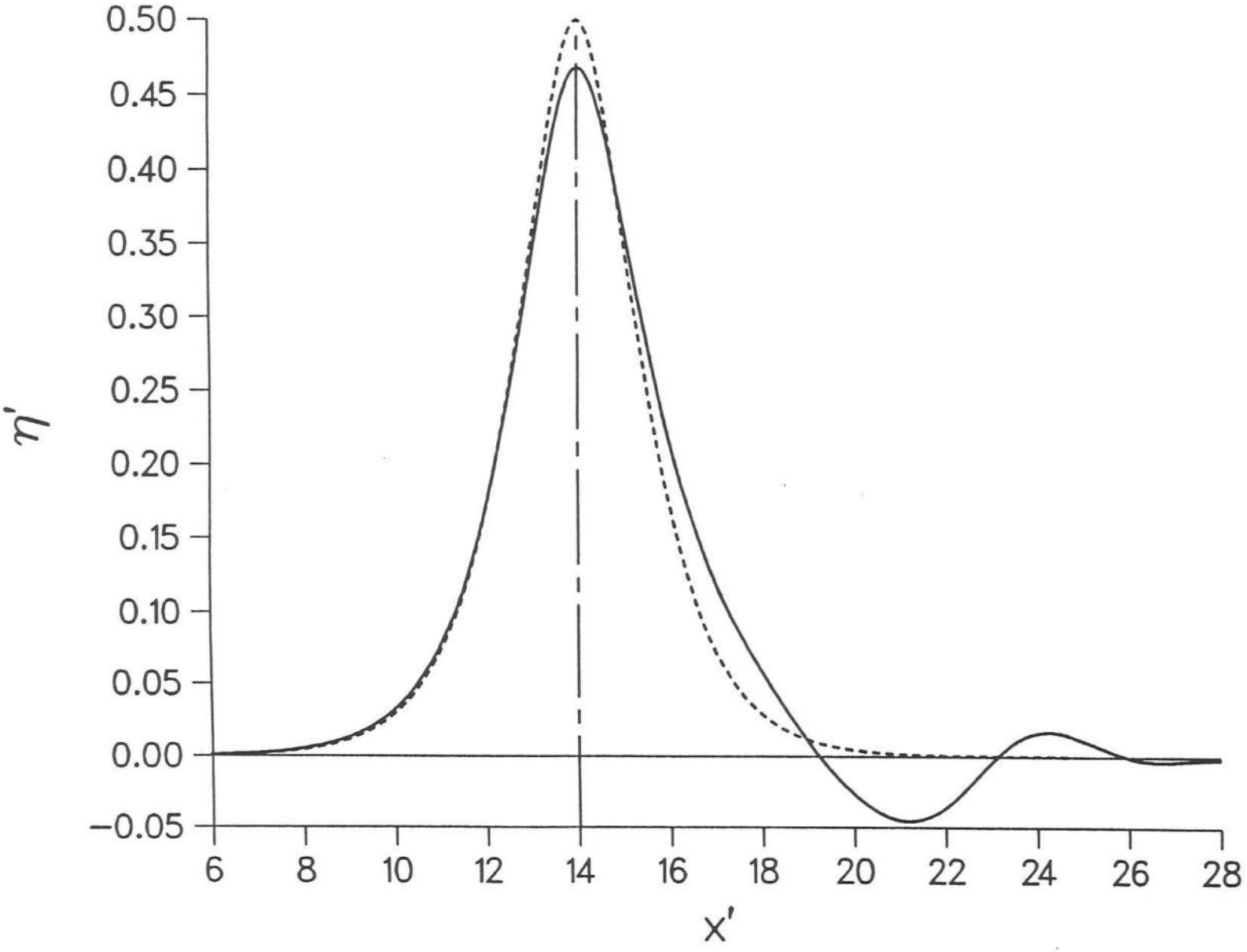

Fig. 9b: Reflection On A Vertical Wall

Amplitude Drop for H/d=0.5

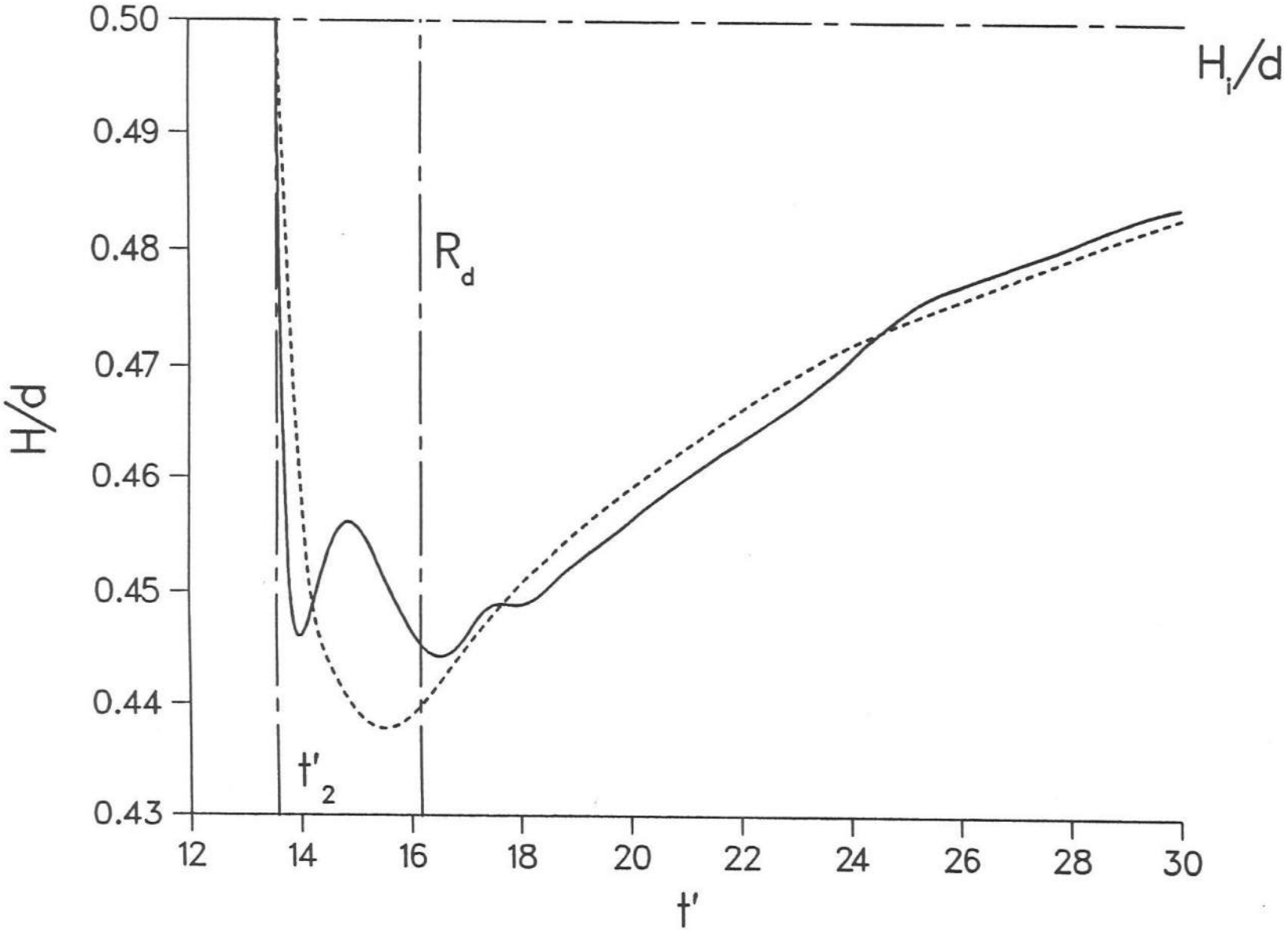

Fig. 9c: Reflection On A Vertical Wall

H/d=0.5 : Oscillatory Tail : x'_o=14.00, tau2=3

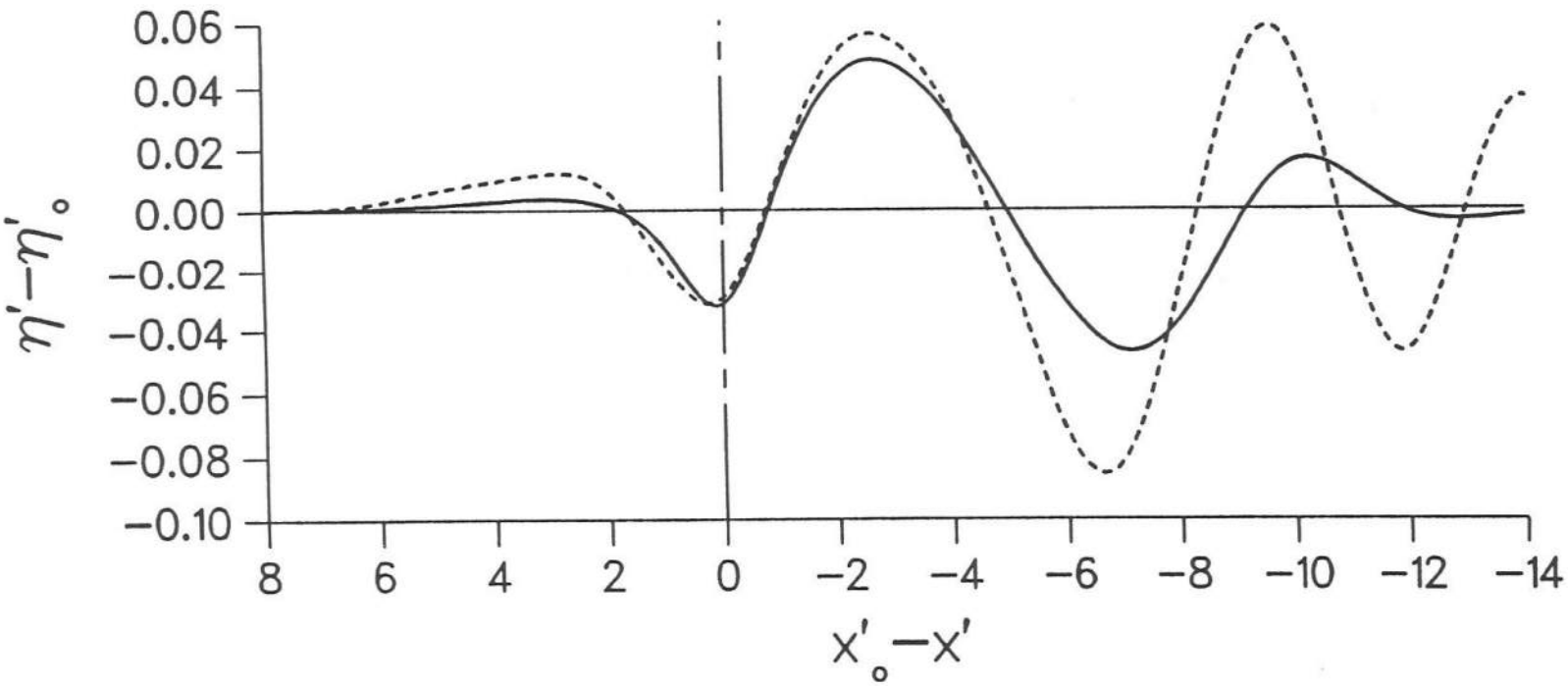

Fig. 10a: Reflection On A Vertical Wall

Phase diagram H/d=0.5, dt=0.05-0.025, dx/d=0.25

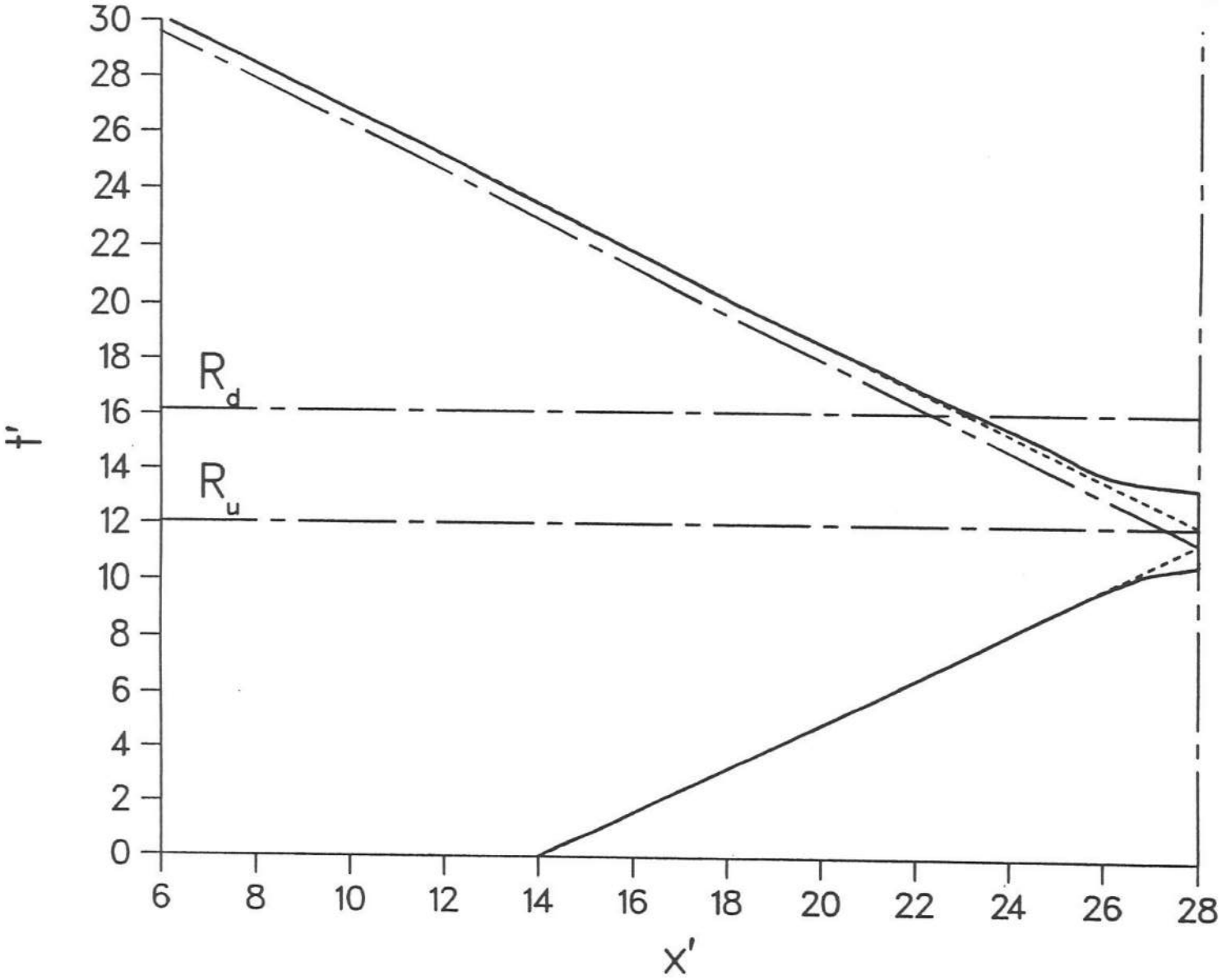

Fig. 10b: Reflection On A Vertical Wall

Phase shift H/d=0.5, dt=0.05-0.025, dx/d=0.25

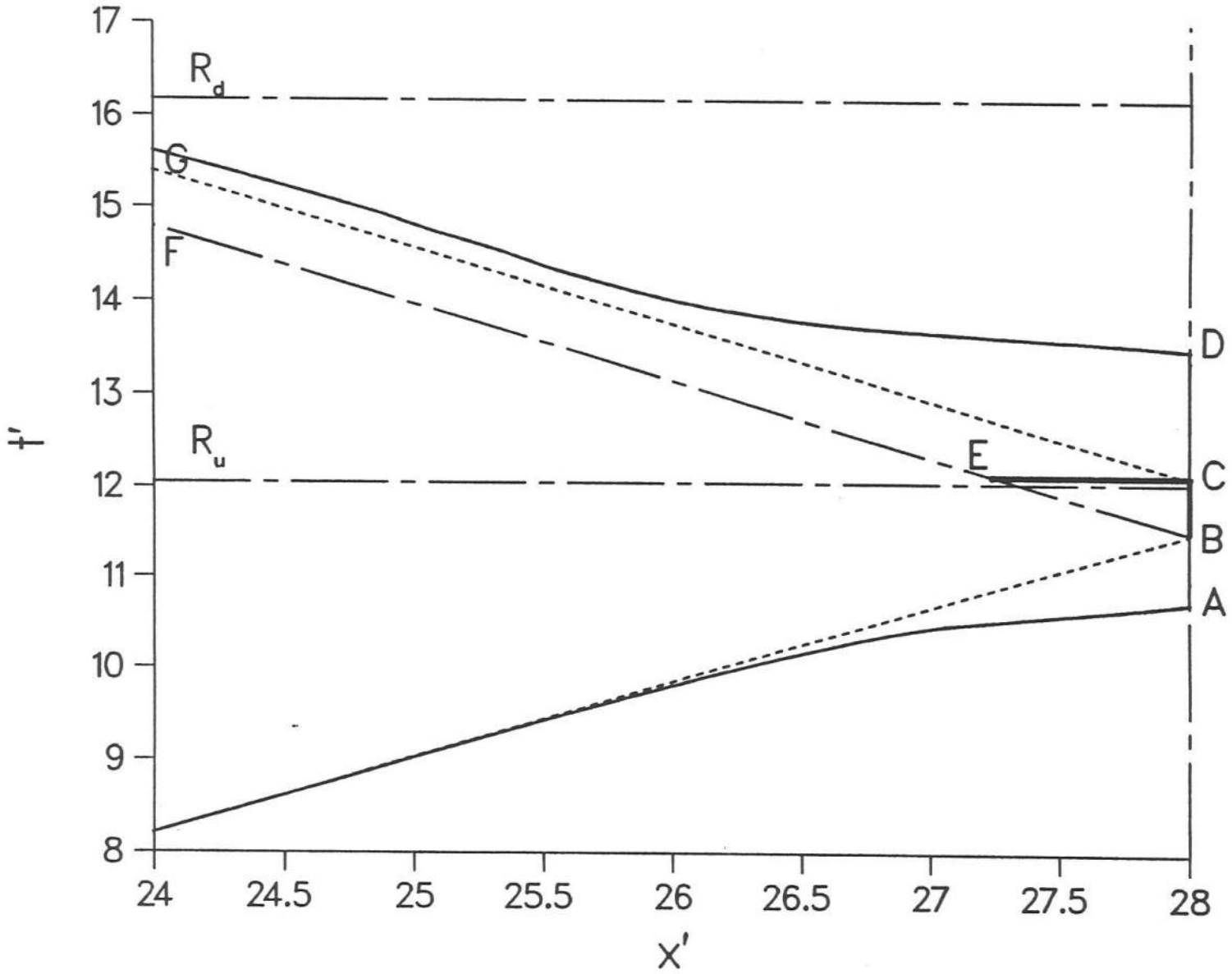

Fig. 11a: Reflection On A Vertical Wall

Energy, H/d=0.5, dt=0.05-0.025, dx/d=0.25

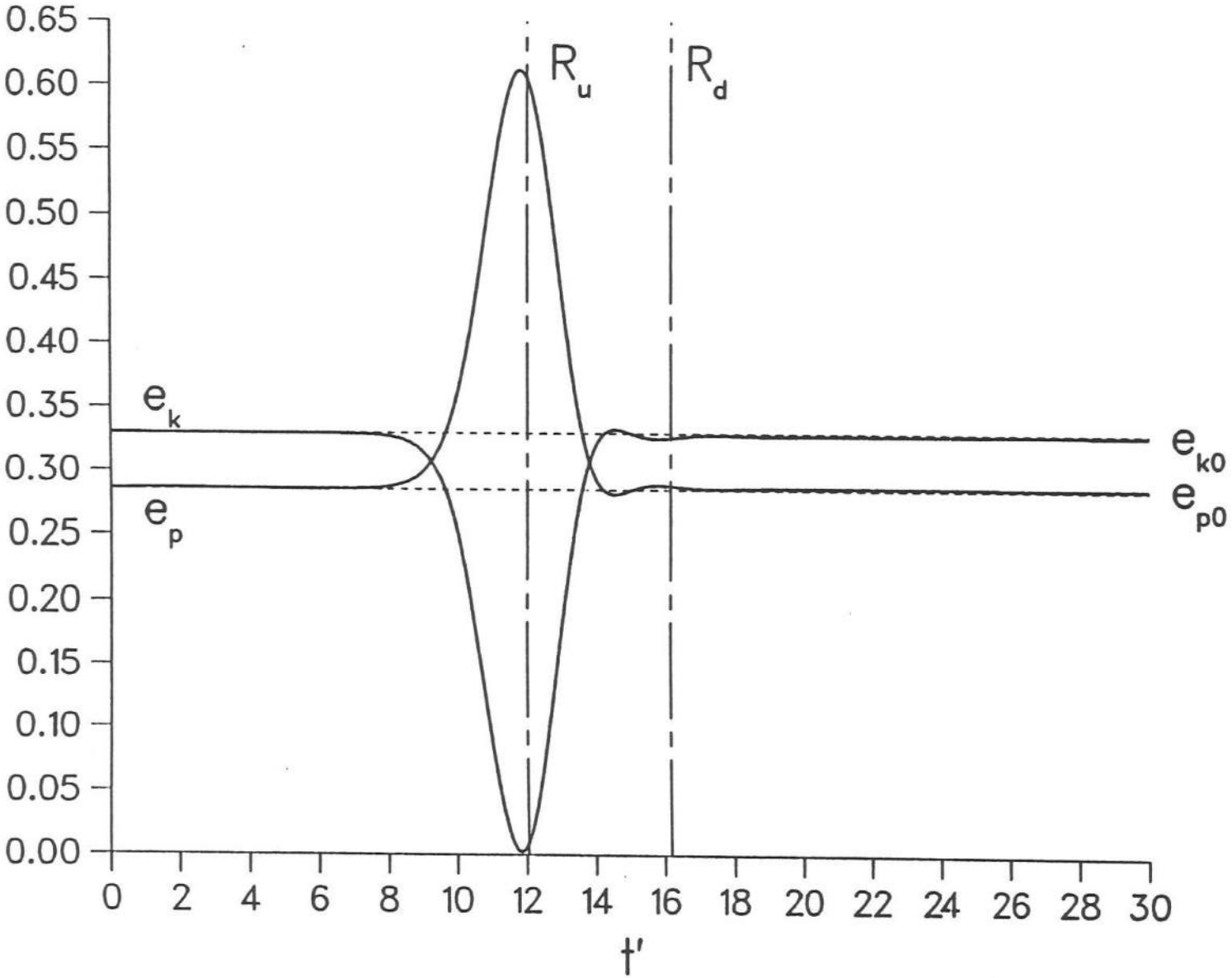

Fig. 11b: Reflection On A Vertical Wall

Energy, H/d=0.5, dt=0.05-0.025, dx/d=0.25

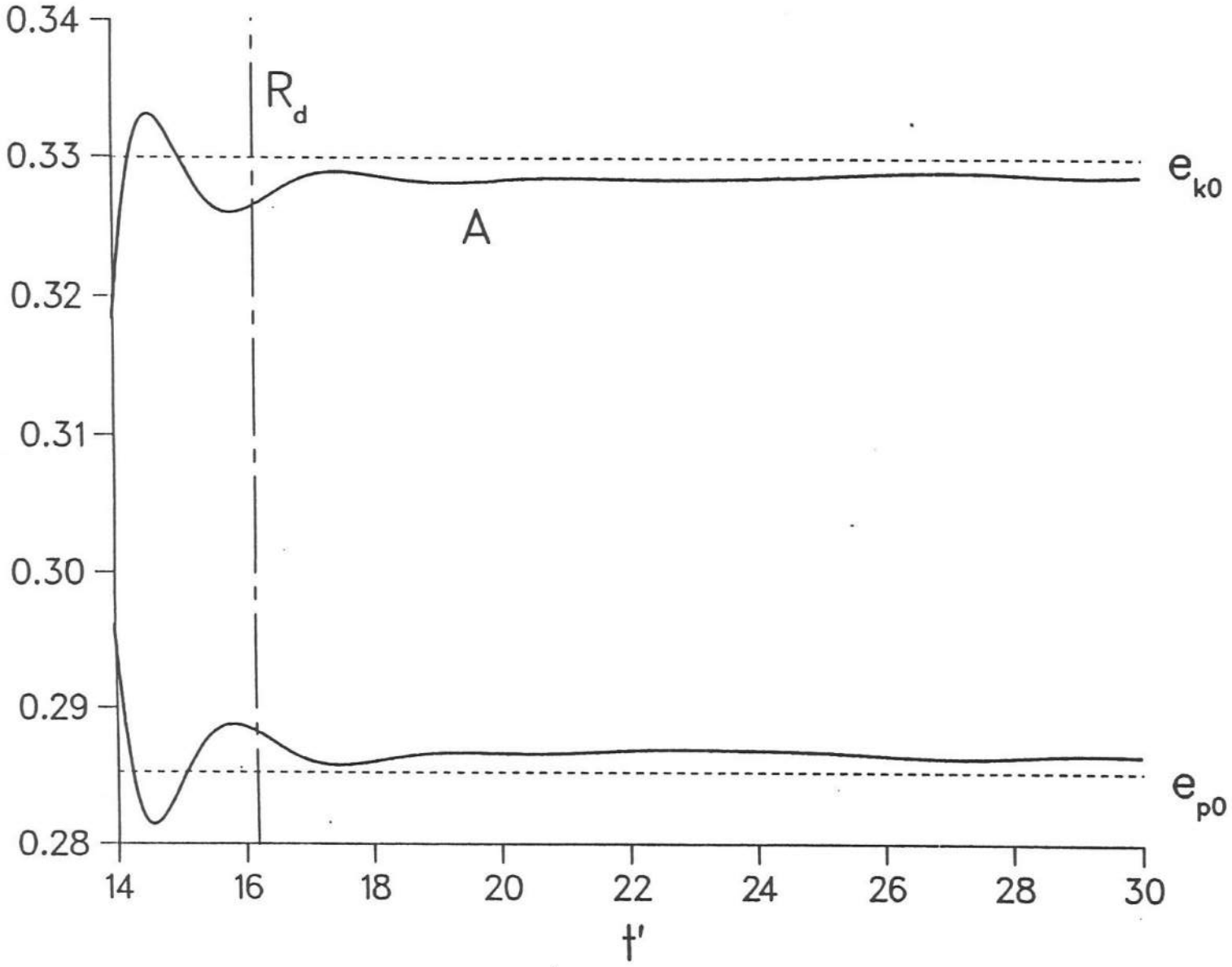

Fig. 12a: Reflection On a Vertical Wall

Maximum Horizontal Force

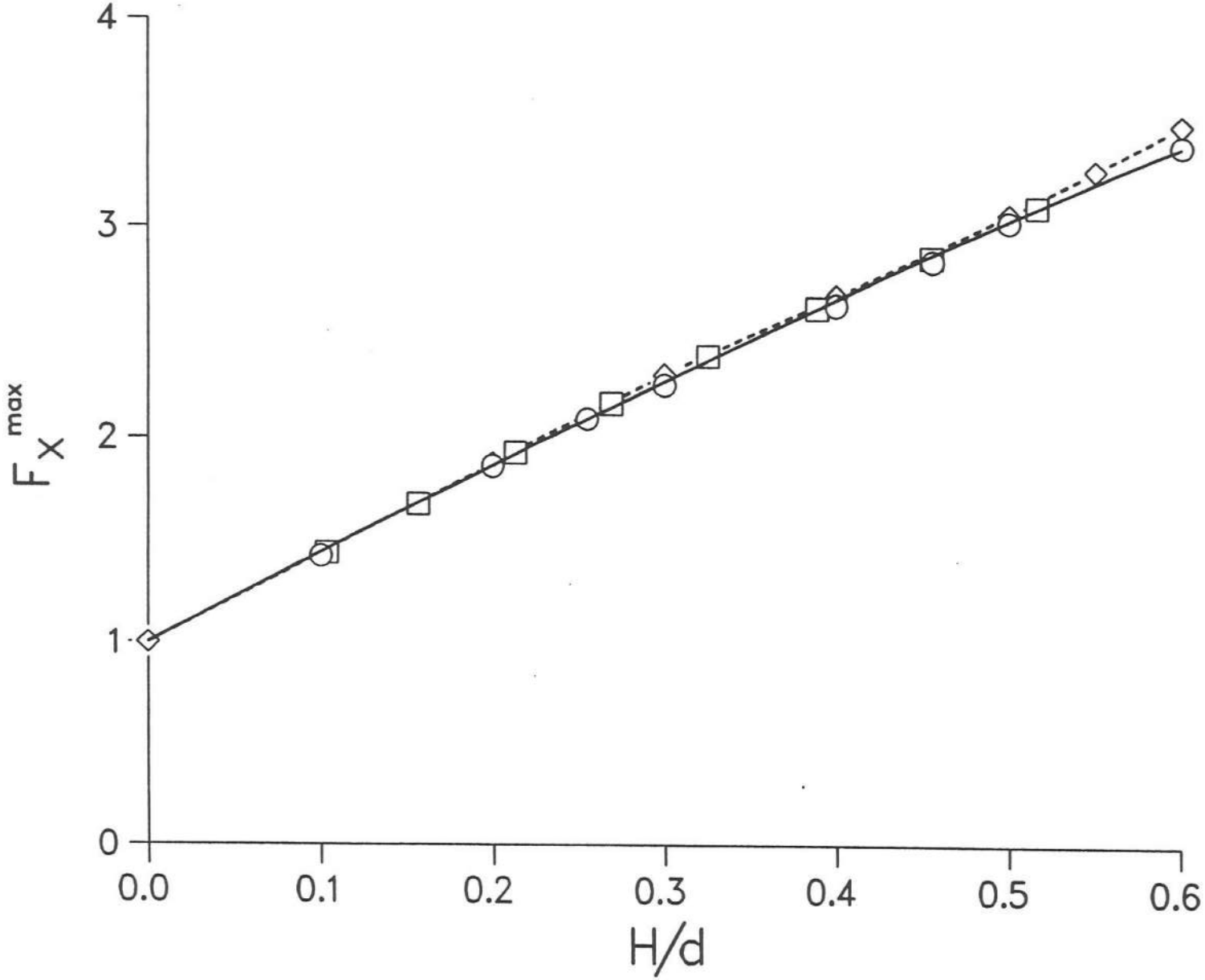

Fig. 12b: Reflection On a Vertical Wall

Maximum Moment With Respect To The Bottom Of The Wall

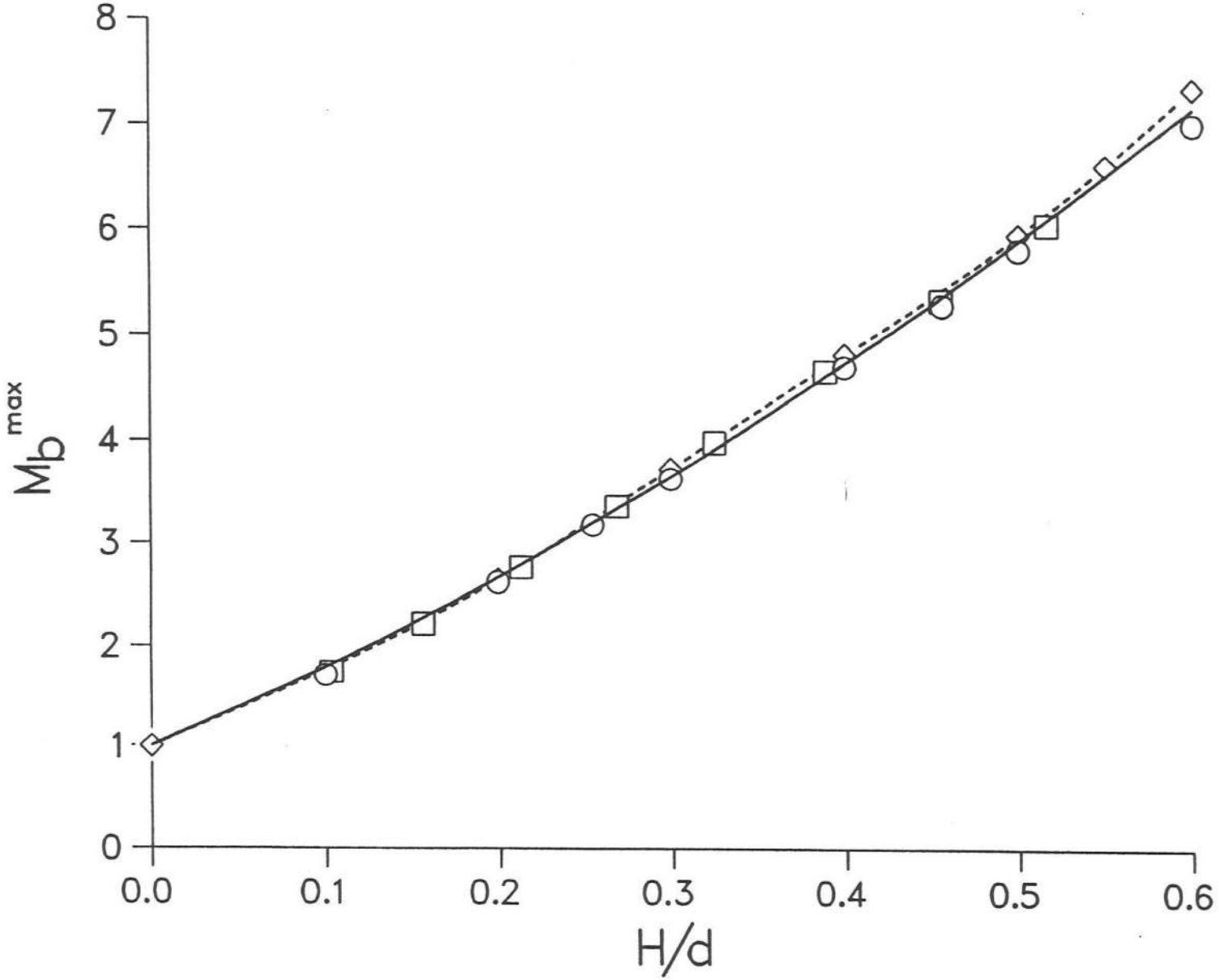

Fig. 13a: Reflection On A Vertical Wall

Horizontal Force In Time

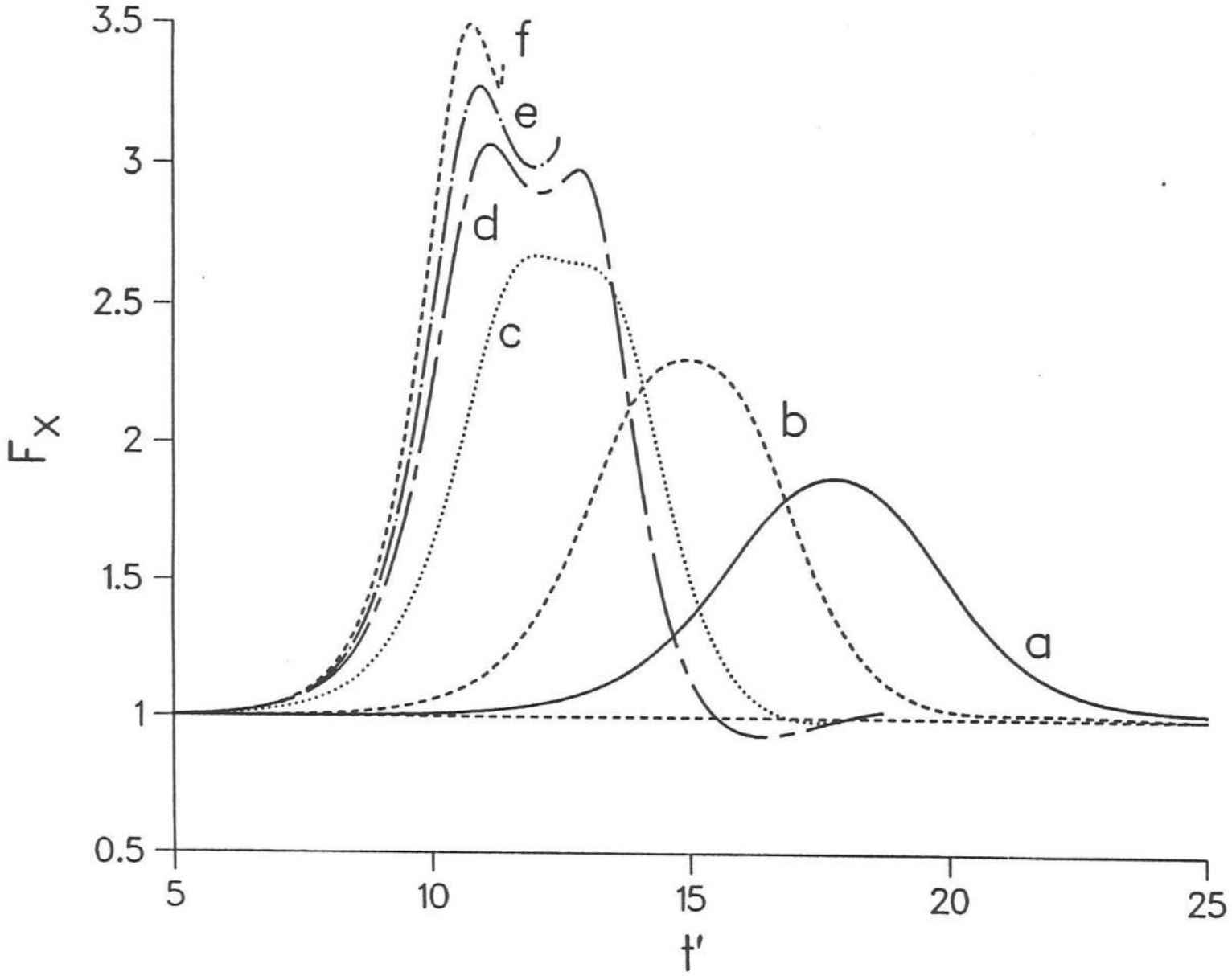

Fig. 13b: Reflection On A Vertical Wall

Mechanics, H/d=0.5, dt=0.05-0.025, dx/d=0.25

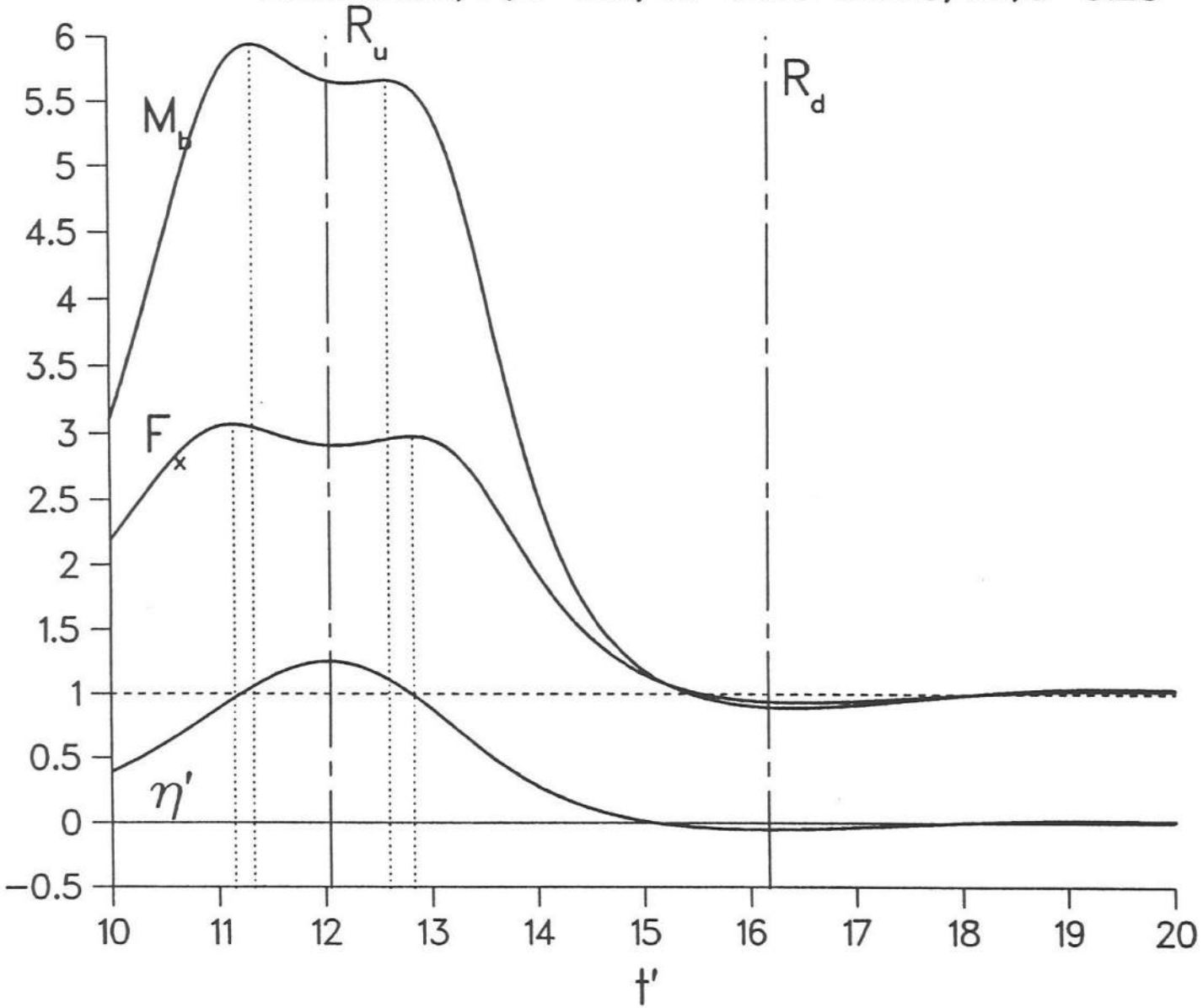

Fig. 14a: Reflection On a 45 Degree Slope

Solitary Wave, H/d = 0.269

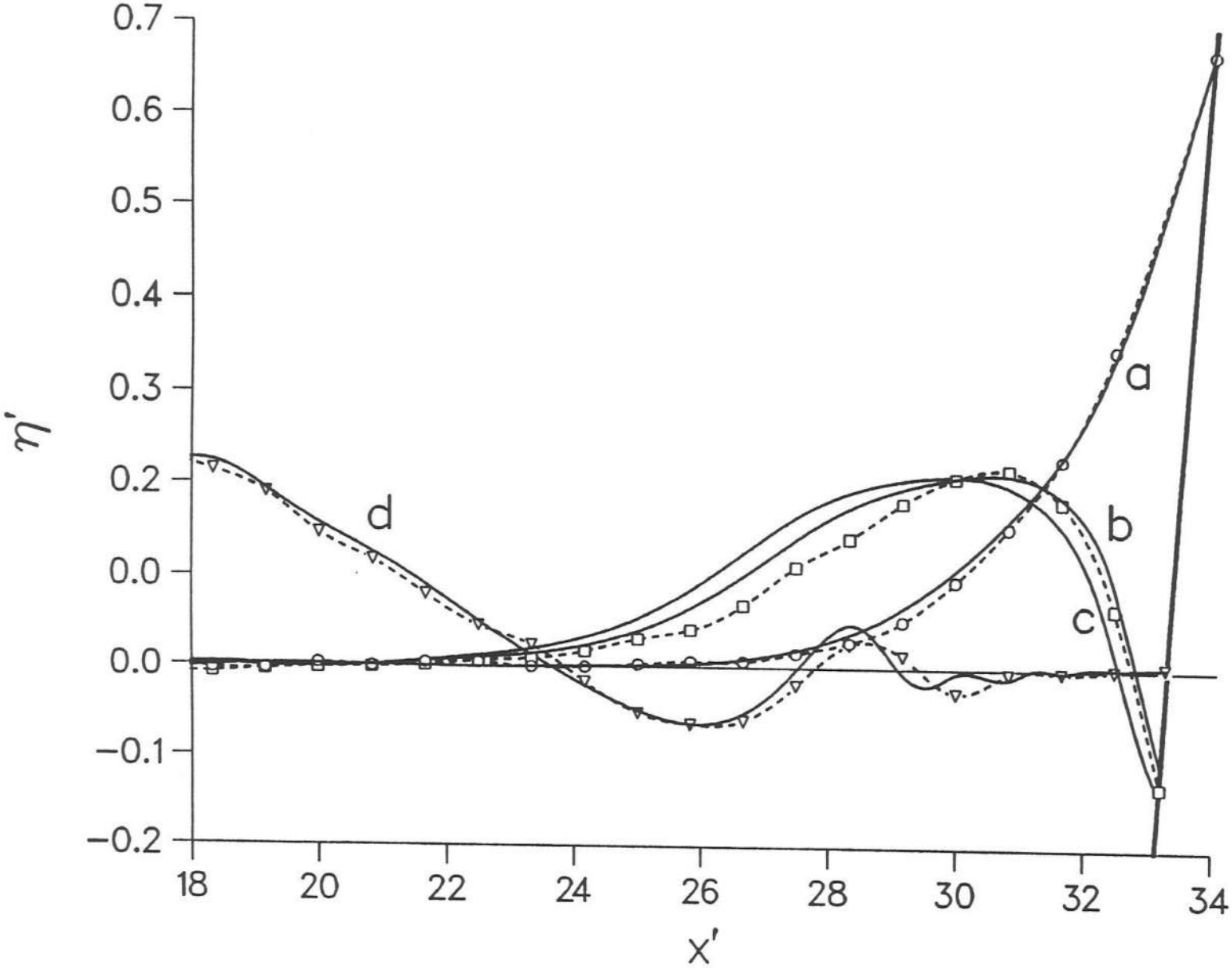

Fig. 14b: Reflection On a 45 Degree Slope

Solitary Wave, H/d = 0.457

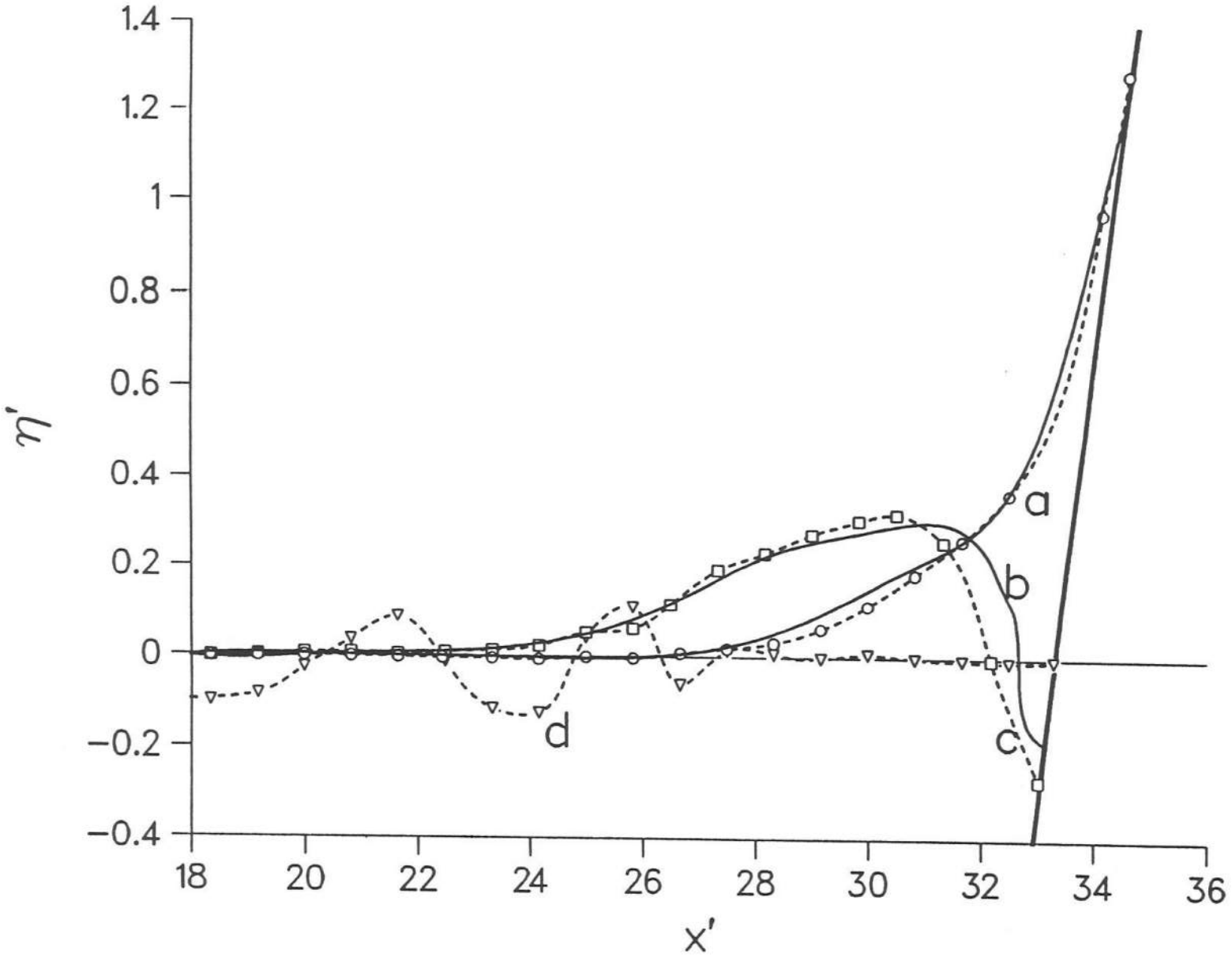

Fig. 15a: Reflection On a 70 Degree Slope

Solitary Wave, H/d = 0.259

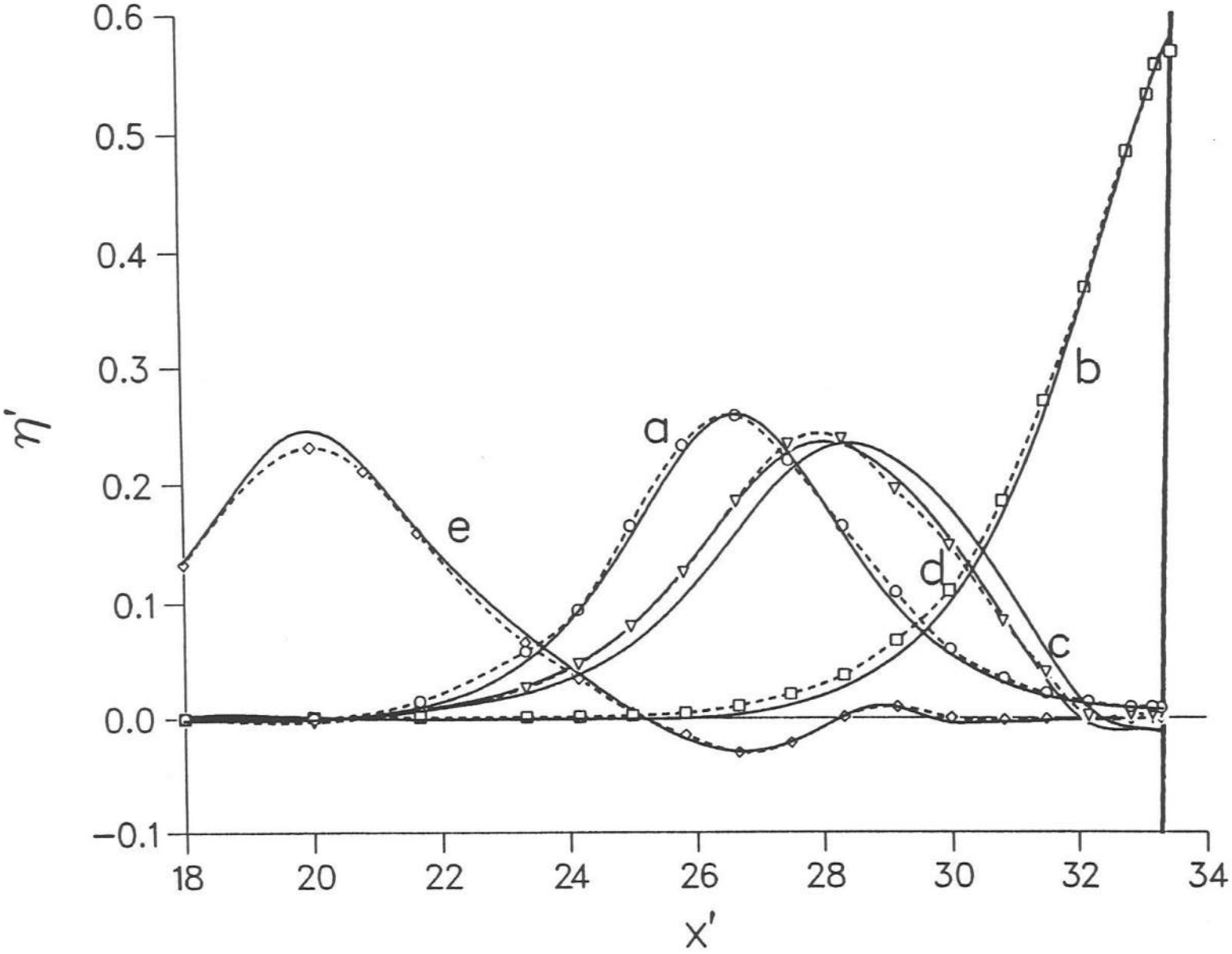

Fig. 15b: Reflection On a 70 Degree Slope

Solitary Wave, H/d = 0.437

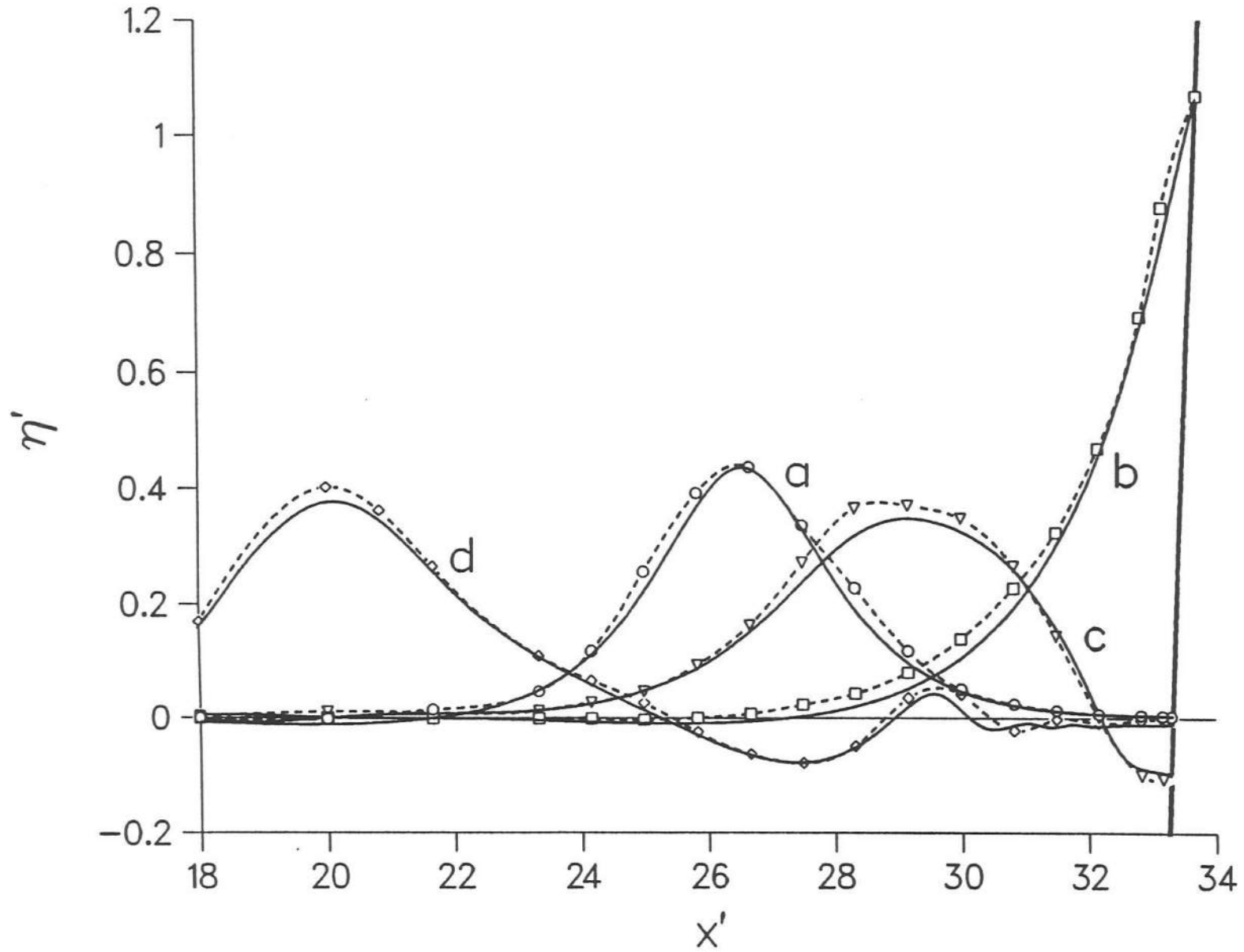

Fig. 16a: Velocity Field, t′ = 30.375

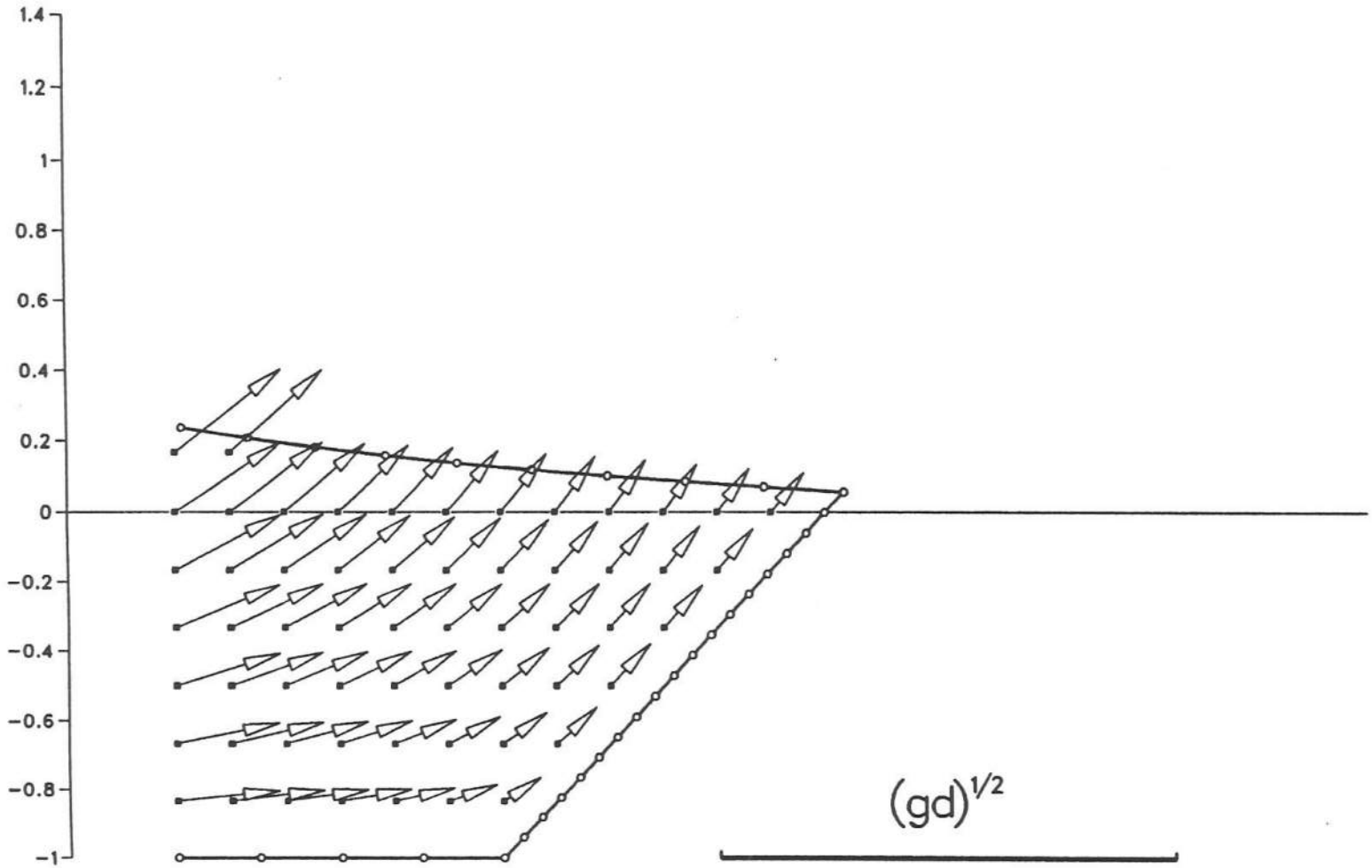

Fig. 16b: Velocity Field, $t' = 32.050$

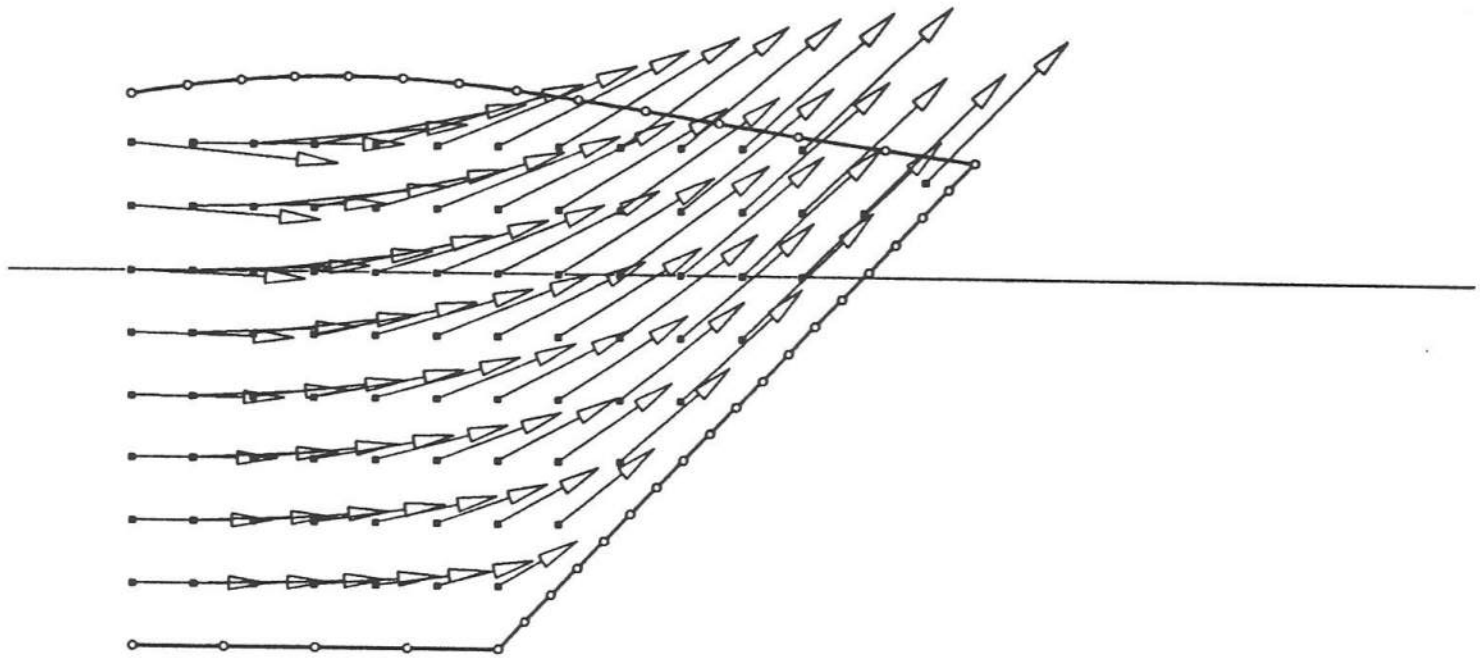

Fig. 16c: Velocity Field, $t' = 33.150$

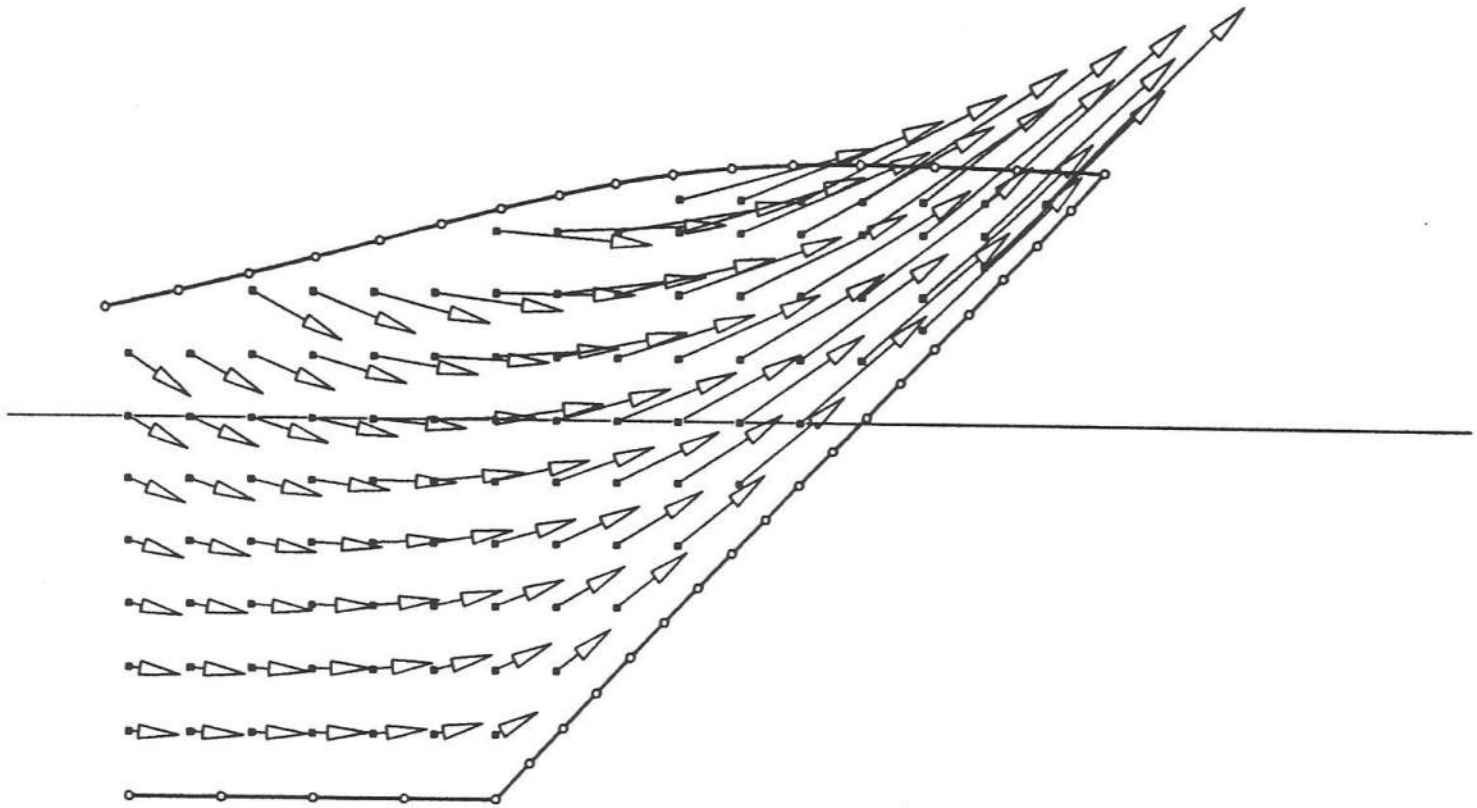

Fig.16d: Velocity Field, $t' = 33.975$

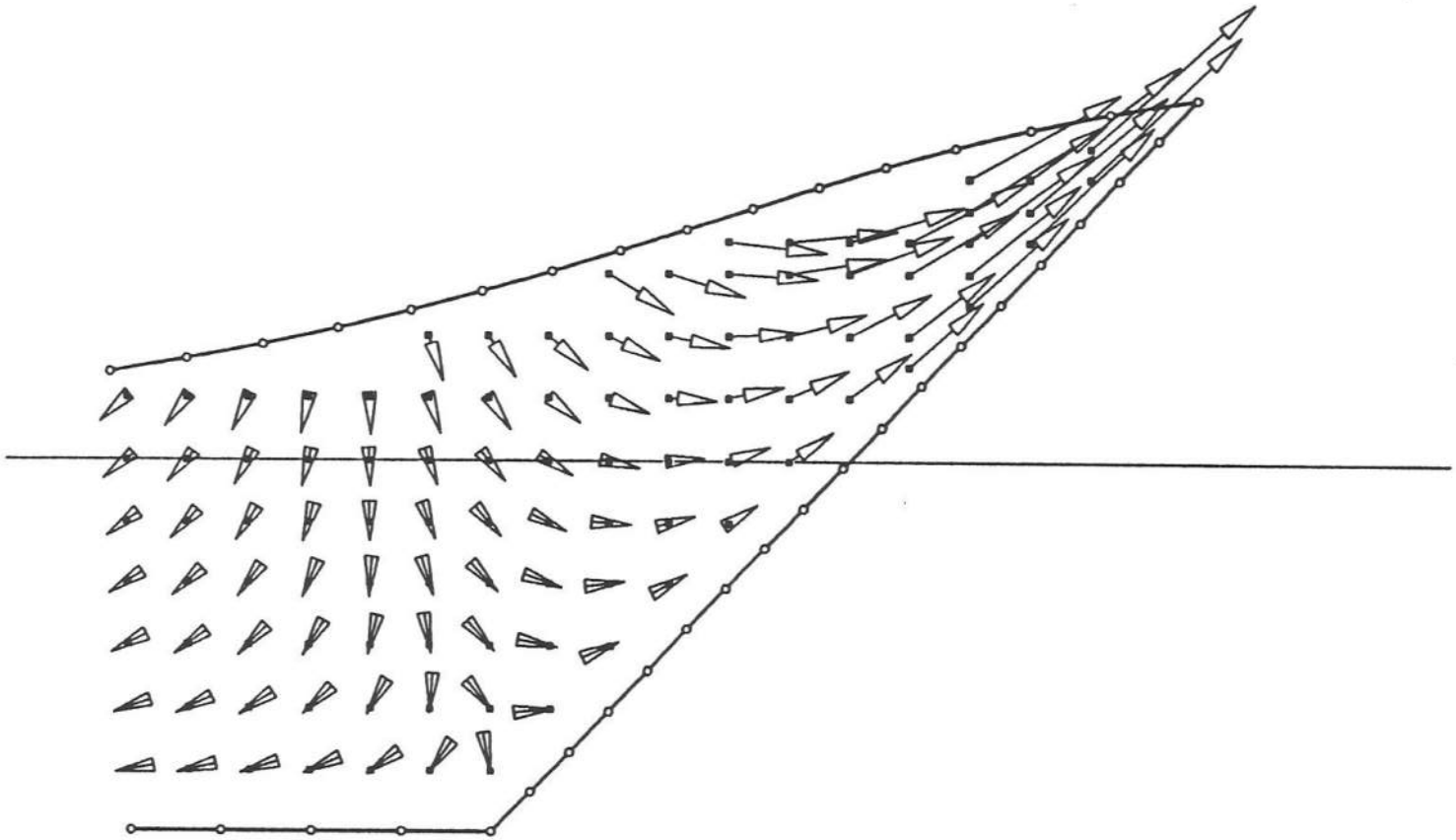

Fig. 16e: Velocity Field, $t' = 34.875$

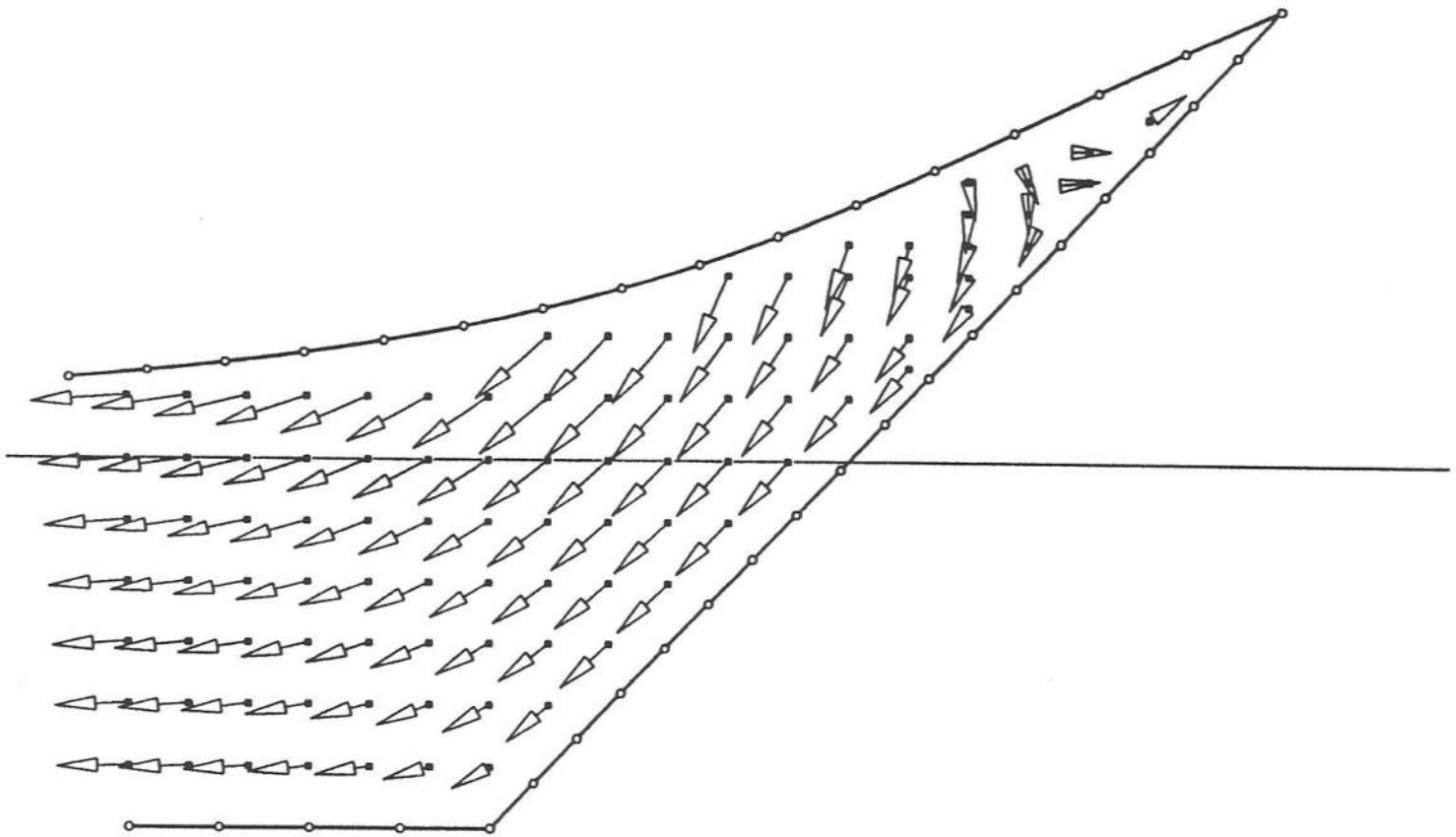

Fig. 16f: Velocity Field, $t' = 35.375$

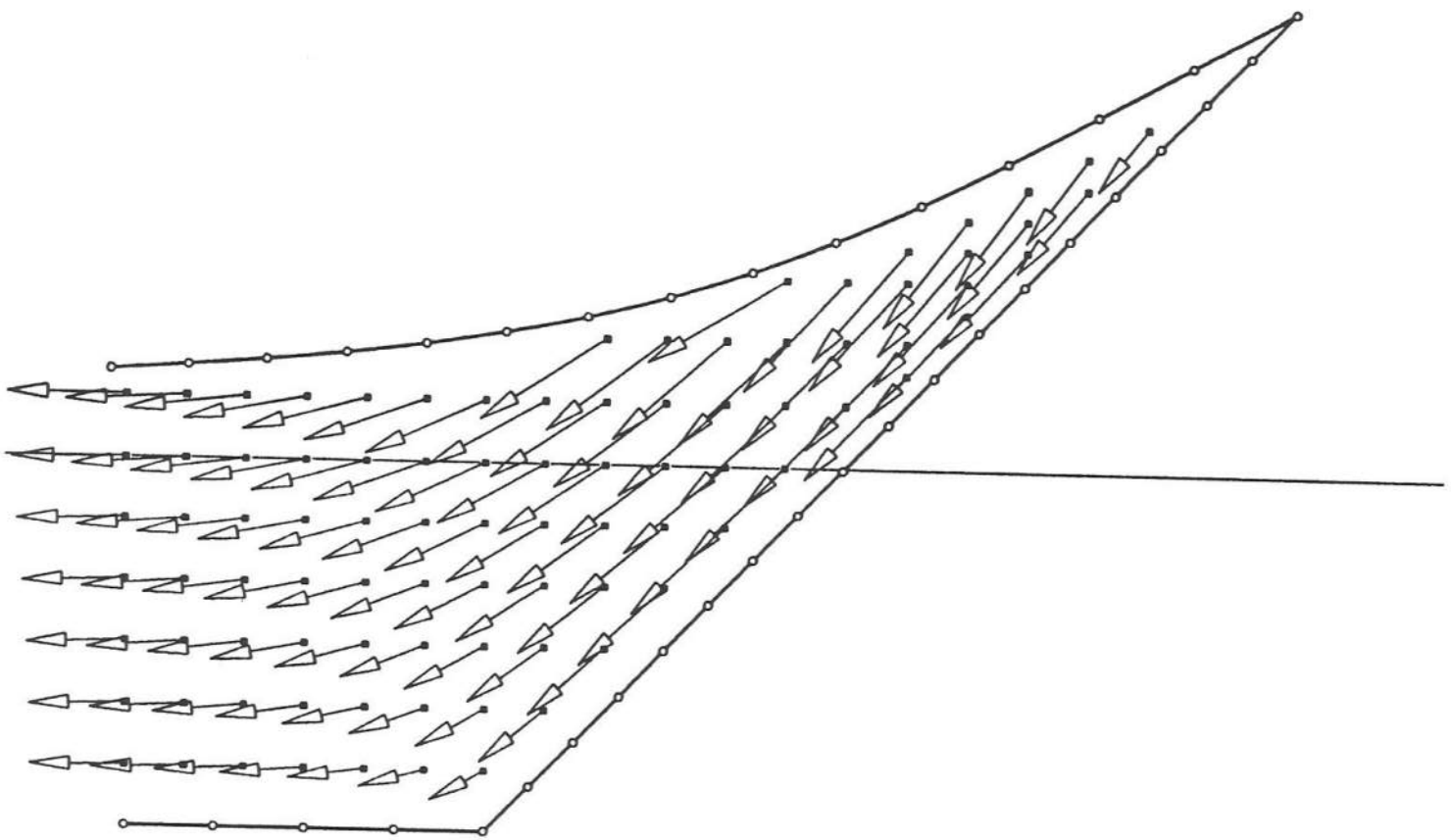

Fig. 17a: Velocity Field, $t' = 36.125$

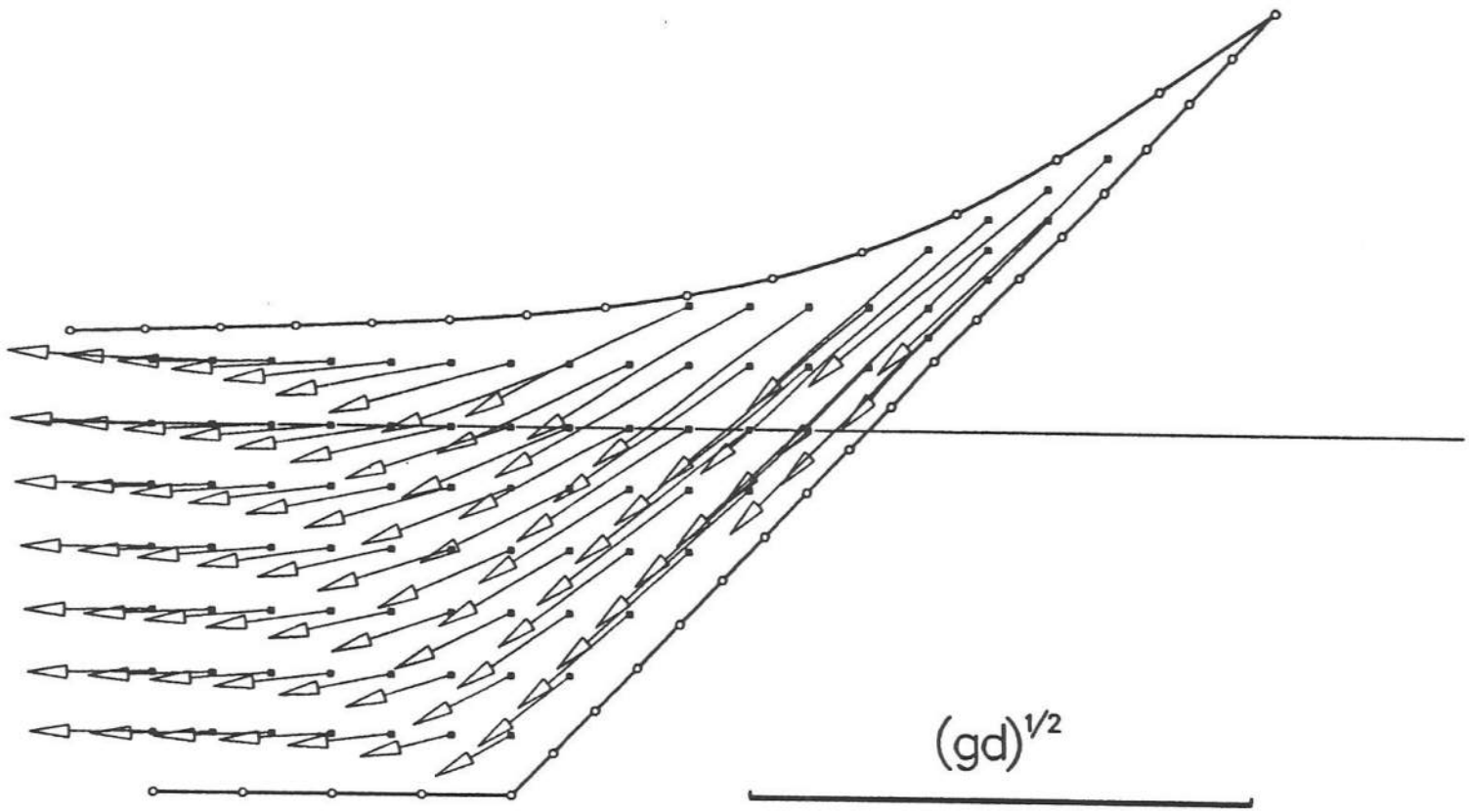

Fig. 17b: Velocity Field, $t' = 37.250$

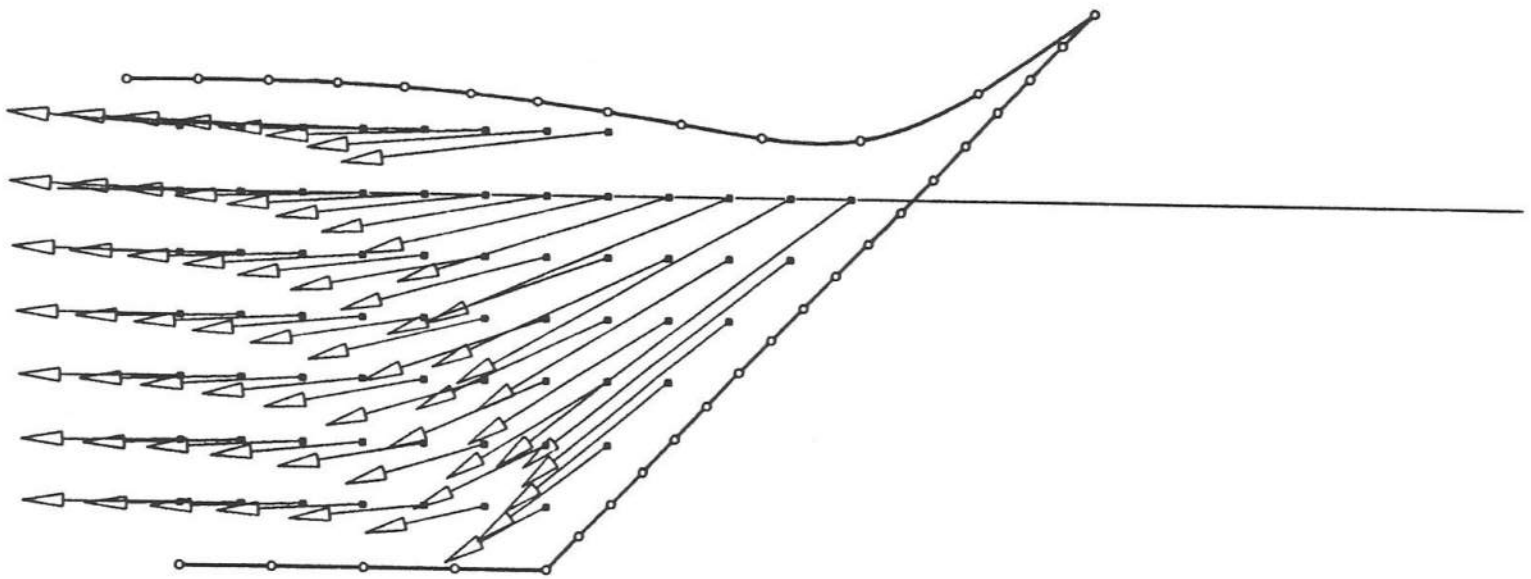

Fig. 17c: Velocity Field, $t' = 37.787$

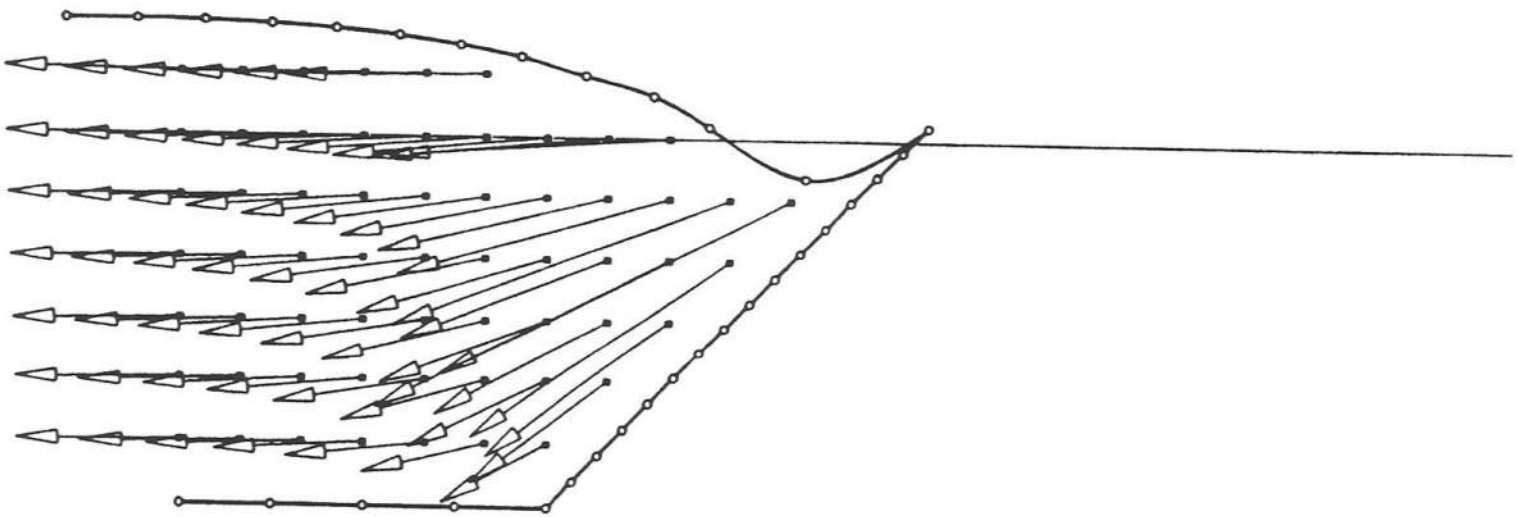

Fig. 17d: Velocity Field, $t' = 37.962$

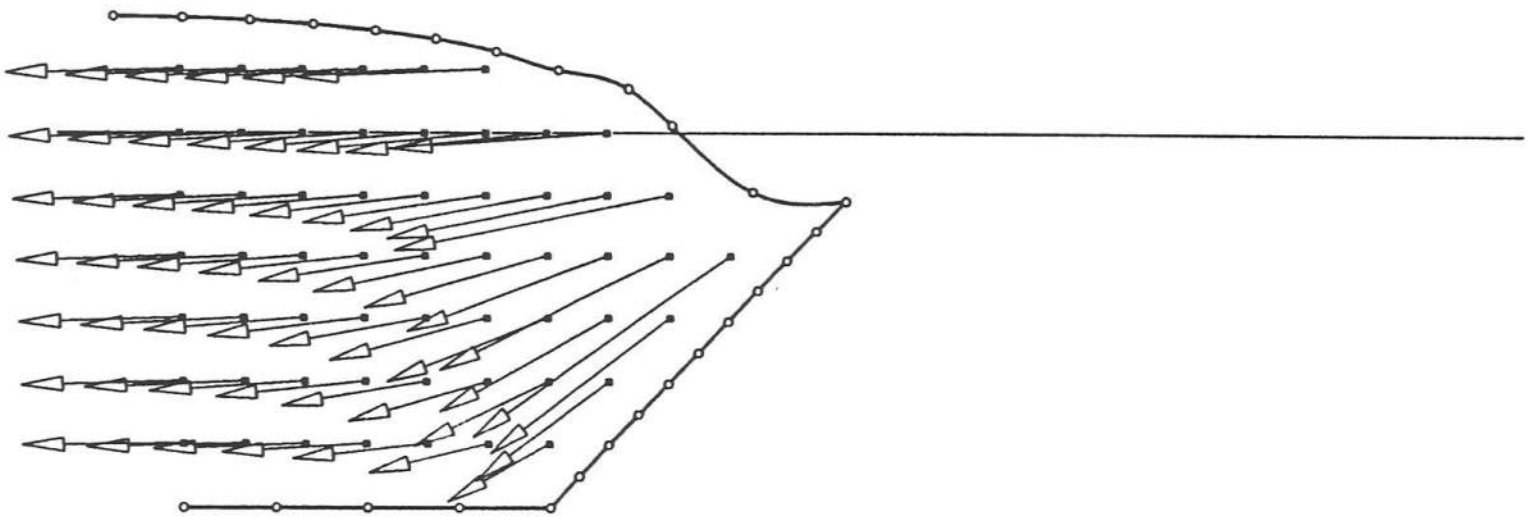

Fig. 18a: Pressure On a 45 Degree Slope

During The Runup, H/d = 0.457

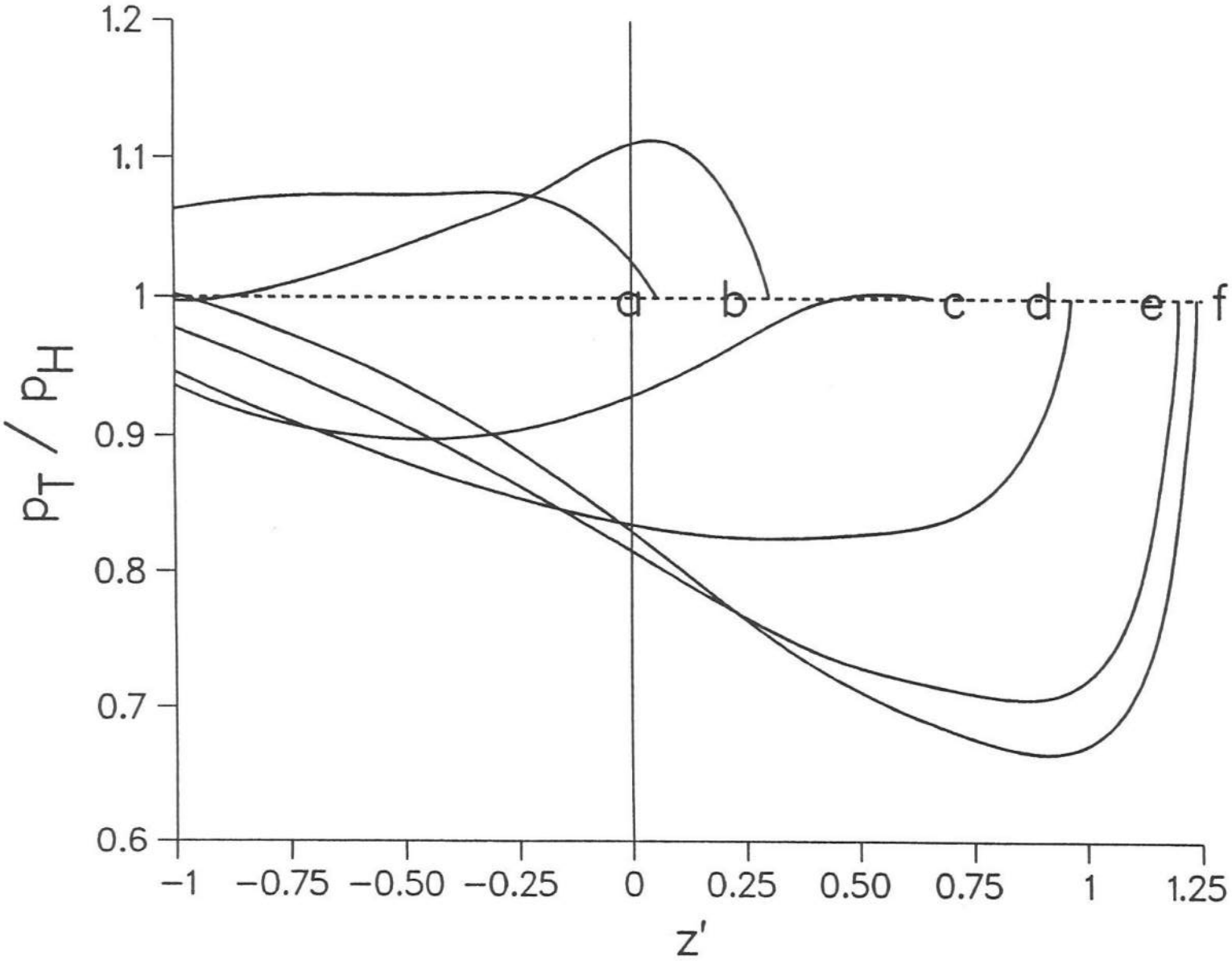

Fig. 18b: Pressure On a 45 Degree Slope

During The Rundown, H/d = 0.457